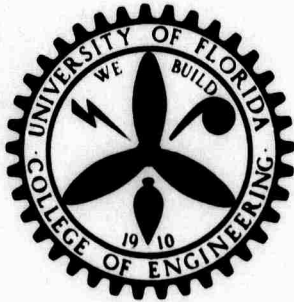


AD 711848

## A CENTER OF COMPETENCE IN SOLID STATE MATERIALS AND DEVICES

by

Fred A. Lindholm, Arthur J. Bradersen, Eugene R. Chenette,  
Robert W. Gould, Larry L. Hench, John J. Hren,  
Sheng S. Li, James K. Watson



Electrical Engineering Department  
College of Engineering  
University of Florida  
Gainesville, Florida 32601

Contract No. F 19628-68-C-0058

Project No. 8687

Scientific Report No. 5

10 March 1970

Contract Monitor  
Andrew C. Yang  
Solid State Sciences Laboratory



This document has been approved for public  
release and sale; its distribution is unlimited.

Prepared

for

**AIR FORCE CAMBRIDGE RESEARCH LABORATORIES  
OFFICE OF AEROSPACE RESEARCH  
UNITED STATES AIR FORCE  
BEDFORD, MASSACHUSETTS 01730**

This research was supported by the Advanced Research  
Projects Agency under ARPA Order No. 1060

Reproduced by the  
CLEARINGHOUSE  
for Federal Scientific & Technical  
Information Springfield Va. 22151

211

Qualified requestors may obtain additional copies from the Defense Documentation Center. All others should apply to the Clearinghouse for Federal Scientific and Technical Information.

ACQUISITION		
DDP	WHITE SECTION	<input checked="" type="checkbox"/>
DDC	DDP SECTION	<input type="checkbox"/>
UNANNOUNCED		<input type="checkbox"/>
JUSTIFICATION .....		
BY .....		
DISTRIBUTION/AVAILABILITY CODES		
DDC	AVAIL. and/or SPECIAL	
1		

# **A CENTER OF COMPETENCE IN SOLID STATE MATERIALS AND DEVICES**

by

Fred A. Lindholm, Arthur J. Brodersen, Eugene R. Chenette,  
Robert W. Gould, Larry L. Hench, John J. Hren,  
Sheng S. Li, James K. Watson

Electrical Engineering Department  
College of Engineering  
University of Florida  
Gainesville, Florida 32601

Contract No. F 19628-68-C-0058

Project No. 8687

Scientific Report No. 5

10 March 1970

Contract Monitor  
Andrew C. Yong  
Solid State Sciences Laboratory

This document has been approved for public  
release and sale; its distribution is unlimited.

Prepared

for

**AIR FORCE CAMBRIDGE RESEARCH LABORATORIES  
OFFICE OF AEROSPACE RESEARCH  
UNITED STATES AIR FORCE  
BEDFORD, MASSACHUSETTS 01730**

This research was supported by the Advanced Research  
Projects Agency under ARPA Order No. 1060

## ABSTRACT

This report describes technical findings in four main subject areas: semiconductors and semiconductor devices, insulating and semiconducting glasses, measurement techniques, and magnetic materials.

For silicon doped with gold and phosphorus, a study of the photo-magnetoelectric effect yields a basic theoretical relationship between the excess hole and excess electron concentrations and an experimental determination of the effective lifetime for temperatures between 21 and 84°K. A pragmatic approach is proposed and empirically tested concerning the dependence that the density of quantum states in a semiconductor shows on the impurity concentration. For a variety of ceramic materials, the electric-field breakdown shown is related to the various environmental and material variables. Based on available data concerning material structure, a study is made to characterize the relationship borne in semiconducting glasses between heterogeneity in structure and resultant electrical properties. Errors in x-ray spectrochemical analysis of powdered materials due to pressing variations are quantitatively examined. The several means for analysis of the defect structure of solid surfaces are discussed together with the relation that this defect structure bears to the surface electronic and chemical properties. Small-angle x-ray data on the low-temperature aging of aluminum-zinc alloys is shown to provide a method for determining the particle size distribution as a function of aging time. A new approach is proposed and evaluated for characterizing the trapped-flux interaction between magnetic films and nearby electrical conductors.

## SUMMARY

This report for the fifth semiannual period of contract support describes technical findings in four main subject areas: semiconductors and semiconductor devices, insulating and semiconducting glasses, measurement techniques, and magnetic materials.

### SEMICONDUCTORS AND SEMICONDUCTOR DEVICES:

For silicon doped with gold and phosphorus the photomagnetoelectric (PME) effect was studied theoretically and observed experimentally for temperatures between 21 and 84°K. A generalized diffusion equation is formulated and solved with the impurity centers included in the charge balance equation and for arbitrary intensity and steady illumination. When the density of gold greatly exceeds the density of the free carriers, the charged impurities maintain charge neutrality; this yields a range of injection where the excess hole concentration can be expressed as the sum of two terms: the first proportional to the excess electron concentration and the second to the square of that concentration. If the quadratic term dominates, the PME current is proportional to the  $4/3$  power of the photoconductance. Measurements show this power-law dependence, from which one can deduce that the effective lifetime ranges between 36 nsec to 63  $\mu$ sec.

The density of quantum states in a semiconductor depends on the impurity concentration; a study is reported concerning a pragmatic approach to the problem of describing this dependence. The approach combines heretofore separate theories concerning the various contributors to this dependence, utilizing an approximation that enables application of the superposed theories over the range of impurity concentration of technological interest. To demonstrate the practical utility of the approach, the prediction yielded

by its application to p-type gallium arsenide as compared to an experimentally determined density of states. The agreement is satisfactory.

#### INSULATING AND SEMICONDUCTING GLASSES:

The electric field a ceramic material can withstand may determine its applicability in various uses in the electronic technology: as an insulator, as a protective surface in various devices, as an isolator in integrated circuits, and as a material for encapsulation. The several theories of breakdown mechanisms in ceramics are reviewed and the influence of environmental and materials variables on the breakdown strength is discussed. The discussion includes consideration of the following variables: thickness, temperature, ambient atmosphere, electrode shape and composition, surface finish, field frequency and waveform, porosity, crystalline anisotropy, amorphous structure, and composition. The relative importance of these factors receives attention for a variety of ceramic materials.

Heterogeneities present in semiconducting glasses play a key role in determining the electrical properties of the glass. Based on available data concerning material structure, yielded by small-angle scattering x-ray studies, and concerning the dc and ac conductivity of  $V_2O_5$ - $KPO_4$  semiconducting glass, a theoretical study is made to characterize the relationship borne between structure and electrical properties. Various alternative models of the conduction mechanisms are proposed and evaluated.

Errors in x-ray spectrochemical analysis of powdered materials due to sample pressing variations are quantitatively examined. It is shown that the x-ray intensity of a pressed sample is a function of the sample density.  $MgO$ ,  $TiO_2$ ,  $Cr_2O_3$  and  $ThO_2$  samples all exhibited three major regions of x-ray response in the intensity vs density studies. Analytical errors of as much as 50% can result if measurements are made without regard to pressed density

variation. The behavior is explained in terms of density gradients produced during pression. Appreciable thickness dependence of x-ray results in  $\text{MgCO}_3$  samples is also discussed.

#### MEASUREMENT TECHNIQUES:

The development of ultra-high vacuum capabilities and sophisticated observational methods has enabled the analysis of the defect structure of solid surfaces and the relation of this defect structure to many physical properties. In this study various means for characterizing the defect structure, such as optical, x-ray topographs, and transmission electron-microscopy are described with major emphasis being placed on the observation and interpretation of surface defects by the field-ion microscopic technique. The influence of these defects on the surface electronic and chemical properties receives attention.

Small-angle x-ray data on the low-temperature aging of three aluminum-zinc alloys affords a method for determining the particle size distribution as a function of aging time. The study yields a series of particle size distribution curves and particle diameter growth paths, and the evolution of the particle size distribution can be followed. The observed growth can be described as a typical particle coarsening process with competitive growth. The zonal state immediately after quench is characterized by a more monodisperse zone size distribution than at later aging times.

#### MAGNETIC MATERIALS:

The trapped-flux interaction between magnetic films and nearby electrical conductors is a well-known phenomenon experimentally and has constituted the basic mechanism of NDRO memories. Previous theoretical analyses of this process, however, have proved so formidable computationally and conceptually as to limit their usefulness. A new approach is suggested that,

despite its simplicity, leads to results that agree well with those that are predicted by the more complicated methods. The approach consists basically in appealing to the analogy of an RC transmission line. Subsequent use of this analog permits geometrical factors to be represented as electric circuit components yielding thereby conceptual and computational advantages. Taking into account the geometry of the film insulators and conductors, the approach provides a basis for estimating the magnitude and time duration of switching transients. The model developed explains the experimental observation that eddy-current torques play an insignificant role in film flux reversal for devices with large stripline separation.



## TABLE OF CONTENTS

	<u>Page</u>
I. <u>Introduction</u>	1
II. <u>Semiconductors and Semiconductor Devices</u> (A. J. Brodersen, E. R. Chenette, R. W. Gould, L. L. Hench, J. J. Hren, S. S. Li, F. A. Lindholm, C. T. Sah, A. van der Zeil)	2
A. LOW TEMPERATURE PHOTOMAGNETOELECTRIC PROPERTIES OF GOLD- DOPED n-TYPE SILICON (J. Agraz-G. and S. S. Li)	2
Introduction	2
Theory	2
Charge Neutrality	4
Diffusion Equation	5
The PME Effect and Photoconductance	6
Experimental Results and Discussion	8
References	17
B. IMPURITY CONCENTRATION DEPENDENCE OF THE DENSITY OF STATES IN SEMICONDUCTORS (D. Dale Kleppinger and F. A. Lindholm)	19
Introduction	19
Conventional Theory	21
Impurity States	22
Conduction Band States	23
The Approach	26
The Density of States in p-type Gallium Arsenide	27
a. Qualitative Discussion	27
b. Quantitative Discussion	30
Discussion	32
Appendix	35
References	38
III. <u>Insulating and Semiconducting Glasses</u> (E. R. Chenette, R. W. Gould, L. L. Hench, J. J. Hren)	39
A. DIELECTRIC BREAKDOWN OF CERAMICS (G. C. Walther and L. L. Hench)	39
Introduction	39
Definitions	43
Breakdown Mechanisms	45
Intrinsic Breakdown	45
Thermal Breakdown	52
Avalanche Breakdown	55
Experimental Variables	60
Conclusions	68
References	69

III. Cont.	<u>Page</u>
B. HETEROGENEOUS SEMICONDUCTING GLASSES (H. F. Schaake)	72
Introduction	72
Heterogeneous Models	75
Mechanisms and Conductivity in Homogeneous Glasses	80
Heterogeneous Mechanisms	84
1. Barrier Tunneling	86
2. Thermal Activation Over the Barrier	89
Application to Heterogeneous Glasses	89
Appendix	102
References	104
C. POWDER SAMPLE PREPARATION ERRORS IN X-RAY SPECTROCHEMICAL ANALYSIS (D. E. Clark and L. L. Hench)	106
Introduction	106
Experimental Procedure	108
Experimental Results	110
Discussion of Results	116
Conclusions	121
References	122
IV. <u>Measurement Techniques</u> (R. W. Gould, L. L. Hench, and J. J. Hren)	123
A. STRUCTURE OF SURFACE DEFECTS (D. L. Stoltz and J. J. Hren)	123
Introduction	123
Methods of Observation	126
Interpretation of Surface Defects by Field-Ion Microscopy	136
Summary and Conclusions	156
References	158
B. THE EVOLUTION OF PARTICLE SIZE DISTRIBUTION FROM DATA ON THE LOW TEMPERATURE AGING OF ALUMINUM-ZINC ALLOYS (R. W. Gould)	161
Introduction	161
Analysis of Data	162
Determination of $N_v(R)$	168
Discussion	174
Summary	176
References	177

	<u>Page</u>
V. <u>Magnetic Materials</u> (J. K. Watson)	178
A. ANALOG APPROXIMATIONS OF TRANSIENT FLUX DIFFUSION (J. K. Watson and C. T. Leis)	178
Introduction	178
System Model	179
Electric Analog	185
System Solutions	189
Comparison of Results	190
Conclusion	192
Appendix	195
References	196
VI. <u>Discussion</u>	197

## I. Introduction

The original general objective of this research program was to establish at the University of Florida a "Center of Competence in Solid-State Materials and Devices." From the efforts expended in developing this center of competence have evolved technical findings: technical findings concerning such materials as glass ceramics, semiconducting glasses, magnetic films, degenerate materials, and degenerate semiconductors, concerning devices made from these materials; concerning measurement techniques; and concerning methods of fabrication. The first of the findings in these various areas are described in four previous scientific reports.<sup>1-4</sup> To Scientific Report No. 1 the reader is referred for a more detailed statement of the research objectives than given here and for a discussion of the means to be used in achieving these objectives. The present report sets forth major findings of the fifth semiannual period of contract support. In the presentation to follow, Section II describes the results of research concerning semiconductors and semiconductor devices, Section III reports findings concerned with insulating and semiconducting glasses, Section IV describes advances made in measurement techniques, and Section V deals with research concerning magnetic materials.

## REFERENCES

1. F. A. Lindholm et al, Scientific Report No. 1, Contract #F 19628-68-C-0058, College of Engineering, University of Florida, 10 April 1968.
2. F. A. Lindholm et al, Scientific Report No. 2, Contract #F 19628-68-C-0058, College of Engineering, University of Florida, 10 October 1968.
3. F. A. Lindholm et al, Scientific Report No. 3, Contract #F 19628-68-C-0058, College of Engineering, University of Florida, 10 April 1969.
4. F. A. Lindholm et al, Scientific Report No. 4, Contract #F 19628-68-C-0058, College of Engineering, University of Florida, 10 October 1969.

**II. Semiconductors and Semiconductor Devices** (A. J. Brodersen, E. R. Chenette, R. W. Gould, L. L. Hench, J. J. Hren, S. S. Li, F. A. Lindholm, C. T. Sah, A. van der Ziel)

**A. LOW TEMPERATURE PHOTOMAGNETOELECTRIC PROPERTIES OF GOLD-DOPED n-TYPE SILICON** (J. Agraz-G. and S. S. Li)

**1. Introduction**

The purpose of this study was to investigate the effects of heavy gold doping upon the transport of excess carriers in n-type silicon by means of the photomagnetolectric (PME) effect. This effect was observed between 21° and 84°K in gold- and phosphorus-doped silicon and the small Hall angle theory<sup>1</sup> has been extended to account for the effects of the impurities.

For constant recombination lifetime, no trapping and constant ambipolar diffusivity, the PME short circuit current is proportional to the photoconductivity<sup>1</sup>. The PME effect has been studied in silicon under these conditions for small<sup>2</sup> and large signal<sup>3,4</sup>. The trapping by the gold centers has significant effects on the diffusion of excess carriers when the equilibrium carrier density is smaller than the gold density. This case occurs in silicon overcompensated by gold at room temperature and in undercompensated silicon at very low temperatures. Our experiments at low temperature show a PME short circuit current proportional to the 4/3 power of the photoconductance. This power law is also obtained from our theoretical analysis.

**2. Theory**

The experimental situation is schematically shown in Fig. 1. The theory for the PME effect<sup>1</sup> involves the solution of the continuity equation for the carriers injected at the illuminated surface. We have obtained this solution under the following assumptions:

- a. The magnetic flux density is very small.
- b. The carriers diffuse in one direction only.
- c. Photoinjection and surface recombination can be represented as surface boundary conditions.
- d. Charge neutrality is preserved and results in a relationship between the excess densities of electrons and holes.

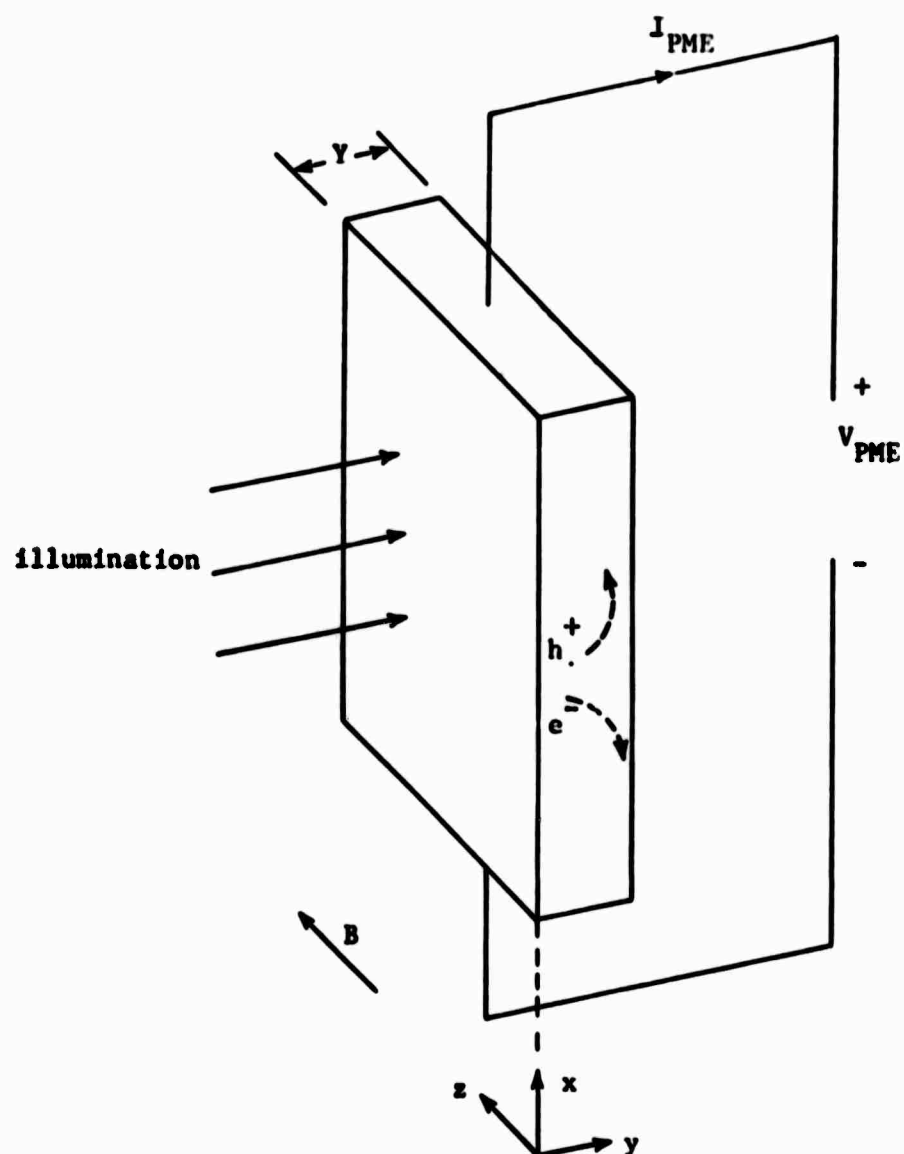


**Fig. 1** Schematic sample configuration for the PME and photoconductivity measurements.

e. The recombination rate is a function of injection only.

f. The injected carriers do not reach the dark surface.

## 2.1 Charge Neutrality

For charge neutrality, the injection dependent densities must satisfy the equation:

$$p + N_{Au}^+ + N_D = n + N_{Au}^- + n_D \quad (1)$$

A detailed solution of this equation is reported elsewhere<sup>5</sup>. Here we only consider the results of direct interest to our experimental work on the PME current and photoconductivity measurements.

Shockley-Read's<sup>6</sup> (S-R model) and Sah-Shockley's<sup>7</sup> (S-S model) statistics are used to relate the densities of the electrons trapped in the impurity centers to the densities of free carriers. A relationship between the excess carrier densities  $\Delta p$  and  $\Delta n$  can be deduced from Eq. (1) by making use of S-R and S-S statistics, which takes the simple form of power laws within certain ranges of injection<sup>5</sup>. Of particular interest here, are the low temperature results. The low and moderate injection solution of Eq. (1) takes the form

$$\Delta p = \Gamma_1 \Delta n + \Gamma_2 \Delta n^2 \quad (2)$$

where

$$\Gamma_1 = |N_D - N_{Au}| / (N_D \gamma_{1/2}) \quad (3)$$

and

$$\Gamma_2 = \Gamma_1 / n_0 \text{ for } N_D > N_{Au} \quad (4)$$

$$\Gamma_2 = N_{Au} / N_D n_{10} \gamma_{1/2} \text{ for } N_D < N_{Au} \quad (5)$$

This solution is valid for

$$0 < \Delta n \ll (\Gamma_2 \sqrt{\gamma_{1/2} \gamma_{-1/2}})^{-1} \quad (6)$$

and can be separated into a small injection linear range (i.e.:  $\Delta p \approx \Gamma_1 \Delta n$ )

and an intermediate quadratic range (i.e.:  $\Delta p \approx \Gamma_2 \Delta n^2$ ).

This analysis also shows that the electron recombination lifetime changes slowly with injection.<sup>5</sup>

## 2.2 Diffusion Equation

The PME current is related to the diffusion current, and the photoconductivity is proportional to the average injected carrier density. The continuity equation for electrons is given by

$$\frac{dJ_{ny}}{dy} + qR = 0 \quad (7)$$

where

$$J_{ny} = qn\mu_n E_y + qD_n \frac{dn}{dy} \quad (8)$$

$$J_{py} = qp\mu_p E_y - qD_p \frac{dp}{dy} \quad (9)$$

The Demer field ( $E_y$ ) in Eqs. (8) and (9) is independent of  $y^1$  and the total current in the  $y$ -direction is zero. With these considerations, Eqs. (8) and (9) can be reduced to:

$$J_{ny} = qD \frac{dn}{dy} \quad (10)$$

where

$$D = D_n \frac{p + n \frac{dp}{dn}}{p + bn}, \text{ and } p = p_0 + \Delta p, n = n_0 + \Delta n \quad (11)$$

is a generalized diffusivity function. The continuity equation in Eq.(7) then takes the form:

$$\frac{d}{dy} \left( D \frac{dn}{dy} \right) + R = 0 \quad (12)$$

The solution of Eq.(12) gives an implicit expression for the carrier profile:

$$y = Y - \int_{\Delta n_Y}^{\Delta n} \left[ \frac{D}{\Delta n_Y} \frac{d\Delta n}{(2\int D R d\Delta n + C_1)^{1/2}} \right] \quad (13)$$



The constants of integration are determined by the boundary conditions at the illuminated and dark surfaces. If the injected carriers do not reach the back surface, the constant of integration  $C_1$  is zero. This can be shown from the boundary condition at this surface:

$$\frac{1}{q} J_{ny}|_Y + S_d \Delta n_Y = 0 \quad (14)$$

Usually the computation of Eq. (13) is only an intermediate step in the calculation of a measurable quantity. Therefore, a complete evaluation of this solution is not necessary.

### 2.3 The PME Effect and Photoconductance

The PME short circuit current, in the limit of small magnetic flux density is:<sup>1</sup>

$$I_{PME} = -\theta \int_0^Y J_{ny} dy \quad (15)$$

where  $\theta = |\theta_n| + |\theta_p|$ ,  $\theta_n = -\mu_{nH} B$ ,  $\theta_p = \mu_{pH} B$ .

For the thick sample, using Eq.(10) we can write

$$I_{PME} = \theta \int_0^{\Delta n_0} q D d\Delta n \quad (16)$$

Similarly the photoconductance can be written as:

$$\Delta G = q\mu_n \int_0^Y \left( \Delta n + \frac{\Delta p}{b} \right) dy \quad (17)$$

or

$$\Delta G = q\mu_n \int_0^{\Delta n_0} \left( \Delta n + \frac{\Delta p}{b} \right) \cdot \frac{D d\Delta n}{\left[ 2 \int_0^{\Delta n} DR d\Delta n \right]^{1/2}} \quad (18)$$

Eqs.(16) and (18) relate  $I_{PME}$  and  $G$  parametrically through  $\Delta n_0$ . In the low injection linear range  $\Delta p = \Gamma_1 \Delta n$ . Solving Eqs.(10), (11), (16) and (17) one finds

$$I_{PME} = \frac{\theta (D_1/\tau_n)^{1/2}}{\mu_n (1 + \Gamma_1/b)} \quad \Delta G = \frac{\theta q D_1 Q_0}{S_1 + D_1/\tau_n} \quad (19)$$

where

$$D_1 = D_n \frac{(n + \Delta n)\Gamma_1}{bn + \Gamma_1 \Delta n} \quad (20)$$

Eq.(19) is consistent with the result obtained by Amith<sup>8</sup>.

Eq.(19) predicts a linear relationship between  $I_{PME}$  and  $\Delta G$ . In this range, the photoconductance, PME current and the photon flux density are proportional to the first power of the surface injection (and therefore to each other). The effective diffusivity ( $D_1$ ) and the lifetime were found to be constant in this range. The linear relationship between  $I_{PME}$  and  $\Delta G$  has been observed recently by Li<sup>4</sup> in n-type silicon at low temperatures.

In the intermediate injection range, where the steady state trapping of photo-injected carriers by gold centers becomes significant, the relation between  $\Delta p$  and  $\Delta n$  is quadratic, i.e.,

$$\Delta p = \Gamma_2 \Delta n^2 \quad (21)$$

By substituting Eq.(21) into (11) and realizing the fact that in this region  $\Delta p \gg p_0$ ,  $\Delta n \gg n_0$  and  $\Delta p < \Delta n$ , the diffusivity function  $D$  in Eq.(11) reduced to the form:

$$D = \frac{3D_n \Gamma_2}{b} \Delta n \quad (22)$$

Substituting Eq.(22) into Eq.(16) yields the PME short circuit current:

$$I_{PME} = \theta \left( \frac{3D_n \Gamma_2 q}{b} \right) (\Delta n_0)^2 \quad (23)$$

And by substituting Eq.(22) and  $R = \frac{\Delta n}{\tau_n}$  into Eq.(18) one finds

$$\Delta G = \mu_n q \sqrt{2\Gamma_2 D_n \tau_n / b} (\Delta n_0)^{3/2} \quad (24)$$

From Eqs.(23) and (24), the relationship between  $I_{PME}$  and  $\Delta G$  is given

in the following form:

$$I_{PME} = \frac{3}{2} (q) \left( \frac{\Gamma_2^D n}{4\tau_n} \right)^{1/3} \left( \frac{\Delta G}{q\mu_n} \right)^{4/3} \quad (25)$$

which predicts a 4/3 power law between  $I_{PME}$  and  $\Delta G$ . This power law relationship was observed in gold-doped n-type silicon at low temperatures as will be reported in the next section.

### 3. Experimental Results and Discussion

We report here the experimental results on three gold-doped silicon samples. The samples were prepared by diffusion of gold into phosphorus-doped silicon bars. The impurity concentrations, listed in Table 1, were estimated from Hall data obtained between 20°K and 300°K.

By comparing the Hall data of the different samples and the gold diffusion data, we have arrived at values for the phosphorus and gold densities as listed in Table I. The activation energy listed is deviated from the accepted value of 0.044 eV for phosphorus at low donor concentrations. However, it is consistent with measurements by Long and Myers<sup>9</sup> of 0.043 eV for a donor concentration of  $4.5 \times 10^{15} \text{ cm}^{-3}$  and by Swartz<sup>10</sup> who obtained 0.032 eV for  $1.8 \times 10^{17} \text{ cm}^{-3}$  of donor concentration. The activation energy of the phosphorus is estimated for samples 1,2 and 3 from the slope of the low temperature plot of  $R_H T^{3/2}$  versus  $1/T$ , which yields a value of 0.033 eV.

To check the adequacy of our model, we investigate the temperature dependence of the PME short circuit current,  $I_{PME}$ , and compare with the theoretical expression. From Eq.(25) we find that

$$I_{PME} \propto \Gamma_2^{1/3} \quad (26)$$

This is the factor that contributes most to the dependence of  $I_{PME}$  on temperature because

$$\Gamma_2 = \frac{N_{Au}}{N_D^{1/2} n_D} \quad (27)$$

Table 1. Impurity concentrations from Hall effect, conductivity and gold diffusion data

	$N_D - N_A$	$E_D$	$N_A$	$N_D$ (est.)	$N_{Au}$ (est.)
Sample 1	$1.7 \times 10^{17} \text{ cm}^{-3}$	33 mev	$10^{16} \text{ cm}^{-3}$	$1.8 \times 10^{17} \text{ cm}^{-3}$	$< 10^{16} \text{ cm}^{-3}$
Sample 2	$8.9 \times 10^{16}$	33	$1.8 \times 10^{17}$	$1.8 \times 10^{17}$	$8 \times 10^{16}$
Sample 3	...	...	...	$2 \times 10^{16}$	$5 \times 10^{16}$

where

$$n_{1D} = N_C \exp[-(E_C - E_D)/kT] \quad (28)$$

Since  $n_{1D}$  decreases exponentially with temperature with the activation energy of the phosphorus level, it is found from Eq. (26) and (27) that  $I_{PME}$  should increase with decreasing temperature with one third of the activation energy of phosphorus. The observed  $I_{PME}$  for  $\Delta G = 0.1$  mho/cm in sample 3 is plotted in Fig. 5. The slope indicated is 0.001 eV which is about one-third of the activation energy we observed for phosphorus. This is in good agreement with the results obtained from the Hall measurements. The experimental procedures for the PME and photoconductance measurements were described in detail previously<sup>3,4</sup>.

In Sample 1, gold was diffused at 1200°C and annealed at 800°C. This resulted in a light compensation by gold. This sample shows normal band conductivity in the liquid hydrogen temperatures. The mobility increases monotonically with decreasing temperature in consistency with the theory for small compensation. The PME short circuit current at 24.7°K is proportional to the 4/3 power of the photoconductance which is consistent with our theory for the range of injection where  $\Delta p \propto \Delta n^2$ . This result is shown in Fig. 2.

Sample 2 was prepared by diffusing gold at 1200°C and then quenching to room temperature. The compensation of phosphorus by gold for this case was about 50 percent. Impurity conduction by hopping was observed below 22°K, mixed impurity and band conduction between 22° and 32°K and normal band conduction above 32°K. The PME current follows the 4/3 power law at 32°K, but shows anomalous behavior below 29.3°K where the impurity conduction becomes important. This anomalous behavior is attributed to the interaction of injected carriers with impurity conduction.

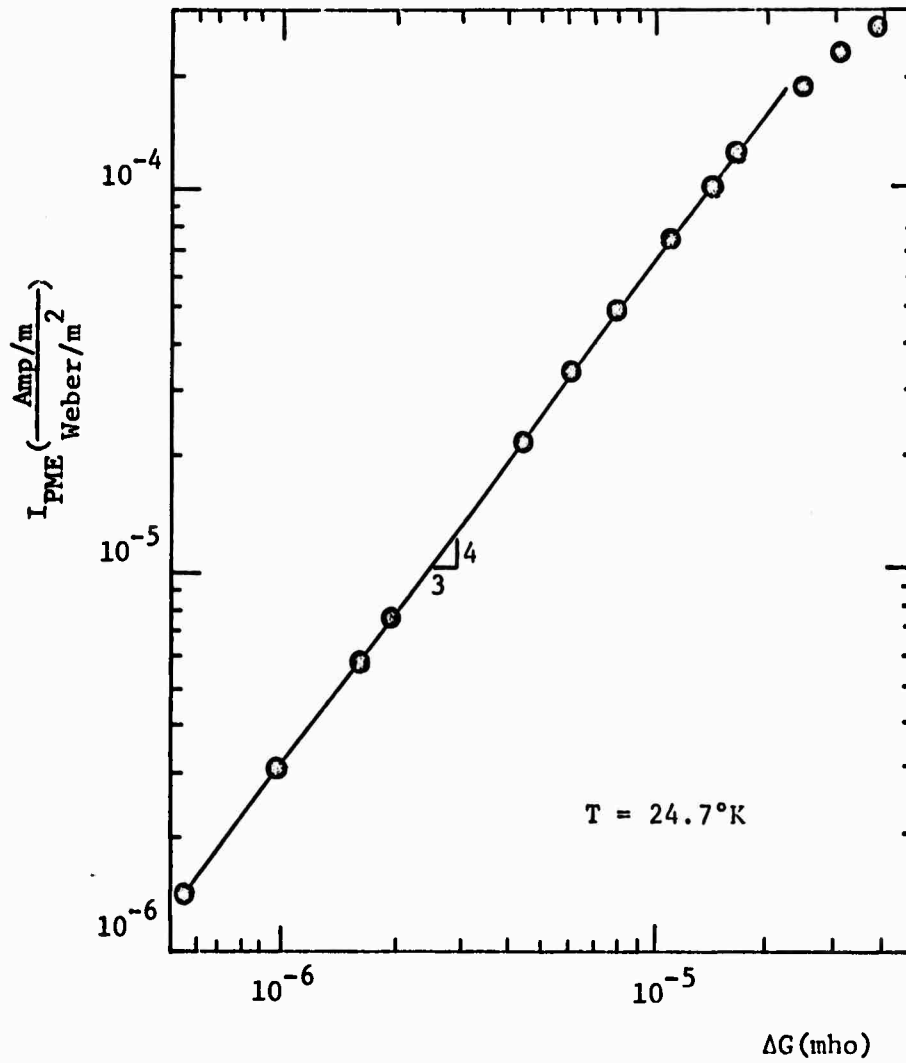


Fig. 2 PME short circuit current versus photoconductance for sample 1.

$$N_D = 1.8 \times 10^{17} \text{ cm}^{-3}, N_{Au} < 10^{16} \text{ cm}^{-3}.$$

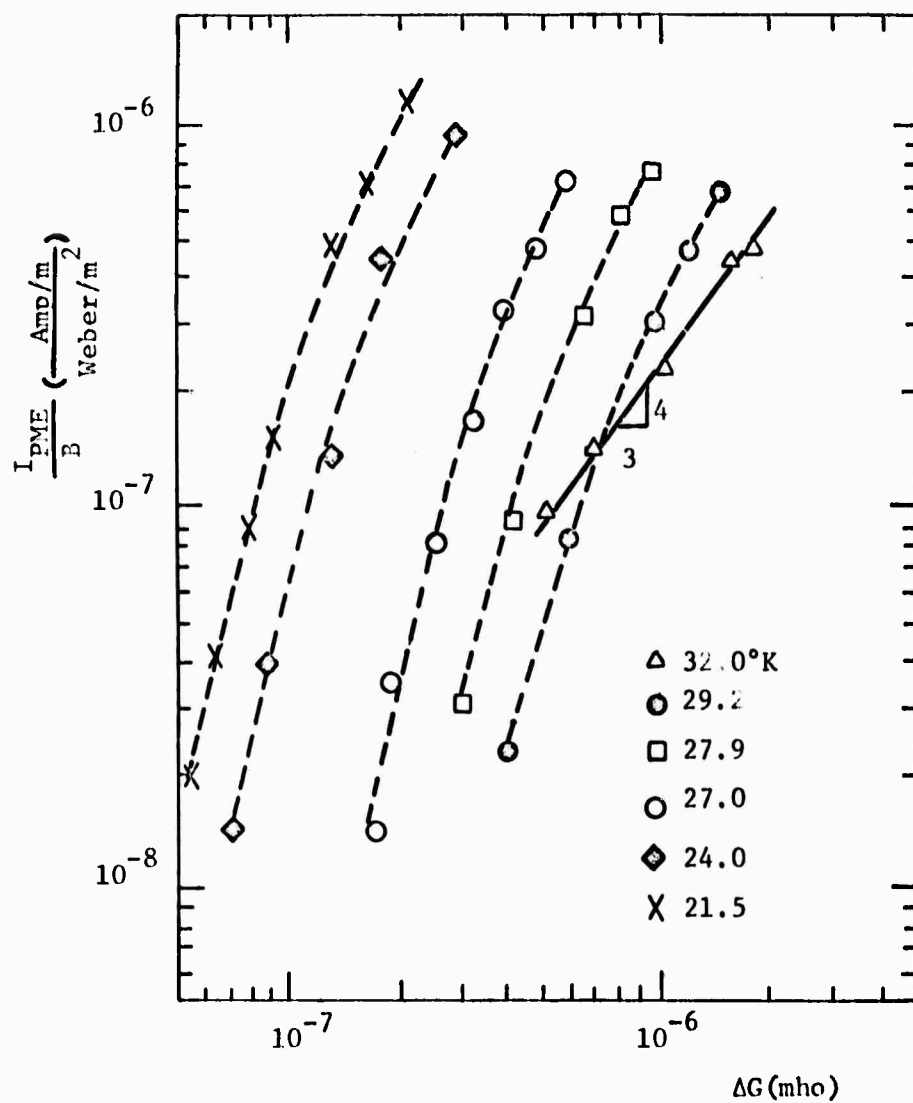


Fig. 3 PME short circuit current versus photoconductance for sample 2.

$$N_D = 1.8 \times 10^{17} \text{ cm}^{-3}, N_{Au} = 8 \times 10^{16} \text{ cm}^{-3}.$$

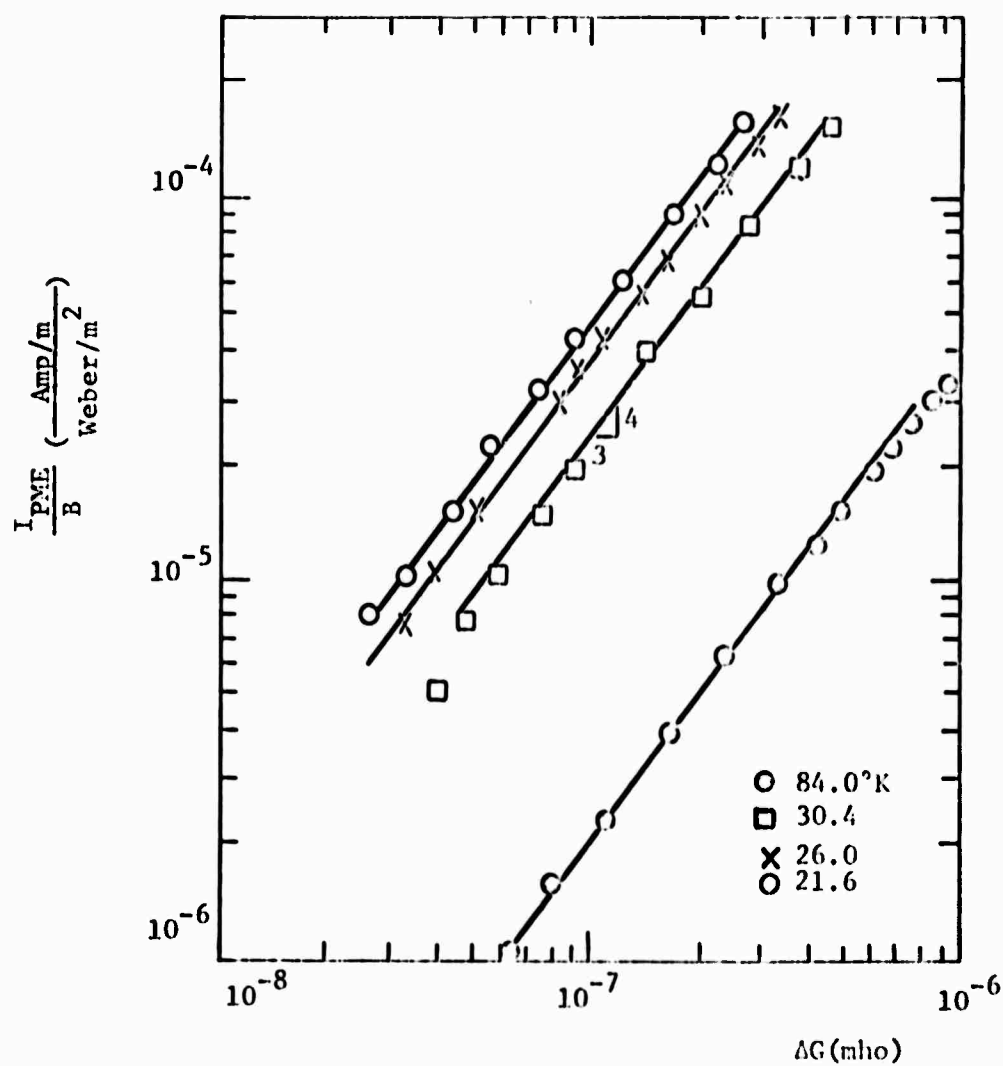


Fig. 4 PME short circuit current versus photoconductance for sample 3.

$$N_D = 2 \times 10^{16} \text{ cm}^{-3}, N_{Au} = 5 \times 10^{16} \text{ cm}^{-3}$$



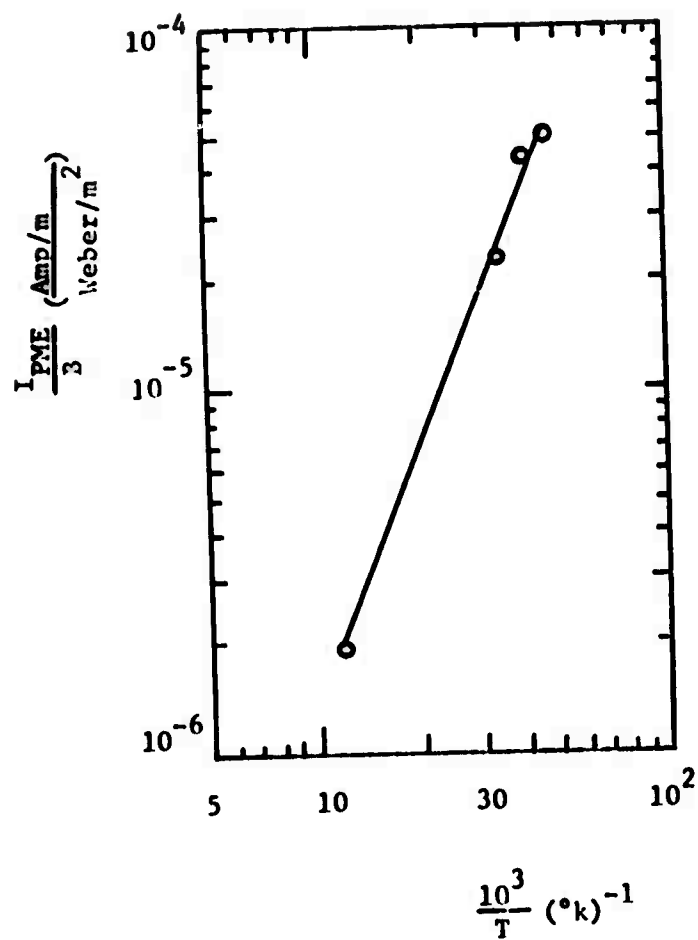


Fig. 5 Temperature dependence of the PME current in sample 3 ( $\Delta G = 0.1 \mu\text{mho}$ ) the slope yields  $E_D = 0.003 \text{ eV}$ .

In sample 3, gold was diffused at 1200°C and quenched to room temperature. The gold overcompensation observed in this sample establishes the gold concentration by this diffusion method at about  $5 \times 10^{16} \text{ cm}^{-3}$ . The 4/3 power law was observed between 20.8° and 84°K in good agreement with our model. (See Eq.(23).)

A nonlinear PME effect in gold-doped silicon has been observed in the injection range characterized by a 4/3 power law for the PME current dependence on the photoconductance. This power law dependence is related to the steady state trapping of the photo-injected carriers by the gold centers. From Eq.(23) and the results shown in Figs. 2, 3, and 4, one can deduce the electron effective lifetime  $\sqrt{\gamma_{1/2}} \tau_n$ . The corresponding values are listed in Table 2.

Since no data are available in literature for the ratio of electron and hole capture rate  $\Gamma_{1/2}$  at the gold acceptor centers at low temperatures, it is impossible to calculate the electron lifetime  $\tau_n$  from the PME and PC measurements for the present case. However, it is possible to determine  $\tau_n$  from photoconductivity decay experiment at low temperature and then calculate the  $\gamma_{1/2}$  from the PME and PC measurements. The increase in temperature of  $\sqrt{\gamma_{1/2}} \tau_n$  for sample 3 is consistent with the fact that  $\gamma_{1/2}$  increases with temperature because  $C_p^+$  increases faster with temperature than  $C_n^x$ .

The PME open circuit voltage observed in the gold-doped silicon is found several orders of magnitude greater than that observed in samples without gold<sup>2,3,4</sup>. The formulation for the steady state diffusion equation shown here is general with respect to trapping and recombination processes.

Table 2. The  $\sqrt{Y_{1/2}} \tau_n$  product.

	T(°K)	$\sqrt{Y_{1/2}} \tau_n$ (μsec)
Sample 1	24.7	63
Sample 2	30.1	0.71
Sample 3	84.0	0.036
	30.4	0.075
	26.0	0.098
	21.6	0.362
	20.8	0.448

#### REFERENCES

1. W. vanRoosbroeck, Phys. Rev. **101**, 1713 (1956).
2. M. Ishigame, Jap. J. of App. Phys. **3**, 720 (1964).
3. S. S. Li and C. Wang, Proceedings of the Conference, Third International Conference on Photoconductivity, Stanford University, August, 1969. Supplements of the J. Phys. Chem. Sol. (to be published).
4. S. S. Li, Phys. Rev. **188(3)** , 1246 (1969).
5. J. Agraz-G and S. S. Li, "Trapping and Recombination Properties of Gold- and Phosphorus-Doped Silicon at Low Temperatures," Phys. Rev. (submitted)
6. W. Shockley and W. T. Read, Jr., Phys. Rev. **87**, 835 (1952).
7. C. T. Sah and W. Shockley, Phys. Rev. **109**, 1103 (1958).
8. A. Amith, Phys. Rev. **119**, 636 (1960).
9. D. Long and J. Myers, Phys. Rev. **115**, 1107 (1959).
10. G. A. Swartz, J. Phys. Chem. of Solids **12**, 245 (1960).

# LIST OF SYMBOLS

$p, n$	=	Total density of holes and electrons, respectively
$\Delta p, \Delta n$	=	Excess density of holes and electrons, respectively
$n_0$	=	Equilibrium electron density
$n_D$	=	Density of electrons in the shallow donor level
$N_{AU}^+, N_{AU}^-$	=	Density of positively and negatively charged gold centers, respectively
$N_{AU}, N_D$	=	Total density of gold and shallow donor impurities, respectively
$\gamma_{1/2}, \gamma_{-1/2}$	=	Ratio of the hole and electron capture rate for the gold acceptor and donor levels, respectively
$R$	=	Recombination rate
$S_d$	=	Dark surface recombination velocity
$Y$	=	Thickness of the sample
$\Delta n_0, \Delta n_Y$	=	Excess electron density at the illuminated and dark surface, respectively.
$\tau_n$	=	Electron recombination lifetime
$b$	=	Electron-hole mobility ratio
$I_{PME}$	=	PME current per unit sample width
$\Delta G$	=	Photoconductance of unit width - unit length sample
$n_{1D}$	=	$N_C \exp[-(E_C - E_D)/kT]$
$S_i$	=	Illuminated surface recombination velocity
$Q_0$	=	Photon flux

**B. IMPURITY CONCENTRATION DEPENDENCE OF THE DENSITY OF STATES IN SEMICONDUCTORS**  
(D. Dale Kleppinger and F. A. Lindholm)

**I. Introduction**

The conventional engineering theory of semiconductors<sup>(1,2,3)</sup> has received wide use in describing the behavior of semiconductor devices. This theory is based on various approximations that make design and analysis manageable; among these approximations is the neglect of the dependence of the density of quantum states on impurity concentration. In predicting the behavior of many semiconductor devices, this neglect introduces no serious error; but for others, in which highly-doped regions play a key role, it may cause the theory to fail utterly in portraying certain aspects of device performance.

That the density of quantum states does indeed depend on impurity concentration is implied by the following experimental evidence. In their study of silicon, Pearson and Bardeen<sup>(4)</sup> found that the impurity ionization energy decreased with increasing impurity concentration. Debye and Conwell<sup>(5)</sup> found the same behavior in germanium. Conwell<sup>(6)</sup> described measurements of carrier concentration and mobility versus temperature and impurity concentration in silicon and germanium. To explain the data, she used a theory that supposed the existence of two species of mobile carriers: the conventional free carriers and carriers in states associated with the impurities. Swartz<sup>(7)</sup> studied resistivity in silicon as a function of temperature and impurity concentration. He found that, depending on temperature and impurity concentration, three modes of conduction can exist: normal band conduction in the states of the host lattice band; non-band conduction (hopping) in states associated with the impurities; and impurity band conduction, again in states associated with the impurities. Finally, measurement of the optical absorp-

tion coefficient for various impurity concentrations gives direct evidence that the band gap, and hence the density of quantum states, depends on impurity concentration<sup>(8)</sup>.

This dependence also manifests itself in device characteristics. By regarding the density of quantum states to depend on impurity concentration, Kane<sup>(9)</sup> has accounted for the non-zero valley current shown by tunnel diodes. Kauffman and Bergh<sup>(10)</sup> and Buhanan<sup>(11)</sup> have explained the observed anomalous temperature sensitivity of transistor gain,  $h_{FE}$ , as being due to a smaller band gap in the heavily doped emitter than exists in the more lightly doped base.

The present paper develops an approach that enables quantitative account to be taken of the relationship between the impurity concentration and the density of quantum states. The approach involves superposing heretofore separate theories concerning the various contributors to this dependence. Combined with a key approximation, which is justified, about the extent of their validity, the superposed theories afford a description for the whole range of impurity concentration that is of technological interest.

Section II below sketches some aspects of the conventional theory. In this section and subsequently, we treat as an example n-type material, unless otherwise indicated; the same treatment holds also, however, for p-type material. Section III focuses on the density of quantum states arising from the impurity atoms; and Section IV focuses on the density of states in the host lattice band. Section V sets forth and justifies the approach by which we combine these contributors to the density of states to yield a comprehensive description of the dependence on impurity concentration. To demonstrate the practical utility of the approach, a prediction based on its use for p-type gallium arsenide is compared in Section VI to an experimental

observation. The approach holds also for material other than gallium arsenide, and Section VII indicates some results to be included in future papers.

## II. Conventional Theory

The conventional engineering theory of semiconductors makes three assumptions about the density of quantum states: The density of states due to the host lattice conduction band is proportional to the square root of energy; the density of states due to the impurity atoms is a delta function positioned in the energy gap and separated from the edge of the conduction band by the ionization energy of the impurity; and, there is no impurity concentration dependence for either of these densities of states. Let us briefly examine these assumptions.

The assumption that the conduction band density of states is proportional to the square root of energy is valid only near the bottom of the conduction band and only for intrinsic material or for material with small or moderate impurity concentration. (The appendix contains a discussion of such relative terms as "small" and "moderate.") At large impurity concentrations the electrons donated to the crystal become so numerous that their interaction with the atomic cores alters the conduction band. The alteration takes the form of a deviation from the square root dependence. This concentration dependent effect is sometimes called the formation of "band tails."

For the contribution to the density of states due to the impurity atoms, the interactions between the individual impurity atoms increase as the concentration increases, i.e., as the average inter-impurity distance decreases. The result of these interactions is like that occurring when many atoms are brought closer together in a conceptual development of crystal properties.<sup>(12)</sup> The energy levels of the individual atoms split and form a quasi-continuous band of



energies, the "impurity band."

The approach to be described provides a means for simultaneous inclusion of the concentration dependence of the band tails and the impurity band.

### III. Impurity States

For small impurity concentrations, implying negligible interaction between impurity atoms, the energy dependence of the impurity states is adequately described by a delta function. As the impurity concentration increases, interaction begins to become important and the (spatially averaged) density of impurity states begins to spread. Most of the states still reside at the non-degenerate level, and the spread occurs around this energy. This approach is based on the calculations of James and Ginzberg<sup>(13)</sup> which dealt with a one-dimensional, random lattice. They found that the density of states is nearly Gaussian in form.\*

For a three-dimensional crystal, the logical extension is to assume that the density of impurity states is still described by a Gaussian whose mean is given by the non-degenerate ionization energy and whose standard deviation depends on impurity concentration. This function will be essentially a delta function at small concentrations and will spread around the non-degenerate ionization energy as the impurity concentration increases. Morgan<sup>(14)</sup> has developed a Gaussian function for describing the impurity states that we will use together with our assumption which places the mean of the distribution at the ionization energy.

Morgan's equation for the density of impurity states is

---

\* Since the impurity atoms are assumed to be randomly distributed, the impurity band resulting from their interactions will vary in width in energy throughout the material. Spatial averaging of this varying width, necessary for comparison to experiments, results in an impurity band that does not have sharp edges but "tails off."

$$\rho(E) = (2N)(2\pi)^{-\frac{1}{2}} \sigma^{-1} \exp\left[-\frac{(E-\mu)^2}{2\sigma^2}\right], \quad (1)$$

where

$$\sigma = \left(\frac{2\pi e^4}{\epsilon}\right)^{\frac{1}{2}} \lambda^{\frac{1}{2}} N^{\frac{1}{2}} \exp\left(-\frac{r_0}{\lambda}\right) (6.2419 \times 10^{11}) \quad (2)$$

and  $\lambda$  is the screening length. Equation (1) has been normalized so that the doubly infinite energy integral of  $\rho(E)$  gives the total number of impurity states,  $2N$  (including spin degeneracy). The equations have been converted from the cgs-esu system of units used by Morgan to a modified cgs-esu system of units in which energy is measured in electronvolts.

Using the screened Coulomb potential screening length for degenerate material,

$$\lambda = \left[2\left(\frac{3}{\pi}\right)^{\frac{1}{6}} \left(\frac{m^*}{\epsilon}\right)^{\frac{1}{2}} \frac{e}{\hbar} N^{\frac{1}{6}}\right]^{-1}, \quad (3)$$

we obtain for Eq.(1)

$$\rho(E) = 3.651 \times 10^8 (\epsilon)^{\frac{3}{4}} \left(\frac{m^*}{m}\right)^{\frac{1}{4}} N \cdot 5833 \exp\left[\frac{-(E-\mu)^2 (\epsilon)^{\frac{3}{2}} \left(\frac{m^*}{m}\right)^{\frac{1}{2}}}{9.551 \times 10^{-18} N \cdot 8334}\right] \quad (4)$$

The units of  $\rho(E)$  are reciprocal electronvolts per cubic centimeter;  $\hbar$  is in erg-sec. Equation (4) has been derived assuming that  $r_0 \ll \lambda$  or, essentially,  $r_0 = 0$ . The quantity  $r_0$  is a radius which Morgan uses to define a sphere near  $r = 0$  where no impurity sites are located. Its value is usually approximately one-half of the lattice constant. Although Morgan points out that  $r_0$  can be used to include skewness in the distribution function, we will consider only a pure Gaussian, leaving for future study the question of the effects of skewness.

#### IV. Conduction Band States

As we noted previously, near the bottom of the conduction band the density of quantum states in the conduction band is proportional to the square root of energy -- but only if the material is, at most, lightly doped. At large impu-

rity concentration, conduction electrons become so numerous that they alter the density of states through their interactions. The main effect resulting from the interactions is the screening of the field contributed by the atomic cores, thereby altering the periodic potential distribution of the system and hence the allowed energies. Bonch-Bruyevich<sup>(15)</sup> has developed a theory which considers this screening and describes the associated density of states in heavily doped semiconductors.

Bonch-Bruyevich deals with semiconductors with very large impurity concentration, i.e., semiconductors in which the impurity band and the conduction band have overlapped. The equation for the density of states in such a material is

$$\rho(E) = \frac{(2m^*E)^{\frac{3}{2}}}{16\pi^{\frac{3}{2}}a^{\frac{3}{2}}\hbar^3} e^{-x} \left[ I_{\frac{1}{4}}(x) + I_{-\frac{1}{4}}(x) + I_{\frac{3}{4}}(x) + I_{-\frac{3}{4}}(x) \right] \quad (5)$$

where

$$x = \frac{E^2}{8a^2}, \quad (6)$$

$$a = \frac{\pi^{\frac{7}{12}} e^{\frac{3}{2}} \hbar^2 N^{\frac{5}{12}}}{2^{\frac{1}{2}} 3^{\frac{1}{12}} \epsilon^{\frac{3}{4}} m^{\frac{1}{4}}}, \quad (7)$$

and the  $I$ 's are Bessel functions with imaginary argument. By making appropriate mathematical approximations, Bonch-Bruyevich reduces this equation to two simpler equations which apply for particular ranges of energy. These equations are as follows.

For energies near the Fermi level the equation becomes

$$\rho(E) = \rho_0 \left( 1 - \frac{a^2}{4E^2} \right) \quad (8)$$

where  $\rho_0$  is the usual parabolic density of states function,

$$\rho_o(E) = [(2m^*)^{\frac{3}{2}} E^{\frac{1}{2}}] [2\pi^2 \hbar^3]^{-1}. \quad (9)$$

Equation (8) shows that near the Fermi level the density of states differs only slightly from that in lightly doped material. It should be recalled that in heavily doped semiconductor material the Fermi level is expected to be in the allowed band. Note that at higher energies the density of states approaches the lightly doped form.

The second simpler equation applies for energies near the conduction band edge.\* The density of states in this energy range will be altered to a greater degree as shown by Eq. (10)<sup>(16)</sup>.

$$\rho(E) = [(2m^*)^{\frac{3}{2}} a^{\frac{1}{2}}] [2\pi^2 \hbar^3 \Gamma(\frac{1}{4})]^{-1} [1 + \frac{\Gamma(\frac{1}{4})}{4\Gamma(\frac{3}{4})} \frac{E}{a}] . \quad (10)$$

This equation is valid for energies greater than  $-E_1$ , where

$$E_1 = [m^* e^4] [2\epsilon^2 \hbar^2]^{-1} (Na_o^3)^{\frac{1}{10}} \quad (11)$$

and

$$a_o = \frac{\epsilon \hbar^2}{m^* e^2} \quad (12)$$

is the first Bohr radius in the crystal. Equation (10) gives a linear dependence on energy for the density of states near the band edge, rather than the conventional square-root dependence.

As has been pointed out above, Bonch-Bruyevich's equations apply to

---

\* Since we will be discussing heavily doped material which has its host lattice band distorted from the intrinsic or lightly doped case, it is necessary to establish a convention. The term "band edge" will refer to the energy at which the density of states becomes zero in non-degenerate or lightly doped material. When it becomes necessary to discuss a band edge in connection with the heavily doped material, the modifier "effective" will be used to avoid confusion. Similarly, the energy reference in this discussion will be the band edge, i.e., energies in the (lightly doped) allowed band will be positive and energies in the (lightly doped) forbidden band will be negative. Both of these conventions will be followed for the conduction band and the valence band.

heavily doped semiconductors. However, an inspection of Eqs. (8), (7), and (11) shows that, as the impurity concentration decreases, the density of states function approaches the intrinsic or lightly doped expression. In view of this behavior, we assume that Bonch-Bruyevich's equations are valid at impurity concentrations below those at which the impurity band has overlapped the conduction band.

### V. The Approach

We seek a description of the density of quantum states applicable for all impurity concentrations. A full and rigorous quantum mechanical treatment of this problem having yet to be done, we make an approximation that employs knowledge available to date. We assume the dependence of the density of states to be given by the superposition of the theories due to Morgan and to Bonch-Bruyevich. Notice that this superposition purports to hold for all impurity concentrations. Upon this point rests the limit of validity of the approximation, for the individual theories themselves hold, strictly speaking, only for restricted ranges of concentration.

To explore the limits of validity, consider the asymptotic behavior. For small impurity concentrations, which were of no interest to Bonch-Bruyevich, observe nonetheless that his equations reduce to the conventional density of states appropriate to a lightly doped semiconductor. So also does Morgan's equation, his Gaussian function becoming narrow and approximating a delta function. For very large concentrations, Bonch-Bruyevich's theory is valid<sup>(15)</sup>. The superposition of Morgan's and Bonch-Bruyevich's equations, however, fails to strictly account for the states in the impurity band having been removed from the host lattice band. This deficiency will introduce negligible error in the calculation of the total density of states provided the impurity concentration remains small compared to the density of host lattice atoms. The same restriction on the impurity concentration is also required by Morgan's theory. For many impurities and semiconductors, the solubility limit of impurities will ensure that this restriction

is not violated. Thus the superposition at large densities introduces practically no error in the total density of states calculated. Nonetheless it could conceivably introduce sizeable error for states near the band edge because it is here that the superposition is influenced comparably by its two components. As will be shown in the following section, however, the superposition predicts a density of states in good accord with an empirically determined density of states for an impurity concentration exceeding the effective density of states ( $N_v$  in the example). For silicon, for example, this is nearly the maximum impurity density seen in the portions of a device that dominate its performance.

From a pragmatic viewpoint, then, the superposition is an approximation that one may expect to serve adequately over the entire range of impurity concentration that is of technological interest.

## VI. The Density of States in p-type Gallium Arsenide

Empirical justification for superposing the theories of Morgan and Bonch-Bruyevich follows from examination of the recent experimental data of Mahan and Conley<sup>(17)</sup>. Using a tunneling theory, Mahan and Conley inferred the density of states in p-type gallium arsenide from measurements of the current-voltage characteristics in gallium arsenide-gold Schottky junctions. They report measurements made with samples containing zinc impurity densities of  $5.4 \times 10^{18} \text{ cm}^{-3}$  and  $9.9 \times 10^{18} \text{ cm}^{-3}$ .

### A. Qualitative Discussion

The density of states that Mahan and Conley infer for the more impure sample is given in Fig. 1, which also shows our resolution of their data into probable components based on the discussion in foregoing sections. The left-hand portion of the Gaussian-like curve was obtained by simply reflecting the right-hand portion about the peak. The next step is to subtract the Gaussian-like curve from the total curve to obtain the third or remainder curve. Notice that this resolution of the experimental data is the reverse of our proposed approach of superposing the results of Morgan and Bonch-Bruyevich. We can identify the Gaussian-like curve

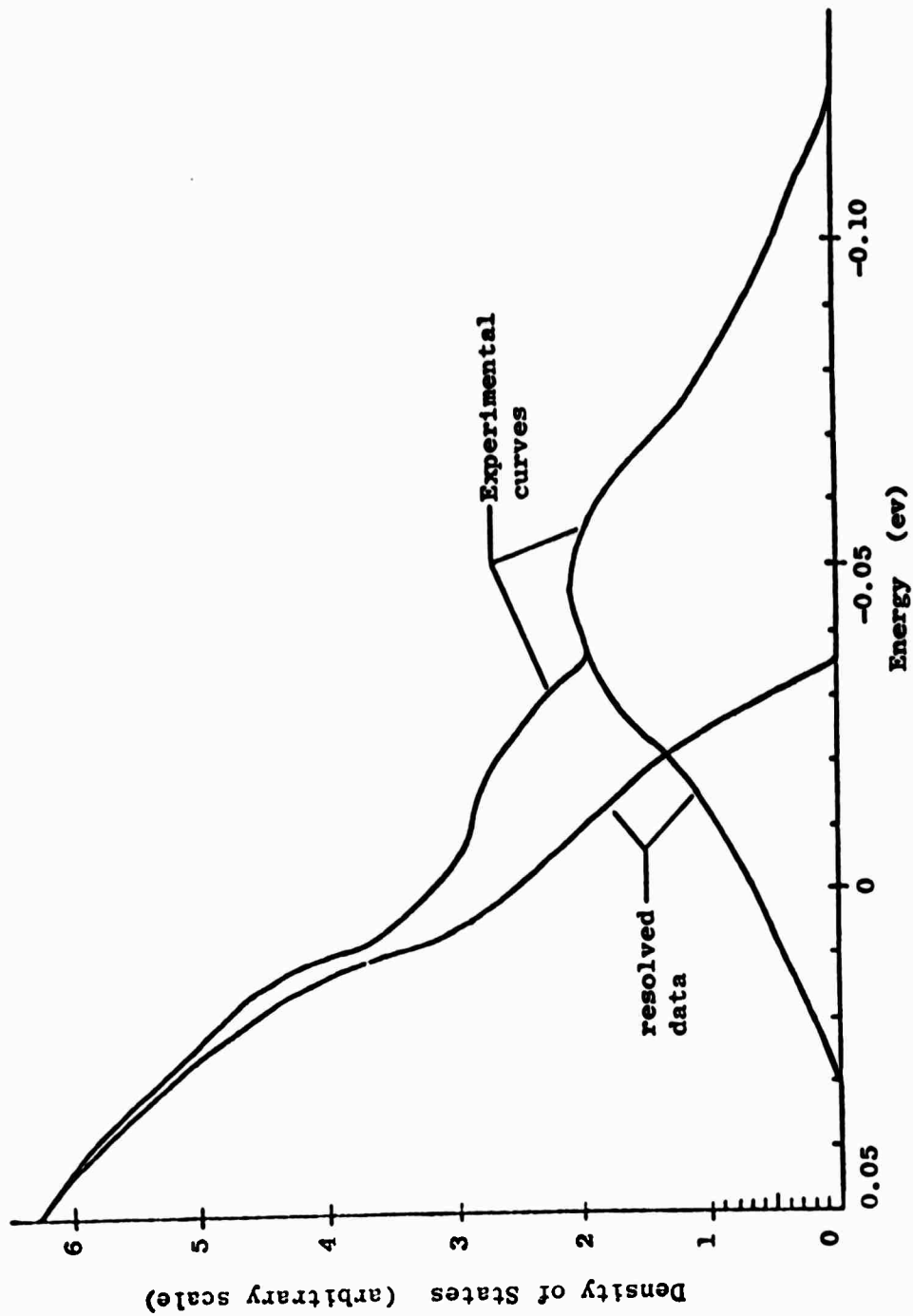


Figure 1. The resolution of the experimentally determined density of states in p-type GaAs. (After G. D. Mahan and J. W. Conley, "The Density of States in Metal-Semiconductor Tunneling," Applied Physics Letters, **11**: 29 (1967).)

with the density of impurity states and the remainder curve as the density of states due to the host lattice band (valence band in this experimental case). Notice that the host lattice states appear as though they can be described by a linear energy dependence near the zero of energy (the band edge) and by a parabolic function beyond the band edge. This observation lends support to our proposed use of Bonch-Bruyevich's results.

Mahan and Conley's data supports our hypothesis that the non-degenerate ionization energy remains the mid-point about which the impurity band develops as the impurity concentration increases. The peak of the Gaussian-like curve occurs at  $-0.04584$  eV for both of their impurity concentrations. The Gaussian-like curve of Mahan and Conley also has a wider spread in energy at the higher impurity concentration than at the lower.

The resolution of Mahan and Conley's data as we have performed it is further supported by an observation of Casey and Panish<sup>(18)</sup>. They state that zinc in gallium arsenide is fully ionized for concentrations greater than  $5 \times 10^{18} \text{ cm}^{-3}$ . Thus we can conclude that the ionization energy has decreased to zero as a result of the overlapping of the impurity and host lattice bands. Both of Mahan and Conley's samples are more heavily doped than  $5 \times 10^{18} \text{ cm}^{-3}$ ; therefore, it is consistent that their density of states data should show an overlapping of the two bands.

The assumption that the mid-point of the Gaussian-like curve,  $-0.04584$  eV, is the lightly doped impurity ionization energy is lent further validity by Huang<sup>(19)</sup>, who places the ionization energy at  $-0.0363$  eV. Since his material was doped at  $5 \times 10^{16} \text{ cm}^{-3}$ , we expect, in view of Casey and Panish's comment, that the ionization energy would have decreased from its lightly doped value. Moreover, Huang states that hydrogenic acceptor impurities are expected to have ionization energies in the range of  $0.030$  eV to  $0.050$  eV in gallium arsenide.

Thus the support for our assumption concerning the mid-point.



## B. Quantitative Discussion

We now compare the quantitative predictions of the approach to Mahan and Conley's experimental data. Before proceeding, however, let us rewrite into convenient forms the equations that we will be using. In the following equations, energies are in electronvolts, concentrations are in reciprocal cubic centimeters, and the density of states is in reciprocal electronvolts per cubic centimeter.

The density of impurity states is given by rewriting Eq. (4) as

$$\rho(E) = 3.651 \times 10^8 \epsilon^{\frac{3}{4}} \left(\frac{m^*}{m}\right)^{\frac{1}{4}} N^{.5833} \exp \left[ \frac{-(E-E_D)^2 \epsilon^{\frac{3}{2}} (m^*/m)^{\frac{1}{2}}}{9.551 \times 10^{-18} N^{.8334}} \right]. \quad (13)$$

In Eq. (13) we have replaced  $\mu$  with  $E_D$  by using our assumption that the impurity band will develop with the conventional ionization energy as its midpoint. The density of states near  $E = 0$  ev is given by Eq. (10) which becomes

$$\rho(E) = 1.309 \times 10^{17} (m^*/m)^{11/8} \epsilon^{3/8} N^{5/24} + 6.267 \times 10^{25} \epsilon^{3/8} (m^*/m)^{13/8} N^{-5/24} E, \quad (14)$$

when the various universal constants are used to evaluate some of the factors.

Similarly, Eq. (8) for the density of states near the Fermi level becomes

$$\rho(E) = 6.8125 \times 10^{21} (m^*/m)^{3/2} E^{1/2} - 4.065 \times 10^3 (m^*/m) \epsilon^{-3/2} N^{5/6} E^{-3/2}. \quad (15)$$

The first term of Eq. (15) is the parabolic density of states function used in the conventional theory.

There are some comments that need to be made about the ranges of validity of Eqs. (14) and (15). For the impurity concentrations that we will consider,

Eq. (14) is valid, according to Bonch-Bruyevich's lower limit  $-E_1$ , for all energies at which  $\rho(E)$  is positive and therefore meaningful. Bonch-Bruyevich, however, does not give an upper limit of validity for Eq. (14), nor does he give a lower limit for Eq. (15). Because of this we have adopted the following scheme. Eqs. (14) and (15) have two intersections at energies above the band edge.\* In the range of energy between these intersections, we apply linear weighting functions to the two equations and use the sum of the weighted equations to calculate the density of states. The weighting functions were chosen to force Eq. (14) to be the only contributor to the sum at the lower energy intersection and Eq. (15) to be the only contributor at the higher energy intersection.

We now compare the predictions of these equations to the experimental data. First, consider the Gaussian-like curve of Fig. 1. The experimental data can be analyzed to find the parameters of a Gaussian function that will then be an approximate mathematical description of the data. The mean of the Gaussian is 0.04584 eV as discussed in Section V. The standard deviation,  $\sigma$ , can be calculated from the data by taking the ratio of two equations of the form of Eq. (1), one evaluated at the mean and one evaluated at the energy that gives the function the value of one-half its peak. This yields

$$\sigma = 0.02799 \text{ eV} \quad (16)$$

for Mahan and Conley's data as resolved in Fig. 1. Morgan's theoretical equation, Eq. (13) yields

$$\sigma = 0.03035 \text{ eV}, \quad (17)$$

when the material parameters of GaAs are used ( $m^* = 0.7132 m^{(20)}$ ,  $\epsilon = 12^{(21)}$ ). The agreement is satisfactory. By using the normalization

---

\* The other intersections do not occur at meaningful energies.

property, we remove the arbitrariness of Mahan and Conley's scale of ordinates. The peak of the Gaussian-like curve is then

$$\rho(\mu) = 1.376 \times 10^{20} \text{ ev}^{-1} \text{ cm}^{-3} \quad (18)$$

Morgan's equation predicts a peak value of

$$\rho(\mu) = 1.401 \times 10^{20} \text{ ev}^{-1} \text{ cm}^{-3}, \quad (19)$$

which agrees satisfactorily with Eq. (18).

Figure 2 shows that Morgan's equation satisfactorily matches our resolution of Mahan and Conley's data. The dashed Gaussian curve is the theoretical prediction of Morgan's equation, while the solid Gaussian-like curve is the resolved data.

Figure 2 also shows a (solid) straight line which has been visually fitted to the resolved curve in the energy range near  $E = 0$  ev. The equation for this straight line is

$$\rho(E) = 3.633 \times 10^{20} + 9.911 \times 10^{21} E, \quad (20)$$

after converting, as described above, from Mahan and Conley's arbitrary scale. Bonch-Bruyevich's equation, Eq. (14) yields

$$\rho(E) = 2.936 \times 10^{20} + 1.013 \times 10^{22} E. \quad (21)$$

The agreement is again satisfactory and within the errors of experiment and graphical analysis. The dashed straight line in Fig. 2 is described by Eq. (21). The downward shift of the theoretical line with respect to the fitted line is approximately 19% at  $E = 0$  ev.

## VII. Discussion

Superposition of the expressions of Morgan and Bonch-Bruyevich yields a description of the density of states in a semiconductor as a function of

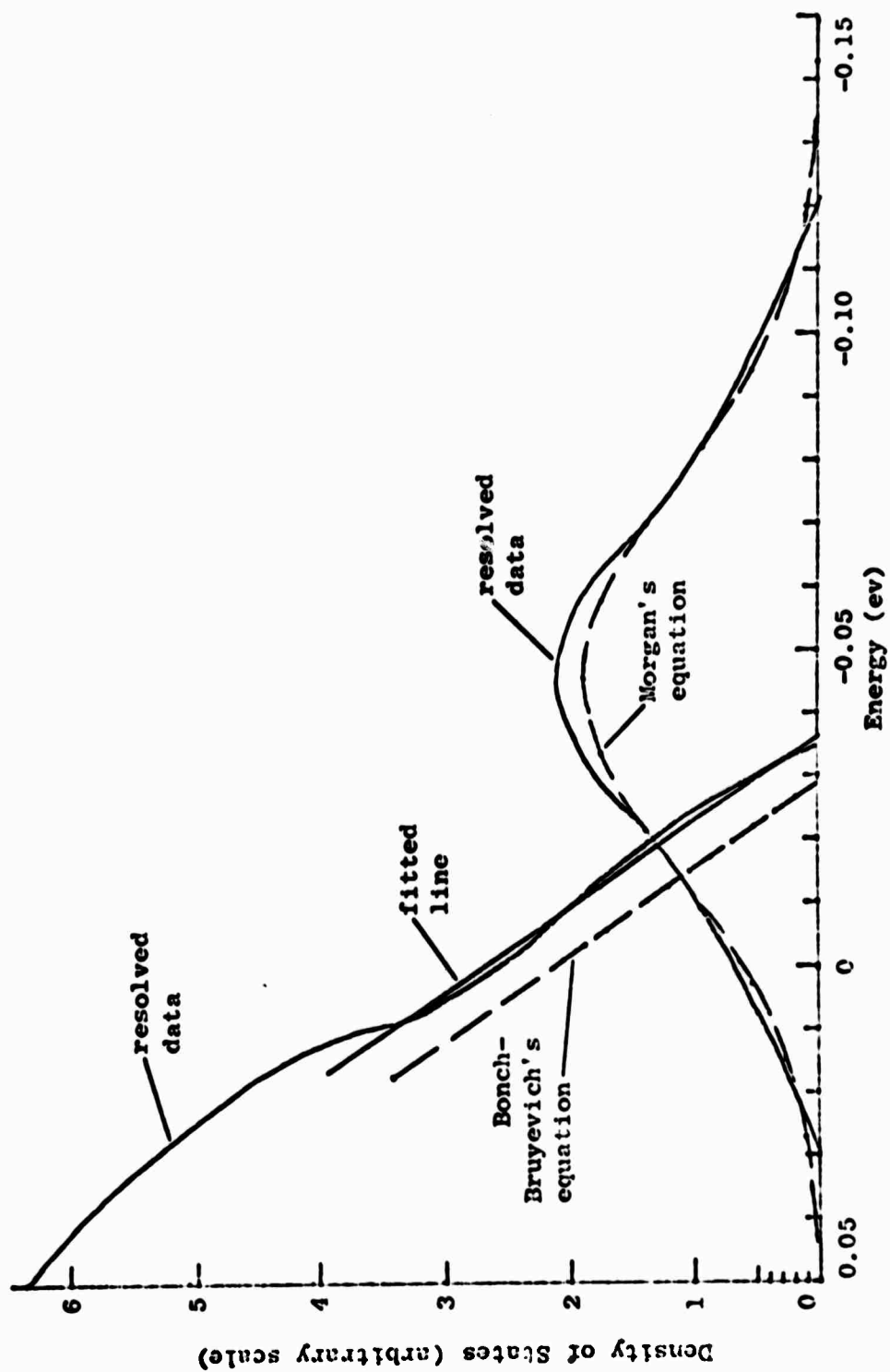


Figure 2. - The comparison of the theoretical and experimental densities of states for p-type GaAs. The example is for  $9.9 \times 10^{18} \text{ cm}^{-3}$  zinc atoms as the impurities.

the impurity concentration. The description is an approximation that one may expect to show the widest discrepancy with reality at asymptotic values of concentration. But for small impurity concentration, the superposition reduces appropriately; and, for large concentrations, the limit of impurity solubility will tend to protect the validity of the approximation. The approach yielded predictions in good agreement with Mahan and Conley's data for p-type gallium arsenide.

From the resultant density of states one can calculate the dependence on impurity concentration of various parameters that interest both the physicist and the device engineer: the Fermi level, transition energies, etc. Though in this paper we have explicitly applied the approach only to p-type gallium arsenide, it applies also to other semiconductors. Subsequent papers will deal with the application to silicon and with the problem of including the complex dependence on impurity concentration in a tractable theory of pn junctions.

## Appendix

The purpose of this appendix is to give some meaning to the relative terms "small," "large," etc., in reference to impurity concentration.

A small impurity concentration is one for which the impurity atoms have a negligible interaction with each other. Then the impurity states may be treated as spatially localized states in which an electron will have a negligible probability of tunneling to another impurity state. At small concentrations the energy spectrum of the impurity states is adequately described by a delta function. Electrical conduction takes place in the host lattice bands.

A moderate impurity concentration is one for which the impurity atoms have a sufficient degree of interaction among themselves that there is a small but finite probability of transfer between impurity states. At temperatures near 0°K, electrical conduction by "hopping" between impurity states will be detectable in this concentration range. The conductivity at these low temperatures will be enhanced by compensating impurities which would have the effect of creating empty states to which hopping can occur.

At the upper end of this moderate concentration range there is a further possible result of the interactions arising because of a difference between the usual tight-binding treatment and the actual circumstances that the impurities experience. (This difference is in addition to the difference in the dielectric medium in the two cases.) The usual assumption in the tight-binding treatment is that the atoms are brought together and formed into a perfect, periodic lattice. This is not the case, however, for impurities in a semiconductor. The impurities assume random, substitutional positions in the host lattice, and, therefore, any given atom interacts to different degrees

with each of its neighbor impurity atoms.\* Hence, along spatial paths of locally large impurity concentration, there will be splitting of the impurity energy levels and the formation of threadlike energy bands through the crystal.

When the impurity atoms interact sufficiently with each other that the impurity states are no longer localized and an impurity band exists quite generally throughout the crystal, the impurity concentration is described as large. In this concentration range the conduction band is noticeably distorted by the formation of band tails. Electrical conduction at low temperatures occurs in the impurity band and is degraded by compensating impurities which act, in this case, to remove mobile carriers from the impurity band instead of providing more available states as compensation does in moderately doped material.

A very large impurity concentration is characterized by the merging of the conduction band states and the impurity band states. The impurity ionization energy has become zero. Electrical conduction in this case has properties which are nearly temperature insensitive and similar to the type of behavior found in metals.

---

\* If the impurities did in fact occur in a perfectly periodic pattern in the lattice, they would not be able to cause the scattering events which manifest themselves as the impurity-determined components of mobility: the ionized impurity and neutral impurity mobilities(15).

### Symbol List

The number in parentheses following the definition indicates the equation in which the symbol is first found. Symbols bearing the subscript "o" designate quantities evaluated in thermal equilibrium unless otherwise specified in the following list. The cgs-esu system is used with the exception that energy is expressed in electronvolts.

$a$	defined in Eq. (7)
$a_o$	the Bohr radius in a crystal (12)
$E$	general energy (1)
$E_1$	defined in Eq. (11)
$E_D$	the energy of the donor level in the forbidden gap (13)
$e$	the magnitude of the electronic charge (2)
$h$	Planck's constant
$\hbar$	$h/(2\pi)$ (3)
$I$	Bessel function with imaginary argument (5)
$m$	free electron rest mass (4)
$m^*$	the density of states effective mass (3)
$N$	impurity concentration (1)
$r_o$	a parameter in Morgan's theory (See text below Eq. (4))
$x$	a normalized energy defined in Eq. (6)
$\epsilon$	the relative dielectric constant (2)
$\mu$	the mean of the Gaussian function (1)
$\rho$	the density of quantum states (1)
$\rho_o$	the parabolic density of quantum states used in conventional theory (8)
$\sigma$	the standard deviation of the Gaussian function (1)
$\lambda$	screening length (2)



## References

1. R. D. Middlebrook, An Introduction to Junction Transistor Theory. Wiley, New York (1957).
2. A. K. Jonscher, Principles of Semiconductor Device Operation. Wiley, New York (1960).
3. A. B. Phillips, Transistor Engineering and Introduction to Integrated Semiconductor Circuits. McGraw-Hill, New York (1962).
4. G. L. Pearson and J. Bardeen, Phys. Rev. **75**, 865 (1949).
5. P. P. Debye and E. M. Conwell, Phys. Rev. **93**, 693 (1954).
6. E. M. Conwell, Phys. Rev. **103**, 51 (1956).
7. G. A. Swartz, J. Phys. Chem. Solids **12**, 245 (1960).
8. V. I. Fistul, Heavily Doped Semiconductors. Plenum Press, New York (1969).
9. E. O. Kane, Phys. Rev. **131**, 79 (1963).
10. W. L. Kauffman and A. A. Bergh, IEEE Trans. on Elec. Devices **ED-15**, 732 (1968).
11. D. Buhanan, IEEE Trans. on Elec. Devices **ED-16**, 117 (1969).
12. J. P. McKelvey, Solid-State and Semiconductor Physics. Harper and Row, New York (1966).
13. H. M. James and A. S. Ginzberg, J. Phys. Chem. **57**, 840 (1953).
14. T. N. Morgan, Phys. Rev. **139**, A343 (1965).
15. V. L. Bonch-Bruyevich, The Electronic Theory of Heavily Doped Semiconductors. American Elsevier, New York (1966).
16. This equation differs from Bonch-Bruyevich's equation 9.6 (Ref. 15) in the prefactor. The present, corrected form is due to Jorge Agraz-G. and was obtained in a private communication.
17. G. D. Mahan and J. W. Conley, App. Phys. Letters **11**, 29 (1967).
18. H. C. Casey and M. B. Panish, Phys. Rev. **162**, 660 (1967).
19. C. J. Huang, J. Appl Phys. **38**, 4811 (1967).
20. S. Wang, Solid-State Electronics. McGraw-Hill, New York (1966).
21. A. S. Grove, Physics and Technology of Semiconductor Devices. Wiley, New York (1967).

### III. Insulating and Semiconducting Glasses (E. R. Chenette, R. W. Gould, L. L. Hench, J. J. Hren)

#### A. DIELECTRIC BREAKDOWN OF CERAMICS (G. C. Walther and L. L. Hench)

##### Introduction

Ceramics are widely used in the electrical industry for insulation, capacitors, and encapsulation. In each of these applications the ceramic material is exposed to a voltage gradient and it must withstand the gradient for the operating life of the system. Failure occurs when an electrical short develops across the material and such a failure is called dielectric breakdown. The voltage gradient, expressed as volts/cm, sufficient to produce the short is termed the breakdown strength of the material.

Breakdown strengths of ceramics vary widely due to many factors. Some of the most important include: thickness, temperature, ambient atmosphere, electrode shape and composition, surface finish, field frequency and wave form, porosity, crystalline anisotropy, amorphous structure, and composition. A detailed characterization of the importance of these factors on breakdown strengths of a variety of ceramics has not been accomplished. A general comparison of several variables can be made from the data accumulated in Table I.

Strengths as large as several million volts/cm are reported for micron thick thin films. Because they are so thin the voltage insulation of such films is small, however. Thus, bulk ceramics of many centimeters in thickness are required to insulate large electrical power voltages. Table I shows that the breakdown strength unfortunately decreases drastically to levels of only several thousand volts/cm for bulk ceramics.

The marked changes in strength occurring with changing thickness are due to changes in breakdown mechanisms. The temperature effects on breakdown

TABLE I

Material	Form	Thickness	Temperature	Breakdown Strength 10 <sup>6</sup> V/cm (D.C.)	Reference
Al <sub>2</sub> O <sub>3</sub>	anodized film	300 Å	25°C	7.0	24
"	"	6000 Å	25°C	1.5	24
"	"	1000 Å	100°C	16.0	38
99.5% Al <sub>2</sub> O <sub>3</sub>	polycrystalline ceramic	0.63 cm	25°C	0.1	39
"	"	"	"	0.18	39
94.0% Al <sub>2</sub> O <sub>3</sub>	"	"	"	0.1	39
"	"	"	"	0.26	39
Alumina Porcelain					
High Voltage Porcelain		0.63 cm	25°C	0.15	40
Steatite Porcelain		"	"	0.15	40
Forsterite Porcelain		"	"	0.10	40
Low Voltage Porcelain		"	"	0.15	40
		"	"	0.03	40
Lead Glass		0.02 cm	25°C	0.25	41
"	"	"	200°C	0.05	41
Lime Glass		0.004 cm	25°C	2.5	41
Borosilicate Glass (BSI)		0.003 cm	20°C	5.8	42
"	"	"	100°C	2.5	42
"	"	0.0005 cm	20°C	6.5	42
Quartz Crystal		0.005 cm	20°C	6.0	43
"	"	"	-60°C	4.1	43
Quartz, fused		"	20°C	6.6	43
"	"	"	-60°C	7.0	43

TABLE I (continued)

Material	Form	Thickness	Temperature	Breakdown Strength 10 <sup>6</sup> V/cm (D.C.)	Reference
NaCl	[100] single crystal	0.002 cm	25°C	2.5	33
"	[111]	"	"	2.2	33
"	[110]	"	"	2.0	33
"	single crystal	0.014 cm	"	1.26	44
KCl	"	"	"	1.11	44
KBr	"	"	"	0.82	44
TiO <sub>2</sub>	single crystal (11 opt. axis)	0.01 cm	25°C	0.02	32
"	(1 opt. axis)	"	"	0.12	32
BaTiO <sub>3</sub>	single crystal	0.02	0°C	0.040	30
"	"	"	150°C	0.010	30
"	polycrystal	0.02	25°C	0.117	21
SrTiO <sub>3</sub>	single crystal	0.046	"	0.414	28
Mica	(muscovite crystal)	0.002	20°C	10.1	45
"	"	0.006	"	9.7	45
PbZrO <sub>3</sub>	polycrystal (0% porosity)	0.016 cm	20°C	0.079	35
"	(10% porosity)	"	"	0.033	35
"	(22% porosity)	"	"	0.020	35

shown in Table I are due to the strong influence of thermal energy on breakdown mechanisms. It is the objective of this paper to review the various theories of breakdown mechanisms and discuss the influence of experimental and materials variables on the magnitude of breakdown strengths obtained for ceramics.

### Definitions

When the temperature (i.e., thermal energy) of the lattice or its electrons reaches a value during the application of an electric field such that the conductivity increases rapidly and results in permanent damage to the material dielectric breakdown occurs. There are three basic types of breakdown called intrinsic, thermal and avalanche breakdown.<sup>1</sup> Historically, there has also been three pseudo-types of breakdown described. The psuedo-types are termed discharge, electrochemical and mechanical breakdown.<sup>2</sup>

Psuedo-types can be considered to be produced by one or more of the three basic mechanisms. Each of the types of failure will be briefly defined and then the fundamental breakdown mechanisms will be discussed in detail.

Dielectric discharge is associated with a gaseous breakdown in the pores or at the surface of a solid material. Electrochemical breakdown is a result of a gradual deterioration of insulating properties through chemical reactions until breakdown occurs by one of the basic mechanisms. Mechanical breakdown is due to cracks, defects and other stress raisers distorting the applied field and thus precipitating failure.

Experimentally, intrinsic breakdown is found to be primarily field dependent in that the applied field determines when the electron temperature reaches the critical level for breakdown. Observations that intrinsic breakdown occurs at or below room temperature and occurs in very short

time intervals, approximately a microsecond or less, is strong evidence that it is electronic in nature. The name "intrinsic" is used because breakdown by this mechanism is independent of the sample or electrode geometry used (provided no field distortion occurs) or of the wave form applied. Hence the value of applied field required to cause intrinsic breakdown at a given temperature is a property solely dependent on the material.

Breakdown observed between room temperature and approximately 300°C is described as thermal breakdown, because reaching the critical thermal energy for breakdown is primarily influenced by the ambient temperature, and not the electric field. Also, thermal breakdown is dependent on the rate of application of the field. Slow increases in field cause breakdown in milliseconds to minutes, with the value of breakdown being influenced by sample geometry. For faster field pulses, breakdown is independent of geometry and breakdown strength increases with shorter pulse times.

Avalanche breakdown is related to intrinsic breakdown in that it occurs at relatively low temperatures and short times. However, thermal properties of the material are used to describe the breakdown behavior, so it is properly a combination of thermal and intrinsic mechanisms. Thin samples, such as dielectric films, undergo avalanche destruction. There is a statistical variation in breakdown strength with short pulses for this mechanism of breakdown.

Pre-breakdown noise is found with slower pulses which indicates a sequential type of lattice destruction is occurring.

### Breakdown Mechanisms

The basic theoretical approach used to describe dielectric breakdown in solids is to develop an energy balance equation of the form

$$A(T_0, F, \alpha) = B(T_0, \alpha) \quad (1)$$

where  $A(T_0, F, \alpha)$  = energy gained by the material from the applied field

$B(T_0, \alpha)$  = energy dissipated by the material

$T_0$  = lattice temperature

$F$  = applied field

$\alpha$  = energy distribution parameter, which depends on the model proposed

Thus  $A = B$  is the limiting condition for breakdown.

### Intrinsic Breakdown

Theories of intrinsic breakdown can be classified as those dealing primarily with the electron-lattice energy transfer and those considering changes in the electron energy distribution in the material.

In electron-lattice interaction models the behavior of the material is approximated by considering a single electron of average  $E$  (i.e.,  $\alpha = E$ ). Consequently, there



is a low electron density, a small probability of electron-electron interaction, and only electron-lattice energy transfer is allowed. The mechanisms contributing to this transfer are:

- (1) Lattice vibrations in a dipolar field
- (2) Electron shell distortion accompanying the dipolar field-lattice vibrations
- (3) Short range electron shell distortion in a non-polar field

The mechanism chosen to describe the electron-lattice energy transfer depends on the model of the material used. The problem is to determine the value of  $E$  required for the energy balance and then to calculate  $F_c$ , the critical field strength, that causes the critical temperature for breakdown,  $T_c$ , to be reached.

One model, called the Fröhlich high energy criteria,<sup>3</sup> assumes that multiplying the number of conduction electrons to a very large value will destroy the lattice. Thus,  $E = I$ , the ionization energy or gap between the valence and conduction band. Breakdown occurs when the ionization rate exceeds the recombination rate causing the conduction electron density to increase irreversibly. Figure 1 shows the energy balance equation schematically. The value of  $E$  at the intersection of the A and B curves indicates the energy an electron must have to be accelerated by the appropriate field,  $F$ . The high energy electron resulting from a recombination collision will have  $E \leq I$  so that only

those fields  $F \geq F_c$  can cause the electron to be accelerated, resulting in another ionization and thus increasing the density of conduction electrons.

The above model has been questioned<sup>1</sup> on the following grounds: (1) An ionization-recombination steady state may not be realizable in the short time before breakdown, and (2) a steady state might not occur physically: the energy balance might be maintained by some non-steady state process such as radiative recombination (i.e., light emitted upon recombination, as observed, but not published, by Kelly).<sup>1</sup>

Another model is the low energy criteria due to von Hippel<sup>4</sup> and Callen.<sup>5</sup> They assumed the limiting condition for breakdown to occur when  $B(E', T_0)$  is a maximum, with  $E'$  being the maximum average electron energy required for steady state conditions. This means that  $F'_c$  is the field needed to accelerate all the conduction electrons against the lattice influence and is also shown on Figure 1. This model faces criticism similar to the above in addition to the improbability of achieving the extremely high field,  $F'_c$ , necessary to accelerate all the conduction electrons simultaneously.

Stratton<sup>6</sup> attempted to extend the above ideas to non-polar materials but agreement between theory and experiment is poor.<sup>1</sup> It should be mentioned that in general the actual breakdown field,  $F_B$ , must be greater than  $F_c$ , the latter being only the value necessary to cause an irreversible imbalance in the energy transfer equation.

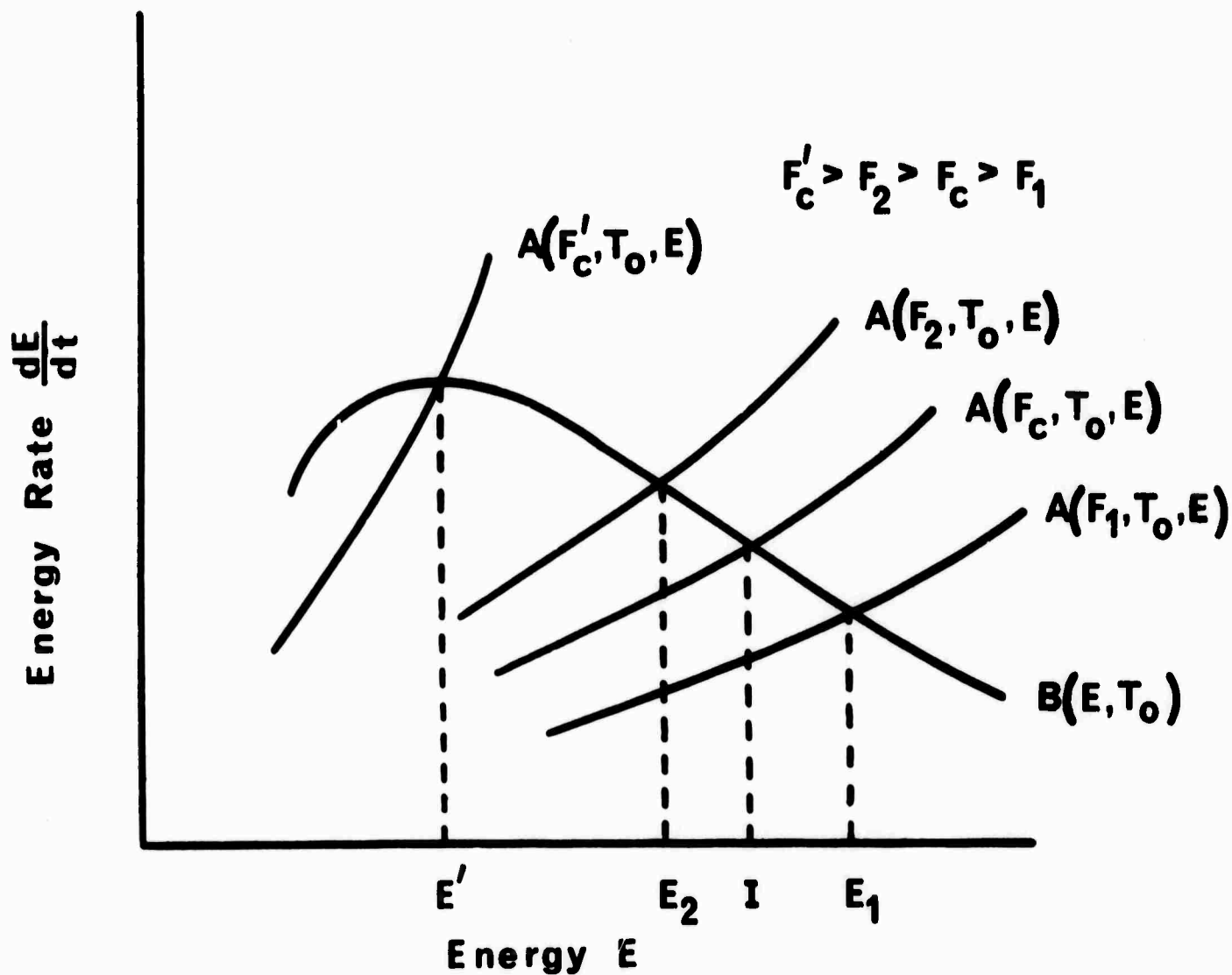


**FIGURE 1**

Schematic representation of the energy balance relation for the Frohlich High Energy Criteria,  $A(F_c, T_0, E) = B(E, T_0)$ , and the Von Hippel-Callen Low Energy Criteria,  $A(F'_c, T_0, E) = B(E', T_0)$ .

Intrinsic theories based on changes in the electron energy distribution of the solid have also been advanced. These theories are based on five contributing factors:

- (1) Acceleration of electrons due to the applied field
- (2) Collisions between conduction electrons
- (3) Collisions between conduction electrons and the lattice
- (4) Ionization or recombination of electrons to and from the valence band or traps
- (5) Diffusion due to a field gradient

This large number of theoretical variables can be reduced by ignoring ionization-recombination processes. This is possible because it can be assumed that most electrons in dielectrics occupy energy states intermediate between those low enough to allow recombination or high enough to permit ionization. The diffusion mechanism can also be dismissed by not considering the influence of the field source.

The energy distribution in the solid can be classified under assumptions of either a low or high density of conduction electrons. Assuming a low electron density permits ignoring electron-electron collisions. For low energy electrons a Boltzmann distribution is obtained. However, for high energy electrons, Fröhlich showed that a valid distribution function could not be described.<sup>7</sup> The distribution approaches infinity with increasing energy unless ionization-recombination properly makes the theory an avalanche type.

For high electron density theories it is assumed that electron-electron collisions are so important that they determine the electron energy distribution. Electron-lattice interactions determine the critical value of electron temperature  $T_c$ , usually greater than the lattice temperature  $T_0$ . Critical conduction electron densities of  $n_c \approx 10^7 \text{ cm}^{-3}$  and  $n_c \approx 10^{14} \text{ cm}^{-3}$  have been calculated for polar and non-polar materials, respectively. Thus for these models,  $\alpha = T_c$  and the breakdown strength is calculated by determining the field,  $F_i$ , necessary to make  $T$  increase to infinity.

An electron density distribution model for a pure crystalline solid has been proposed by Fröhlich and Paranjape.<sup>8</sup> With few or no defects there would be few traps. Consequently, in the energy dissipation function,  $B$ , ionizing collisions were also assumed to be of minor significance and therefore is one point of criticism. Another less than satisfactory aspect of the model is that for  $n_c \approx 10^{17} \text{ cm}^{-3}$  and  $F < F_c$ , the energy gain function  $A$  is a very large value of  $600\mu$  electron volts per ion volume, where  $\mu$  is the mobility. For normal values of  $\mu$  this magnitude of energy absorption would destroy the crystal at less than critical fields.

Fröhlich has also proposed a model for amorphous materials<sup>7</sup> in which he assumes a trap distribution as shown in Figure 2. These are shallow S traps just below the conduction band and deep D traps within the gap. The

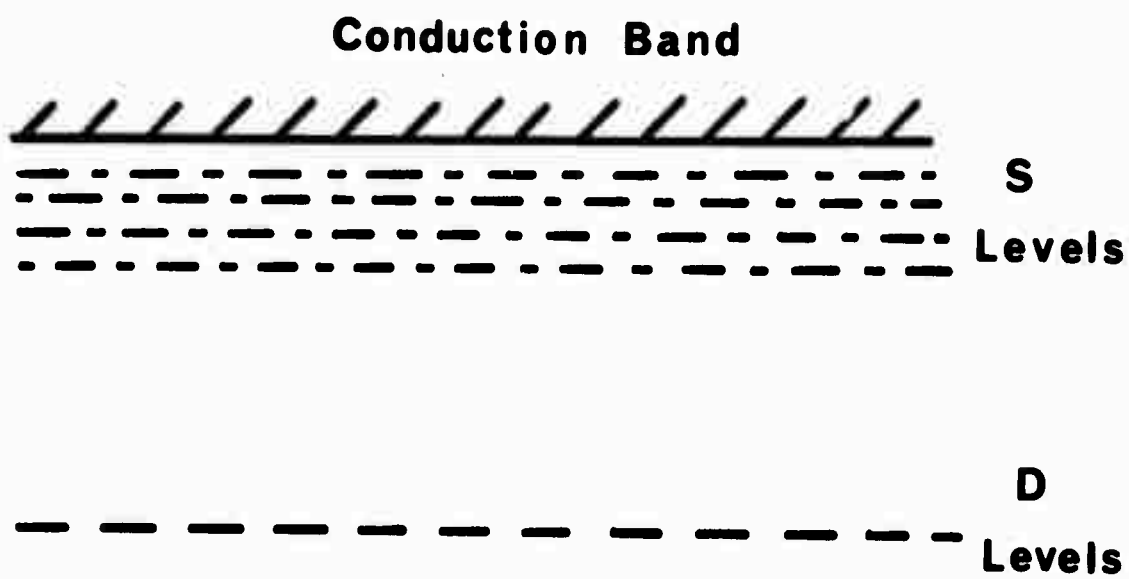


**FIGURE 2**

Trap level representation for the Frohlich amorphous material model.

density of electrons in the traps is  $n_c < n_s \ll n_D$  and  $n_c \approx 10^{17} \text{ cm}^{-3}$ .  $n_c$  plus  $n_s$  thus determines the conduction electron energy distribution and the electron temperature  $T$ . The main mechanism of energy transfer in this model is emission of phonons associated with the change of electrons between  $S$  levels and the conduction band. O'Dwyer has extended this theory to include isolated defect levels in crystals.<sup>9</sup>

Criticism of the amorphous model is centered on the strong possibility of emission from traps, which would change the electron distribution. Figure 2 is also a very idealized distribution of energy levels for an amorphous solid.

The current state of intrinsic breakdown theory thus appears to be that the actual intrinsic breakdown mechanism or mechanisms may be more complex than those proposed by present breakdown models. Further experimental investigation to reduce experimental difficulties may resolve some of the complexity or provide insight into modifications of present theory.

#### Thermal Breakdown

Thermal breakdown theory also is based on an energy balance relation, but it is the balance between heat dissipated by the sample and the heat generated due to Joule heating, dielectric losses, and discharges in the ambient. Hence, it is the lattice temperature and not an electron

temperature that must reach a critical level for breakdown to occur. The influence of the applied field is only indirectly felt as it influences the heat generating mechanisms and does not play the determining role evident in the intrinsic theories based on the electron temperature in the solid. Because of the relatively weak dependence between field and temperature, the value  $T_c$  is not too important and the actual lattice temperature at breakdown,  $T'_0$ , is usually somewhat greater.

The basic relation for thermal breakdown is

$$C_v \frac{dT}{dt} - \text{div}(K \text{ grad } T) = \sigma(F, T_0) F^2 \quad (2)$$

where  $C_v$  = heat capacity of the material

$\text{div}(K \text{ grad } T)$  = heat conduction of a volume element

$\sigma(F, T_0) F^2$  = heat generation term

There is no charge accumulation so the current is continuous.

For slow field applications a steady state is assumed and the  $C_v \frac{dT}{dt}$  term can be ignored. Calculations<sup>2</sup> employing this model show that breakdown strength is inversely proportional to the square root of the thickness. This square root dependence agrees well for thin samples where a uniform temperature can be realized but for thicker samples the breakdown strength is experimentally observed to be inversely proportional to the thickness itself. The criteria for determining if a sample is thick or thin depends on several materials constants, namely the thermal



conductivity as well as the pre-exponential,  $\sigma_0$ , and the activation energy,  $Q$ , for the conductivity-temperature dependence of the solid, i.e.,  $\sigma = \sigma_0 \exp(\phi/kT)$ .

When the field pulse is fast enough, negligible heat transfer can take place. Consequently, the heat conduction term can be ignored and the electrodes only influence the field distribution and not the heat flow, as in the previous case. By integration it is possible to calculate  $t_c$ , the time for breakdown to occur after reaching  $T_c$ :

$$t_c = \int_{T_c}^{T'_0} \frac{C_v dT}{\sigma(F_c, T_0) F_c^2} \quad (3)$$

The strong dependence of  $t_c$  on  $F_c$  is easily seen in the above expression. Similarly, it can be shown that  $F_c = \frac{KT_0}{t_c^{1/2}} \exp(\phi/2kT)$ , thus, the critical breakdown field is essentially independent of  $T_c$ .

Numerical solutions to thermal breakdown models must be used when the field frequency is intermediate and either of the above simplifications can not be made. Each case becomes a different problem with different boundary conditions. Numerical techniques can also be extended to cover multi-dimensional samples or different waveforms with some success. There are no serious criticisms of thermal breakdown theory.<sup>1</sup>

### Avalanche Breakdown

While thermal breakdown theory may be more practical for the application temperatures of many ceramic materials, if the material geometry approaches that of a thin film, avalanche theory may prove more useful. Avalanche breakdown theory is an attempt to combine features of intrinsic and thermal theories since an electron distribution instability will have thermal consequences. The electron behavior is described with an intrinsic theory and the breakdown criteria is based on thermal properties. Avalanche theory considers the gradual or sequential buildup of charge rather than the sudden change in conductivity, even though the charge buildup may occur in a very short time.

Avalanche theories can be easily classed as to their initiation mechanisms which are either field emission or ionization collision. Field emission assumes that the conduction electron density increases by tunneling from the valence band to traps or to the conduction band.<sup>10</sup> Considering that the probability for emission is

$$P = aF \exp(-bI^2/F) \quad (4)$$

shows that  $P$  is small until  $F$  is quite high ( $a$  and  $b$  are constants). Using this development gives an order of magnitude calculation of  $F = 10^7$  volts/cm, with the impulse thermal criteria  $T = T_c$  being the critical parameter. Criticism of initiation by field emission may be made on

at least three points: (1) there should be field emission only for gaps of 1 eV or less, i.e., for semiconductors, or there (2) may be emission from traps, and (3) thermal or phonon assisted emission is not included.

The simpler single electron approach to an ionization collision theory seems to be preferred to the more complex many electron or avalanche multiplication view. The single electron model assumes that at least  $10^{12}$  conduction electrons per  $\text{cm}^3$  are needed to disrupt the lattice.<sup>11</sup> When one starting electron-ionizing collision liberates two electrons, which in turn liberate four and so on, it will take about 40 such collisions to achieve breakdown. This simple approach gives a critical field  $F_c$  that is dependent on thickness: the sample must be thick enough to have at least 40 mean free path lengths. However, the sample can not be so thick that the conduction electron density becomes so large that electron-electron collisions occur, thus limiting the electron energy to that below the ionization level.

The many electron avalanche theory gives a relation between the electron energy distribution function and the ionization-recombination rates. There are two views of this approach to dielectric breakdown. One, due to Heller,<sup>12</sup> assumes that the ionization rate is so large that recombination can not keep up. It is assumed in the other model by Franz<sup>13</sup> and Veelke,<sup>14</sup> that recombination can be dismissed since ionization increases the number of conduction

electrons so rapidly that no recombination mechanism can quench the process. The actual case is likely to be a combination of the two. The electron source is ignored because the density of the source electrons has no relation to  $F_c$ .

Criticism on several points makes the simpler single electron theory appear more realistic than the ones involving multiple processes. The multiple electron theory is limited to short path lengths because breakdown should occur before electron interactions become important. The imbalance between ionization and recombination is due to rapid saturation of traps, which is always unstable, or to some emptying mechanism, which is unstable only if traps empty faster than they fill. Traps might fill with pre-breakdown avalanches having slow decay times but phosphorescence studies show the high instability of traps, which is important for this theory. Also, the electron energy distribution occurs only from electron-lattice collision so that the electron density is lower than the Fröhlich-Paranjape collective avalanche proposal.<sup>7</sup> Finally, the effects of the cathode on such a short path of ionization avalanche is ignored.

O'Dywer has recently proposed a space charge modified field emission model<sup>15</sup> for avalanche breakdown. His criticism of the single electron or 40 generation model is based on its lack of a continuity of current. Assuming that the freed electrons and holes occurring after the fortieth collision form a parallel plate capacitor,

calculations show that a field of  $10^{11}$  v/cm would be needed to maintain this charge separation. Since such a large breakdown strength is not observed, he suggests a continuous current model involving cold cathode field emission with collision ionization occurring after emission, for short breakdown times. Only electrons of energy  $kT$  (i.e., room temperature) are assumed to be accelerated by the field to the ionization level, although intermediate electron energies could cause ionization or some electrons with sufficient energy might not. Calculation of a field versus distance relation<sup>15</sup> indicate that a space charge of low mobility holes is influencing the field distribution and hence breakdown strengths, as seen by the drop in field near the cathode, shown in Figure 3. Comparison of the theoretical results with  $Al_2O_3$  and NaCl thin film breakdown data gives good agreement. The influence of space charge on the temperature dependence at higher temperatures is not known.

This approach combines features of field emission and ionization collision which were mutually excluded in previous proposals. It is therefore potentially subject to the same criticism as the other theories although it does account for thickness dependence and cathode effects. Several experimenters who were inclined to interpret their results in terms of field emission or ionization collision<sup>16,17</sup> before this theory appeared are now willing to consider the effect of space charge<sup>18,19</sup> or at least of the possibility

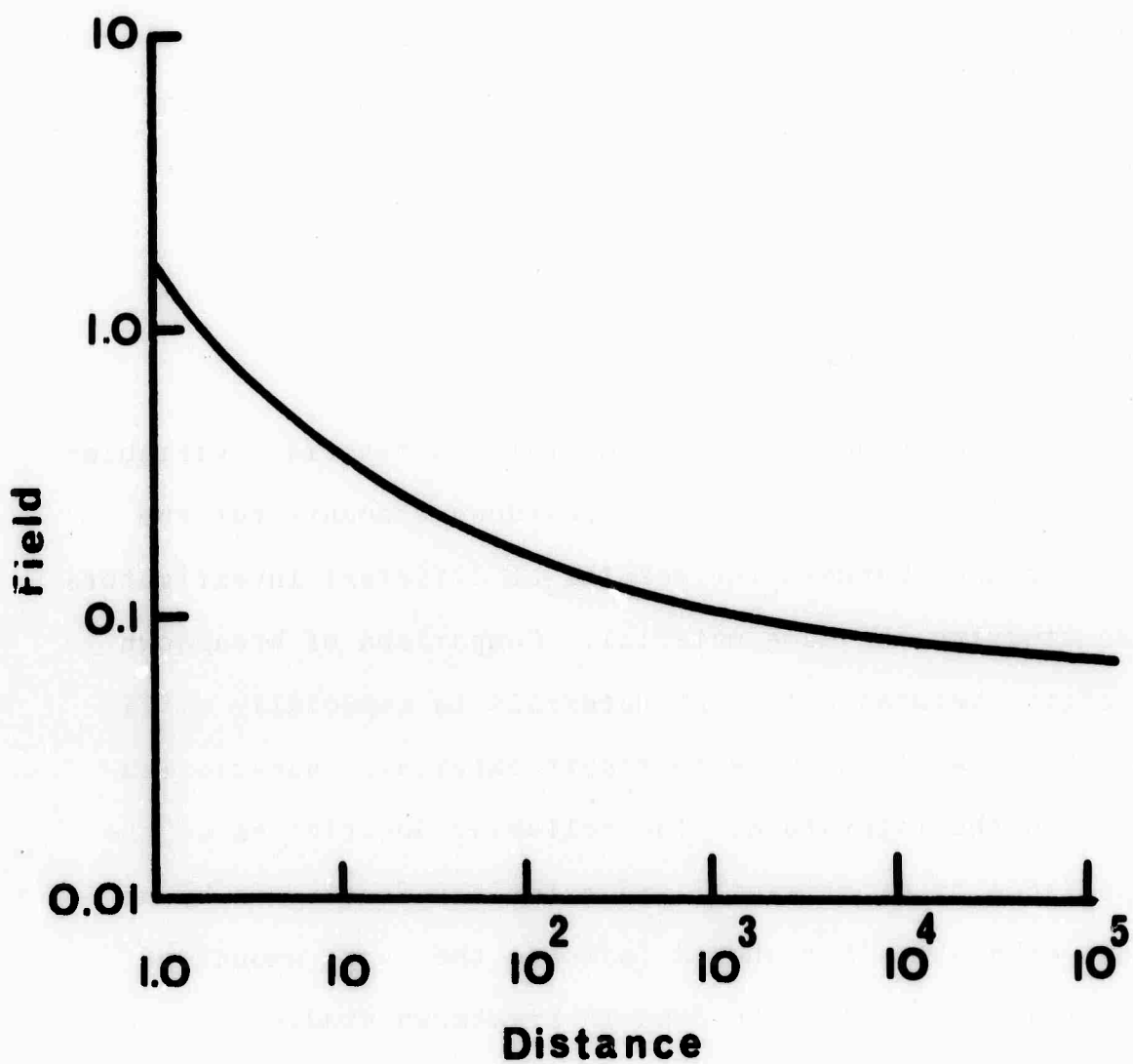


**FIGURE 3**

Representation of the field gradient calculation of O'Dwyer showing the drop in potential in the dielectric due to formation of a space charge with distance from the cathode.

of both mechanisms.<sup>20</sup> Others<sup>21,22</sup> also feel that space charge is worth considering as a possible mechanism. In addition, it appears Mott feels such a mechanism is probably responsible for switching effects in some amorphous semiconductors.<sup>23</sup>

#### Experimental Variables

The great number of experimental and materials variables that can influence dielectric breakdown accounts for the wide variance between the results of different investigators when studying the same material. Comparison of breakdown strengths between different materials is especially difficult because of failures to report materials characterizations in the literature. The following description of the importance of experimental and materials factors is by no means exhaustive but should indicate the large amount of work that is still to be done in breakdown studies.

Sample geometry influences field distribution and heat dissipation considerably. The geometric parameter of major study has been the thickness of the breakdown path on the breakdown strength. Figure 4 shows a general result for thin films<sup>16,24</sup> and indicates that the breakdown strength decreases sharply with distance at some critical value. The same general pattern is observed for thicker specimens,<sup>25</sup> although some doubt has been raised with regard to amorphous materials.<sup>26</sup>

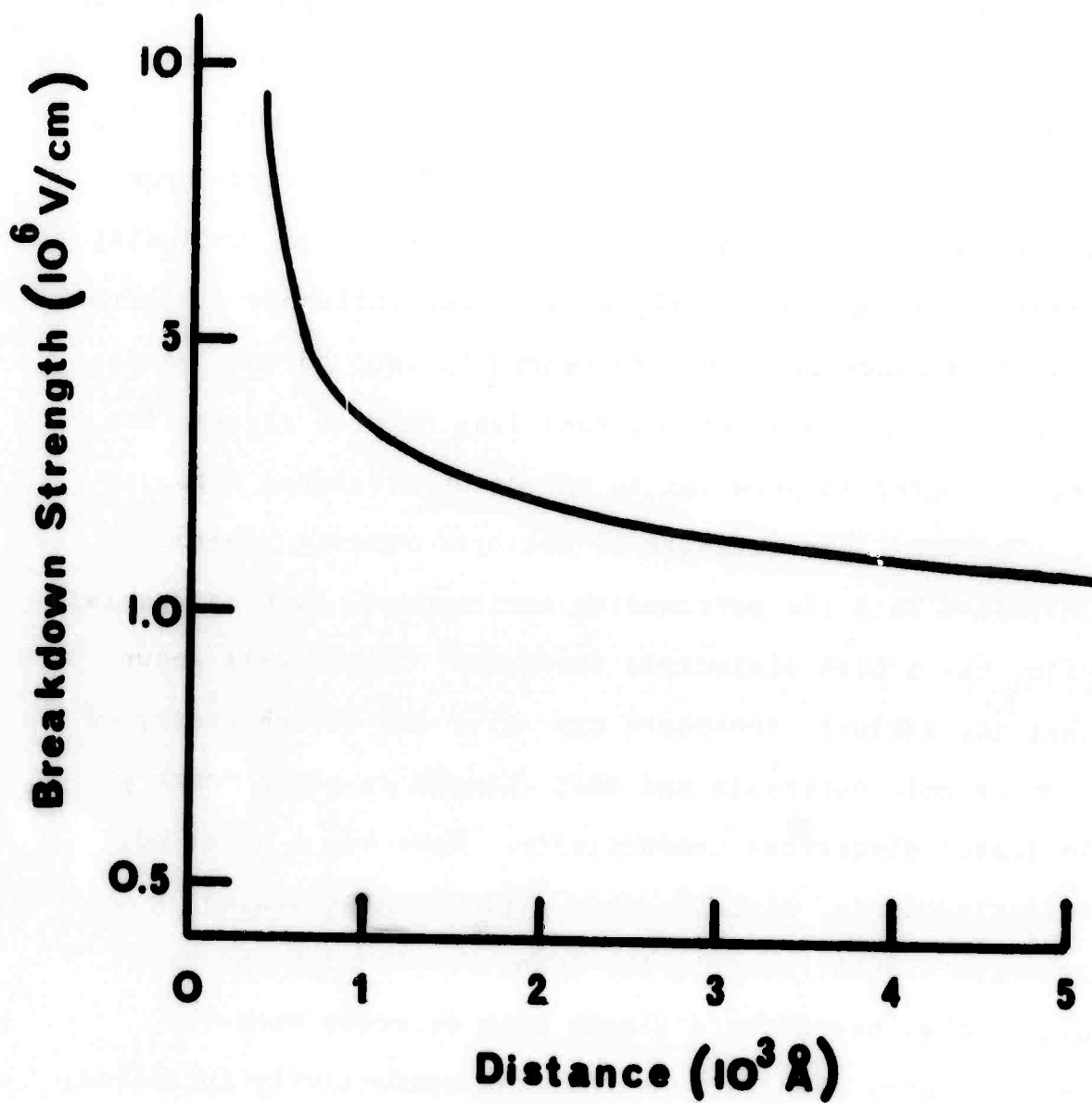


**FIGURE 4**

Thickness dependence of breakdown strength typical of thin films.



A curve showing the general temperature dependence of many materials is shown in Figure 5. In the low temperature region the breakdown strength increases with increasing temperature and then declines with further increases. The location of the maxima depends on the material and large deviations from this pattern have been reported, including temperature independent regions.<sup>21</sup> The influence of thermal history appears to have been generally ignored as a variable, although the affect of annealing on some glasses has been reported to have little effect on breakdown strength.

The breakdown strength of measured samples generally increases when the surrounding environment, such as special oils, has a high dielectric strength.<sup>2</sup> It is well known that the ambient atmosphere can alter the stoichiometry of many ceramic materials and that changes in stoichiometry influence electrical conductivity. However, a detailed investigation of stoichiometry effects on breakdown strength is not known to the authors. It might be predicted that breakdown strength will decrease when the stoichiometry changes such that the conductivity increases.

The applied field itself is an important parameter, in that not only its magnitude, but its frequency, duration, waveform, and distribution can also be varied. This can be very important, especially for intrinsic type breakdown, which is directly field dependent. In general, it has been observed that dc fields produce lower breakdown strengths than ac fields for thin specimens.<sup>27</sup> The reverse

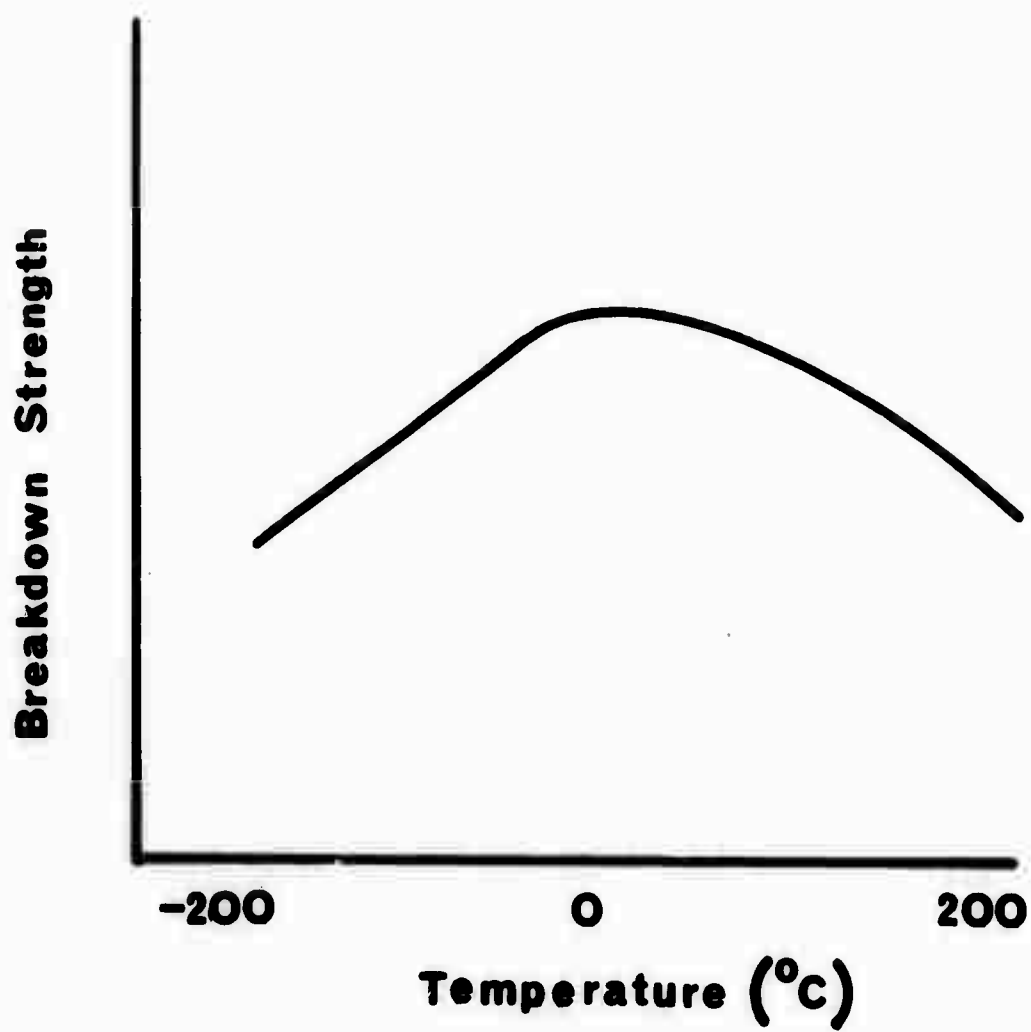


**FIGURE 5**

Nominal temperature dependence of breakdown strength for many materials.

is true for thick specimens due to dielectric heating and poor heat dissipation. The greatest discrepancies to this generalization occur at very high and very low frequencies. Many researchers have used squarewave pulses, either singly<sup>28</sup> or in series, to determine intrinsic breakdown and they observe that increased breakdown values are obtained with shorter pulses<sup>26</sup> and faster rise times.<sup>29</sup> Prestressing, or applying a field less than breakdown for some time, has received too little attention, especially since the influence of space charge on breakdown strength is being considered more favorably. Experiments on glass indicate a very definite influence of prestressing<sup>22</sup> and it has been observed for some time that there is a threshold field such that application of a lesser field will not cause breakdown in any time interval.<sup>2</sup>

The electrodes used for determining breakdown strength have received much attention from investigators. Vacuum depositions of aluminum or gold appear to be the most reliable electrode metal<sup>30</sup> while electrolytes or graphite may be suitable in certain cases.<sup>17</sup> Even the polarity can make a difference if the electrode geometry does not provide a uniform field intensity,<sup>19</sup> especially in light of space charge considerations. The observation of micro-projections 40-500 Å high on thin film electrodes<sup>19</sup> and evidence of current asymmetry due to such projections<sup>31</sup> lends further support to theories based on field emission.

Electrode configuration has been a subject of concern for many years. However, for thick samples a cup and plate electrode, shown in Figure 6, approximating a sphere and plate configuration, appears to give fairly reliable results.<sup>28</sup> Generally, the values of  $t$  and  $r$  are about 0.1mm. The ratio  $d/t$  must be varied with temperature to obtain reliable results: It should be about 4/1 at room temperature but increased to 12/1 at  $-195^{\circ}\text{C}$ , to avoid breakdown at the edges of the sample. For amorphous materials even thicker or diffusely deposited electrode edges may not prevent breakdown over undesired paths.<sup>32</sup> The success with electrolytes and the effect of projections shows the importance of having good contact between the electrode and the sample.<sup>29</sup> Even the electrode area can influence results, as shown by a study of the anisotropy of breakdown in single crystals.<sup>33</sup>

The most important factor to characterize accurately, the dielectric material being investigated, has had very little systematic investigation. In glasses, it is generally found that the effect of composition on breakdown strength follows the change in resistivity with additions of alkali ions.<sup>2,22</sup> Less is known about compositional effects in ceramics, either as impurities or mixtures. The influence can be great as is shown by the investigation of La additions to  $\text{Ba}_{1-x}\text{La}_x\text{ZrO}_3$ .<sup>34</sup> For  $x = 0.06$  the breakdown strength increased 175%, apparently due to electron-hole recombinations reducing the conductivity. A

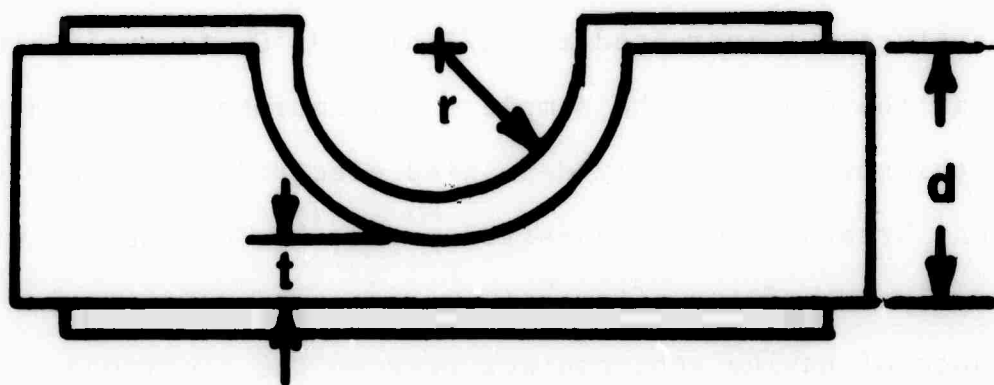


**FIGURE 6**

Typical sample and electrode configuration for dielectric breakdown measurements.

similar effect was observed for additions of Nb in place of Zr.

There is practically no specific information on microstructural effects on breakdown strength known to the authors. Aside from observing that extrusion affects the material texture, particle alignment, stress distribution and hence breakdown strength of a material,<sup>29</sup> the only detailed paper is concerned with porosity.<sup>35</sup> The investigators found a sharp increase in the statistical distribution of voids in the direction of the breakdown path. Experiments with Lucite spheres burned out of  $\text{PbZrO}_3$  yielded fairly good agreement with the theoretical model proposed for porosity effects.

Investigations concerned with the influence of particle size, glassy phase, and phase distributions are apparently absent from the literature.

Other material properties that should be examined with respect to dielectric breakdown are surface condition or grain boundary effects; point defects; dislocations; and dielectric permittivity, which appears to be related to breakdown, in  $\text{BaTiO}_3$ .<sup>21</sup> There is evidence, for example, that dislocations increase the free charge in dielectrics<sup>36</sup> and consequently grinding, polishing, surface treatments or mechanical history can influence breakdown behavior.

Several of the above-mentioned experimental parameters are inter-related and others might also be mentioned, but it is apparent that materials studies have lagged far

behind theoretical studies of dielectric breakdown. This is unfortunate because the theoretical models may well have overlooked critical materials parameters from a lack of such data.

### Conclusions

The conclusions that can be stated are similar to recommendations for future work. Assumptions made in the theoretical approaches often limit calculations to order of magnitude results, although including the effect of space charge in modifications of current theories may produce improvements. The influence of prestressing and microstructure on dielectric breakdown definitely need attention, as well as less directly related phenomena, such as radiative recombination. Finally, full characterization of the materials investigated and experimental conditions must be reported to make worthwhile comparison of results practical.

## LIST OF REFERENCES

1. O'Dwyer, J. J. The Theory of Dielectric Breakdown of Solids. Clarendon Press (1964).
2. Whitehead, S. Dielectric Breakdown of Solids. Oxford Press (1951).
3. Fröhlich, H. Proc. Roy. Soc. A, 160 (1937) 230.
4. von Hippel, A. Ergebn. exakt. Naturw. 14 (1935) 79.
5. Callen, H. B. Phys. Rev. 76 (1949) 1394.
6. Stratton, R. Progress in Dielectrics. Vol. 3. John Wiley and Sons (1961).
7. Fröhlich, H. Proc. Roy. Soc. A, 188 (1947) 521.
8. Fröhlich, H. and B. V. Paranjape. Proc. Phys. Soc. B, 69 (1956) 21.
9. O'Dwyer, J. J. Proc. Phys. Soc. B, 70 (1957) 761.
10. Franz, W. Handbuch der Physik. ed. Flugge, Berlin (1956).
11. Seitz, F. Phys. Rev. 76 (1949) 1376.
12. Heller, W. R. Phys. Rev. 84 (1951) 1130.
13. Franz, W. Z. Phys. 132 (1952) 285.
14. Veelken, R. Z. Physik. 142 (1955) 476.
15. O'Dwyer, J. J. J. Phys. Chem. Solids. 28 (1967) 1137.
16. Korzo, U. F. and A. I. Korabov. Sov. Phys. Solid State. 8 (1966) 494.
17. Vorob'ev, G. A. and L. G. Nekrasova. Sov. Phys. Solid State. 7 (1965) 800.
18. Korzo, U. F. Sov. Phys. Solid State. 10 (1968) 1256.
19. Vorob'ev, G. A. Sov. Phys. Solid State. 10 (1968) 203.



20. Vorob'ev, G. A. Elektrichestvo (U.S.S.R). 12 (1967) 14.
21. Ueda, I., et al. J. Phys. Soc. Japan. 19 (1967) 1267.
22. Sutton, P. M. Progress in Dielectrics. Vol. 2. John Wiley and Sons (1960).
23. Mott, N. F. Contemp. Phys. 10 (1969) 125.
24. Korzo, U. F. Sov. Phys. Solid State. 9 (1968) 2167.
25. Pikalova, I. S. Sov. Phys. Solid State. 8 (1967) 1784.
26. Weaver, C. and J. E. S. MacLeod. Brit. J. Appl. Phys. 16 (1965) 441.
27. Klein, N. and N. Levanon. J. Appl. Phys. 38 (1967) 3721.
28. Barrett, H. H. J. Appl. Phys. 35 (1964) 1420.
29. Ingles, T. A. J. Brit. Cer. Soc. 3 (1966) 135.
30. Branwood, A., et al. Brit. J. Appl. Phys. 13 (1962) 528.
31. Gershinskii, A. E. and E. G. Kostsov. Sov. Phys. Solid State. 10 (1968) 200.
32. Powers, D. A. and I. J. T. Johansen. J. Appl. Phys. 32 (1961) 1083.
33. Vorob'ev, A. A., et al. Sov. Phys. Solid State. 4 (1963) 1441.
34. Koenig, J. and H. Jaffe. J. Amer. Ceram. Soc. 47 (1964) 87.
35. Gerson, R. and T. C. Marshall. J. Appl. Phys. 30 (1959) 1650.
36. Graham, R. A. J. Appl. Phys. 33 (1962) 1755.

37. Bogdanov, S. V. Sov. Phys. Solid State. 4 (1963) 1596.
38. Kawamura, H. and K. Azuma. J. Phys. Soc. Japan. 8 797.8 (1953).
39. Gitzen, W. H. "Alumina Ceramics." Technical Report AFML TR-66-13, Jan. 1966, p. 167.
40. Thurnauer, H. "Ceramic Dielectric Materials and Their Application," A. R. von Hippel, ed. MIT Press, 1954, p. 179.
41. Morey, G. W. "Properties of Glass." Reinhold Press, 1954, pp. 523-541.
42. Vermeer, J. Physica. 20 (1954) 313; ibid. 22 (1956) (a) 1247, (b) 1257, (c) 1269.
43. von Hippel, A. and R. J. Maurer. Phys. Rev. 59 (1941) 820.
44. Kuchin, V. D. Sov. Phys. Solid State. 1 (1959) 406.
45. Austen, E. W. and S. Whitehead. Proc. Roy. Soc. A, 176 (1940) 33.

## B. HETEROGENEOUS SEMICONDUCTING GLASSES (H. F. Schaake)

### Introduction

The fact that many glasses consist of several phases in metastable equilibrium has been recognized for many years. The separation of an initially homogeneous glass into two or more phases occurs by one of three mechanisms: (1) nucleation and growth of one or more glassy phases from the initially homogeneous phase; (2) spinodal decomposition of the initial phase into two new phases; and (3) nucleation and growth of one or more crystalline phases. Each of these processes gives rise to a characteristic microstructure.

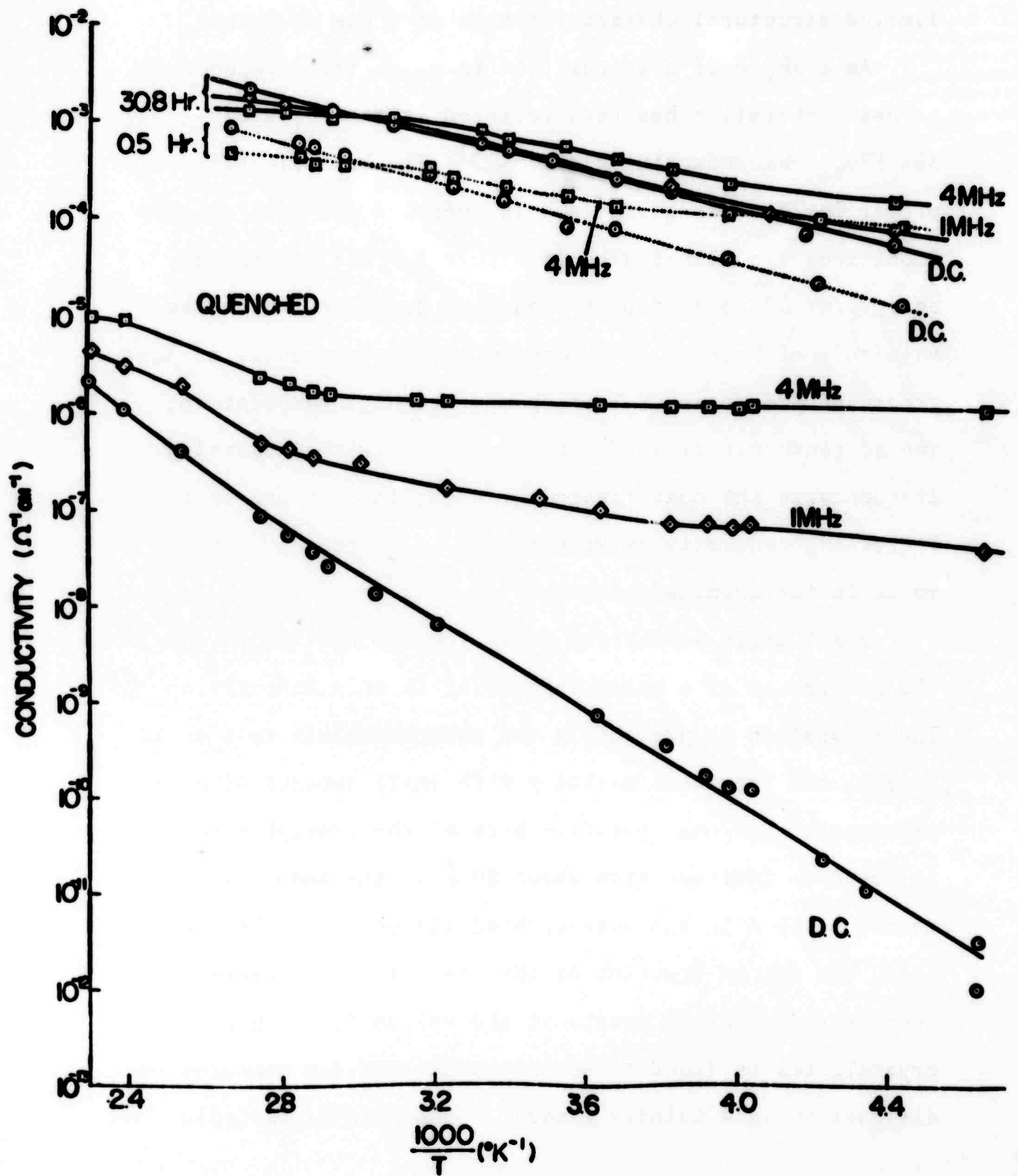
That the existence of such heterogeneities affects the electrical properties of a glass has been demonstrated for dielectric glasses,<sup>(1)</sup> and has been suggested for semiconducting glasses.<sup>(2)</sup> It appears, however, that no systematic study of the effects of heterogeneities on the conductivity of a semiconducting glass has been made. This

situation reflects the early stage of development of the theory of homogeneous amorphous semiconductors, and the limited structural characterization of these materials.

An example of a composition in which the existence of a phase separation has been verified is the 70%  $V_2O_5$  - 30%  $KPO_4$  semiconducting glass.<sup>(3,4)</sup> The bulk electrical properties of this glass in both quenched and heat treated conditions are illustrated in Figure 1. The activation energy for DC conduction is found to decrease, while the magnitude of both AC and DC conductivity increases, as heat treatment progresses. Furthermore, at high temperature, the AC conductivity is found to decrease with increasing frequency in the heat treated glasses, in contrast to the increasing conductivity with increasing frequency that is found in the quenched glasses.

Small angle scattering x-ray studies have confirmed the occurrence of a phase separation in this composition.<sup>(5)</sup> The separation is present in the quenched glass to a small extent, and increases markedly with small amounts of heat treatment. The mean particle size of the precipitated phase is found to increase from about 80 Å in the quenched glass to about 130 Å in the heat-treated glasses. At the same time, the volume fraction of the precipitate increases, but even after prolonged treatment the volume fraction of crystallites is found to be only about 10% (as measured by diffraction in a Guinier camera). Electron microscopic

Fig. 1 Total conductivity in annealed and heat treated glasses with composition 70%  $V_2O_5$  - 30%  $KPO_3$ .



examination of glasses in this system have also confirmed the occurrence of a phase separation with heat treatment. (6)

The question which these microstructural studies have raised is to what extent can the observed microstructural changes affect the AC and DC conductivity of the bulk sample. It is the purpose of this paper to review the effect of a heterogeneous microstructure on the AC and DC conductivity<sup>of semiconducting materials</sup>, and to apply these results on data obtained on the 30%  $\text{KPO}_{1/4}$  - 70%  $\text{V}_{2/5}\text{O}_5$  glasses.

#### Heterogeneous Models

The general problem of the electrical behavior of a composite in which random nucleation and growth leads to intersection of the new phase has not yet been treated. The mixture formulae which are available are based on specific geometric models, none of which are applicable over the entire range of volume fractions of the component phases for a phase separated glass. (7) A semiquantitative understanding of the electrical properties of a heterogeneous semiconductor can be obtained, however, by using an idealized model. For simplicity, we shall consider the precipitated particles to be non-intersecting uniform spheres, uniformly distributed in the matrix phase.

For small volume fractions of dispersed particles, the assumption that there are no interactions between particles

is applicable. The conductivity of such a composite is given by: (8)

$$\sigma_v = \sigma_1 \frac{\sigma_1(2-2v_2) + \sigma_2(1+2v_2)}{\sigma_1(2+v_2) + \sigma_2(1+v_2)} \quad (1)$$

where  $\sigma_1$  is the conductivity of the matrix phase,  
 $\sigma_2$  is the conductivity of the isolated phase, and  
 $v_2$  is the volume fraction of the isolated phase.

Assuming that the conductivities of both phases can be characterized by an activation energy, the apparent activation energy of the composite may be calculated from the relation:

$$Q^* = \frac{d \ln \sigma}{d\beta} \quad \beta = \frac{1}{kT} \quad (2)$$

The results are:

$$Q^* = \frac{Q_1(1-v_2)[2(2+v_2) + 4\alpha(1-v_2) + \alpha^2(1+2v_2)] + 9\alpha v_2}{2(2-v_2-v_2^2) + \alpha(4+v_2+4v_2^2) + \alpha^2(1+v_2-2v_2^2)} \quad (3)$$

with  $\alpha = \sigma_2/\sigma_1$

Three distinct regions can be delineated in Eq. (3):

$$\alpha \ll 1 \quad Q^* \approx Q_1 \quad (4a)$$

$$\alpha \approx 1 \quad Q^* \approx v_2 Q_2 + (1-v_2) Q_1 \quad (4b)$$

$$\alpha \gg 1 \quad Q^* \approx Q_1 \quad (4c)$$

The value of  $\alpha$  at which Eq. (4a) and Eq. (4c) become good approximations to  $Q^*$  is dependent on the volume fraction,  $v_2$

For large volume fractions of the isolated phase, the interactions between the particles cannot be ignored. Hanai has derived an equation for the conductivity valid in this limit for our model:<sup>(9)</sup>

$$\frac{\sigma - \sigma_2}{\sigma_1 - \sigma_2} \left( \frac{\sigma_1}{\sigma} \right)^{1/3} = 1 - v_2 \quad (5)$$

The activation energy can again be calculated using Eq. (2):

$$Q_a = \frac{(1-v_2) [2\sigma_1^{2/3} Q_1 + \sigma_1^{-1/3} \sigma_2 (Q_1 - 3Q_2)] + 3\sigma_1^{-1/3} \sigma_2 Q_2}{2\sigma_1^{2/3} + \sigma_1^{-1/3} \sigma_2} \quad (6)$$

While this equation is slightly more complex than Eq. (3), it reduces to Eq. (4) in the same limits. These results are to be expected. When  $\alpha \ll 1$ , the isolated phase is an excellent conductor, and the conductivity is limited by and hence determined by the matrix phase. Finally, when  $\alpha \sim 1$ , both phases conduct equally well, and the electric field is uniform throughout the composite, resulting in the simple volume fraction dependence of the activation energy.

In considering the AC properties of the DC path conductivity, it is desirable to introduce a model in which the isolated particles are coated with a thin barrier phase, as is shown in Figure 2. Discussion as to the nature of this barrier will be deferred until later. The sole effect on the DC conductivity is to change the conductivity of the isolated phase to:



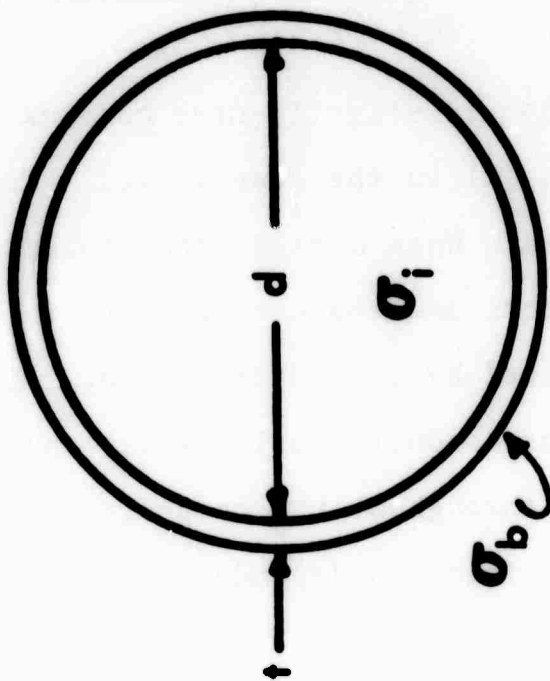


Fig. 2 Particle-barrier model.

$$\sigma_2 = \frac{\sigma_i \sigma_b}{\sigma_b + \frac{2t}{d} \sigma_i} \quad (7)$$

with the quantities defined in Figure 2.

The effect of an AC field on the conductivity of a composite can in principle be computed if, in addition to the real conductivities of the two phases, the frequency behavior of the dielectric constant is known. The resulting equations, however, are extremely complicated, even for the simplest model. The reason for the complication is apparent by considering the distribution of the electric field in the composite. If  $\alpha \gg 1$ , then the electric field is confined almost entirely to the matrix phase. Hence a relaxation process in the matrix will contribute to the AC conductivity much more greatly than will the identical process in the isolated phase. Furthermore, the changing conductivity with frequency will result in a change in the distribution of the field in the composite, leading to complex frequency dependent interactions between the two phases. In discussing the effects of frequency dependent dielectric constants, we shall therefore generally confine our attention to the behavior when the electric field is uniform throughout the composite, i.e., when  $\alpha = 1$ . Similarly, when discussing the effects of a non-uniform electric AC field in the composite, we shall generally treat the dielectric constant as being frequency independent.

### Mechanisms and Conductivity in Homogeneous Glasses

Before proceeding further with our discussion of heterogeneous materials, it is necessary to review the conduction mechanisms which have been proposed in the homogeneous amorphous materials which comprise the various phases.

A more detailed review of the conduction mechanisms in homogeneous semi-conducting glasses than we shall present here may be found in the article by Davis<sup>(10)</sup> in this volume, in several papers by Mott,<sup>(11,12)</sup> and in various papers of the SEAS symposium.<sup>(13)</sup>

Three distinct mechanisms have been recognized as important in amorphous materials (Figure 3). They are:

1. Essentially normal band conduction for carriers having energies above some critical value,  $E_c$ .

2. A diffusion mechanism, in which the mobility of a carrier having an energy below  $E_c$  but above a lower energy  $E_b$  is considerably reduced due to the electronic wavefunction being highly modulated by the disorder in the lattice, which results in regions in the diffusion path where the probability of finding the carrier is extremely small. The behavior of the carriers in the diffusion region is still band-like, in that it is a non-thermally activated process. There may be a substantial interaction between the electron in these states and the lattice displacement

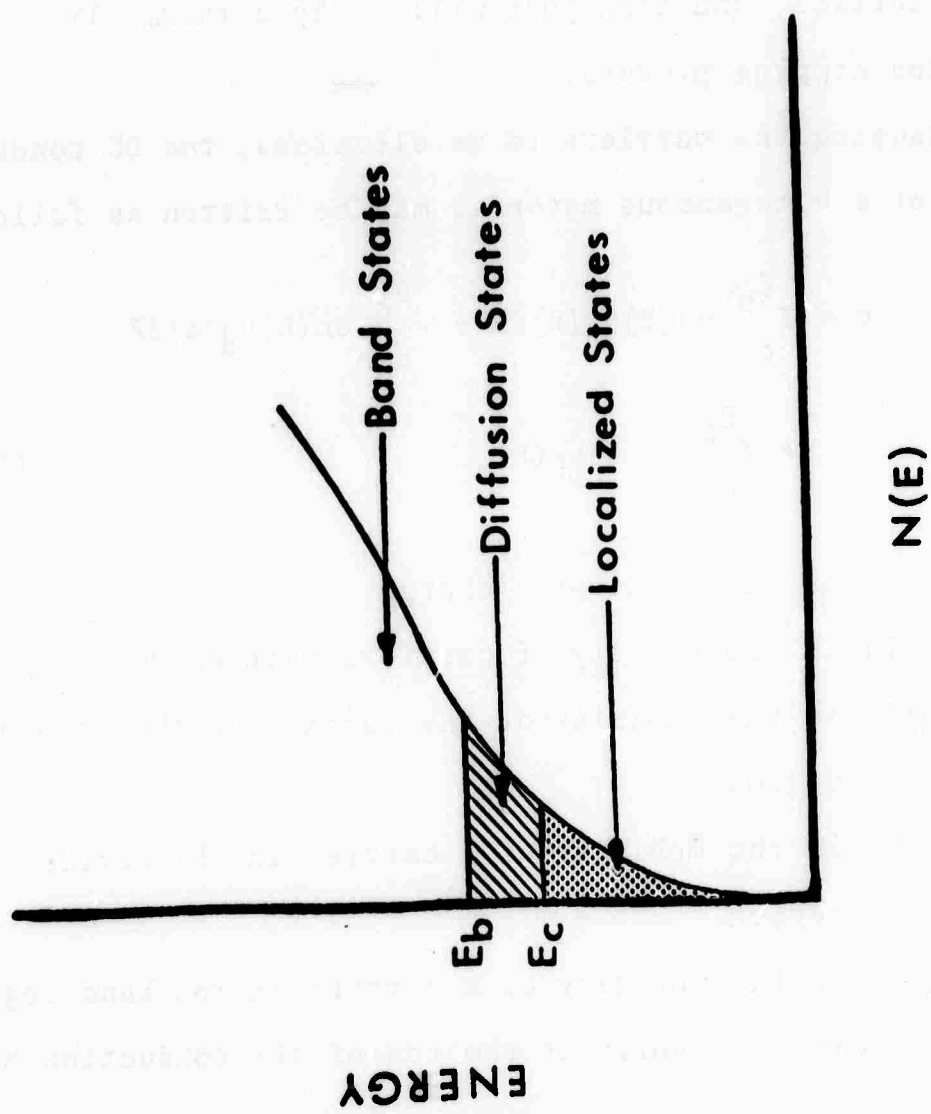


Fig. 3 Conductivity mechanisms in amorphous semiconductors. The density of states,  $N(E)$ , is plotted against the energy,  $E$ . Symbols are defined in the text.

which is polaronic in nature. The importance of the interaction will depend on the various material parameters involved. For a further consideration, see Reference 3, in which this diffusion region is referred to as a polaronic band. We may conclude, however, that the energies  $E_b$  and  $E_c$  are temperature dependent, increasing with increasing temperature.

3. Carriers having energies below  $E_b$  will be localized in the lattice, and transport will be by a thermally-activated hopping process.

Assuming the carriers to be electrons, the DC conductivity of a homogeneous material may be written as follows:

$$\sigma = \int_0^{E_b} e n(E) \mu_h(E) dE + \int_{E_b}^{E_c} e n(E) \mu_d(E) dE + \int_{E_c}^{E_B} e n(E) \mu_b(E) dE \quad (8)$$

where  $e$  is the electronic charge

$n(E)$  is the density of carriers with energy  $E$

$\mu_h(E)$  is the mobility of the carrier in the hopping region

$\mu_d(E)$  is the mobility of a carrier in the diffusion region

$\mu_b(E)$  is the mobility of a carrier in the band region

and  $E_B$  is the energy at the top of the conduction band.

When an AC field is applied to a homogeneous amorphous semiconductor containing partially filled localized states, localized carriers which are essentially isolated from the DC path can jump to nearby localized states of nearly the same energy, giving rise to a relaxation loss peak. The real part of this AC conductivity, which is additive to the DC conductivity will be given by: <sup>(10,14)</sup>

$$\text{Re } \sigma_{AC}(\omega) = \sum_t C(\tau) \frac{\omega^2 \tau^2}{1 + \omega^2 \tau^2} \quad (9)$$

where  $\tau$  is the relaxation time

$C(\tau)$  is a proportionality factor.

The complex part of the conductivity is related through a Kramers-Kronig relation.

The relaxation time will be given by: <sup>(3)</sup>

$$\tau = \frac{C}{\Delta E} \tanh \frac{\Delta E}{2kT} \quad \frac{h\omega_0}{k} \gg T \quad (10)$$

or, at sufficiently high temperatures:

$$\tau = C \exp\left[-\left(E_A + \frac{\Delta E}{2} + \frac{\Delta E^2}{16E_A}\right)/kT\right] \quad \frac{h\omega_0}{k} \ll T; \quad (11)$$

$$\frac{E_A}{h\omega_0} \coth \frac{h\omega_0}{2kT} \gg 1$$

where  $E_A$  is the activation energy

$\Delta E$  is the difference in energy between initial and final state

and  $\omega_0$  is the optical phonon frequency.

### Heterogeneous Mechanisms

The presence of heterogeneities in the semiconducting glass gives rise to the possibility of several additional conduction mechanisms, which we shall now discuss.

The classic mechanism in a heterogeneous medium is the interfacial polarization or Maxwell-Wagner loss mechanism, which arises when the conductivities or dielectric constants of the two phases differ.<sup>(8)</sup> When a step field is applied to such a heterogeneous medium, the electric field distribution in the various phases immediately after the application of the field (which is determined by the dielectric constants), will differ from the field distribution at infinite times (which is determined by the conductivities). The transition from the  $t = 0^+$  regime to the  $t \rightarrow \infty$  regime is a relaxation process dependent on the geometry of the heterogeneous medium, as well as the electrical constants.

The effect of the inhomogeneities on an AC field may be calculated for the low concentration model of Section II by replacing the real conductivity in Eq. (1) with the complex admittance:

$$A_i = \sigma_i + i\omega\epsilon_i \quad (12)$$

The results for the real (total) conductivity when the dielectric constants are frequency independent are:

$$\sigma = \sigma' + \frac{(\epsilon_s - \epsilon_\infty) \omega^2 \tau}{1 + \omega^2 \tau^2} \quad (13)$$

where:

$$\tau = \frac{(2+v_2)\epsilon_1 + (1-v_2)\epsilon_2}{(2+v_2)\sigma_1 + (1-v_2)\sigma_2} \quad (14)$$

$$\epsilon_s = \epsilon_1 \left( \frac{\sigma_1'}{\sigma_1} \right) + 3v_2\sigma_1 \left[ \frac{(2\sigma_1 + \sigma_2)(\epsilon_2 - \epsilon_1) - (2\epsilon_1 + \epsilon_2)(\sigma_2 - \sigma_1)}{[(2+v_2)\sigma_1 + (1-v_2)\sigma_2]^2} \right]$$

$\epsilon_\omega$  is given by Eq. (1) with  $\epsilon_i$  substituted for  $\sigma_i$ , and  $\sigma'$  is given by Eq. (1).

In order for the losses to be observable, there need only be an observable difference between  $\epsilon_s$  and  $\epsilon_\omega$ . It will be noticed that Eq. (13) is the equation for a simple Debye relaxation process. This is no longer the case if we consider the high concentration model of Section II, or one in which the isolated phase is no longer spherical. The general characteristics of the loss peak remain the same, however, with other powers of  $\omega$ , in addition to  $\omega^2$  appearing in the equation for  $\sigma(\omega)$ .

An interesting model is that in which each of the isolated particles is coated with a barrier phase. Treating this model in the low concentration limit, and assuming  $\sigma_b = i\omega c$ ;  $\sigma_i \gg \sigma_1$ , real (see Figure 2), we find that Eq. (13) is applicable and that

$$\tau = \frac{c}{\sigma_1} (1-v_2) \quad (15)$$

We shall refer to these results later.

In addition to Maxwell-Wagner losses, several other AC phenomena may be present in heterogeneous semiconductors.



These additional mechanisms depend on the existence of Schottky barriers or other types of barriers, such as a compositional change at the interface of the two phases. The Schottky barriers will arise when the Fermi levels in the different phases in isolation are different, due to differences in composition, structure, or both. In order to establish a constant Fermi level when the two are in contact, charge may be transferred from the phase having the higher Fermi level to that having the lower (Figure 4a). It is these barriers which give rise to the barrier phase of Section II.

With the presence of these barriers, the following additional mechanisms may arise.

1. Barrier Tunneling. If the charge transfer is sufficient to completely displace the conduction states which are contributing the greatest to the conduction or, if the isolated phase is separated from the matrix phase by an insulating barrier, then barrier tunneling will result (Figure 4). If conduction is by carrier hopping, then the hopping time through the barrier will be given by:

$$\tau' = \tau \exp(-2\alpha d) \quad (16)$$

where  $\alpha = \sqrt{\frac{2mW}{\hbar^2}}$

W is the barrier height

d is the barrier width

and  $\tau$  is given by Eq. (10) or (11).

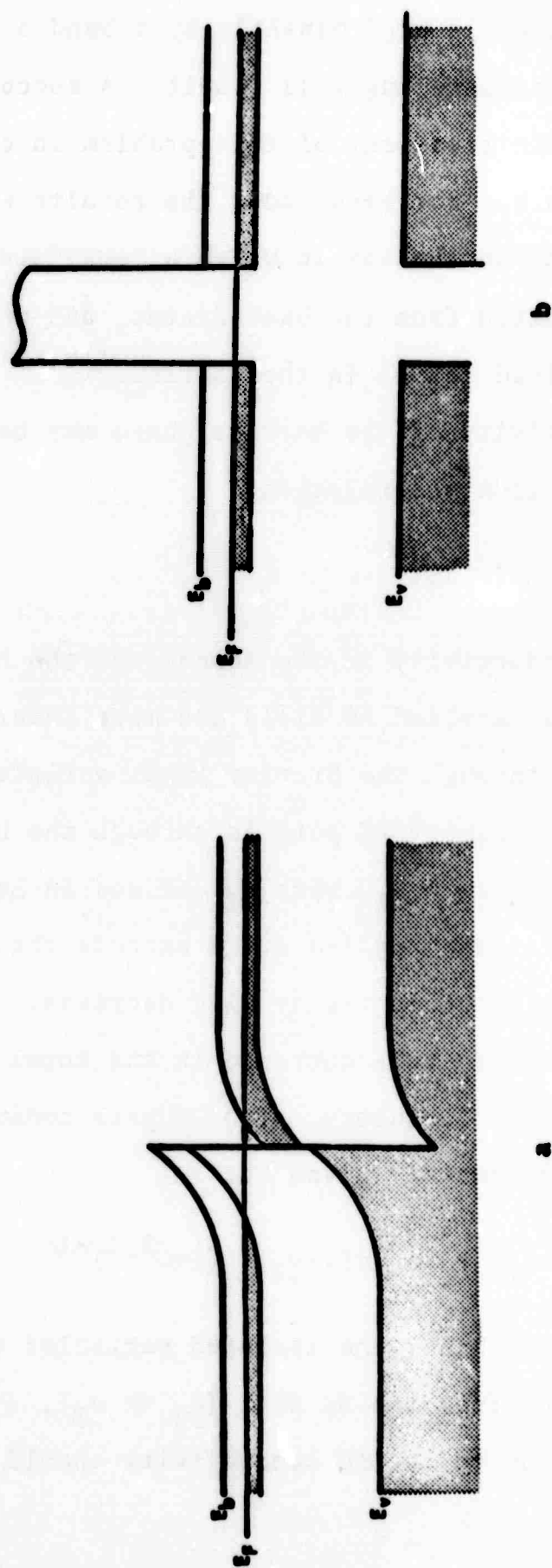


Fig. 4 Possible configurations of barriers in heterogeneous amorphous semiconductors.  
(a) Schottky barrier (b) Insulation barrier.  $E_F$  is the Fermi level.

If the conduction is predominantly by a band diffusion mechanism, then band tunneling will result. A successful quantitative analytic treatment of this problem in crystalline semiconductors has not been made; the results which are available depend on the way in which a localized wavefunction is constructed from the band states, and on the existence of localized states in the barrier. (16,17)-

The DC conductivity of the barrier phase may be approximately calculated from the relation:

$$\sigma_b = \sigma_0 \exp(-2ad) \quad (17)$$

where  $\sigma_0$  is the conductivity in the absence of the barrier. The results under an applied AC field are more interesting. Since a transition through the barrier takes a finite amount of time, and if the primary DC path is through the barrier (which is the case if  $\sigma_2 > \sigma_1$ , with  $\sigma_2$  defined in Eq. (7)), then as the period of the applied field exceeds the transition time, the DC path conductivity will decrease. Such a circumstance may lead to a decrease in the total conductivity with increasing frequency. The DC path conductivity should then be approximately given by:

$$\sigma = \sigma_1(1-v_2) + [\sigma' - \sigma(1-v_2)] (1+\omega^2\tau^2)^{-1/2} \quad (18)$$

If, on the other hand, the isolated particles are essentially isolated from the DC path ( $\sigma_2 \ll \sigma_1$ ), then an additive contribution to the AC conductivity should be

present, in accordance with Eqs. (9) and (16), due to the transition of carriers through the barrier. This additive contribution will be in addition to the Maxwell-Wagner effect.

2. Thermal Activation Over the Barrier. If the charge transfer does not completely displace the conduction states which are contributing the greatest to the conduction (Figure 4a), then thermally activated hopping over the barrier may result. The conductivity through the barrier will then be given by:

$$\sigma = ne\mu_B \exp(-W/kT) \quad (19)$$

where the mobility  $\mu_B$  is essentially unchanged from that of the constituent material. Since the mobility is essentially unchanged, such a process will make no additional contribution to the AC conductivity -- it will merely affect the DC conductivity.

#### Application to Heterogeneous Glasses

As discussed in the introduction, glasses with the composition 30%  $KPO_3$  - 70%  $V_2O_5$  are found to be heterogeneous after a short heat treatment at 288°C. These glasses (which, according to thermopower measurements, are n-type semiconductors) are therefore potentially useful in applying the principles of the previous sections. Our task will be

complicated by the lack of electrical data on each of the constituent phases.

We shall begin by considering the AC conductivity, as this gives the most information as to the mechanism operative. The additive AC conductivity for a quenched and heat treated glass is presented in Figures 5, 6 and 7. To elucidate the conduction mechanisms, it is worthwhile to note that the AC conductivity above  $5 \times 10^6$  MHz is proportional to  $\omega^2$  in both the quenched and heat treated glasses, and that the activation energy for the AC conductivity is approximately 0.05 ev in the quenched glass at all frequencies, and in the heat treated glass at low frequencies. This is suggestive of the hopping of trapped carriers with  $\tau$  appreciably smaller than  $3 \times 10^{-8}$  sec., as Eq. (9) reduces to:

$$\sigma_{AC}(\omega) = \sum_{\tau} C(\tau) \omega^2 \tau \quad (20)$$

when the product  $\omega\tau \ll 1$ . The temperature dependence of Eq. (20) is contained in the product  $C(\tau)\tau$ . The temperature dependence in  $C(\tau)$  is due to the product of the Fermi factor  $f(E)$  and a distribution function  $g(E, \Delta E)$  which tells how many pairs of states at energy  $E$  have a difference in energy  $\Delta E$ , and a factor  $1/T$  which arises from the Einstein equation for the diffusion coefficient, while the temperature dependence of  $\tau$  is given by Eq. (10) or Eq. (11). The present data is insufficient to separate these temperature

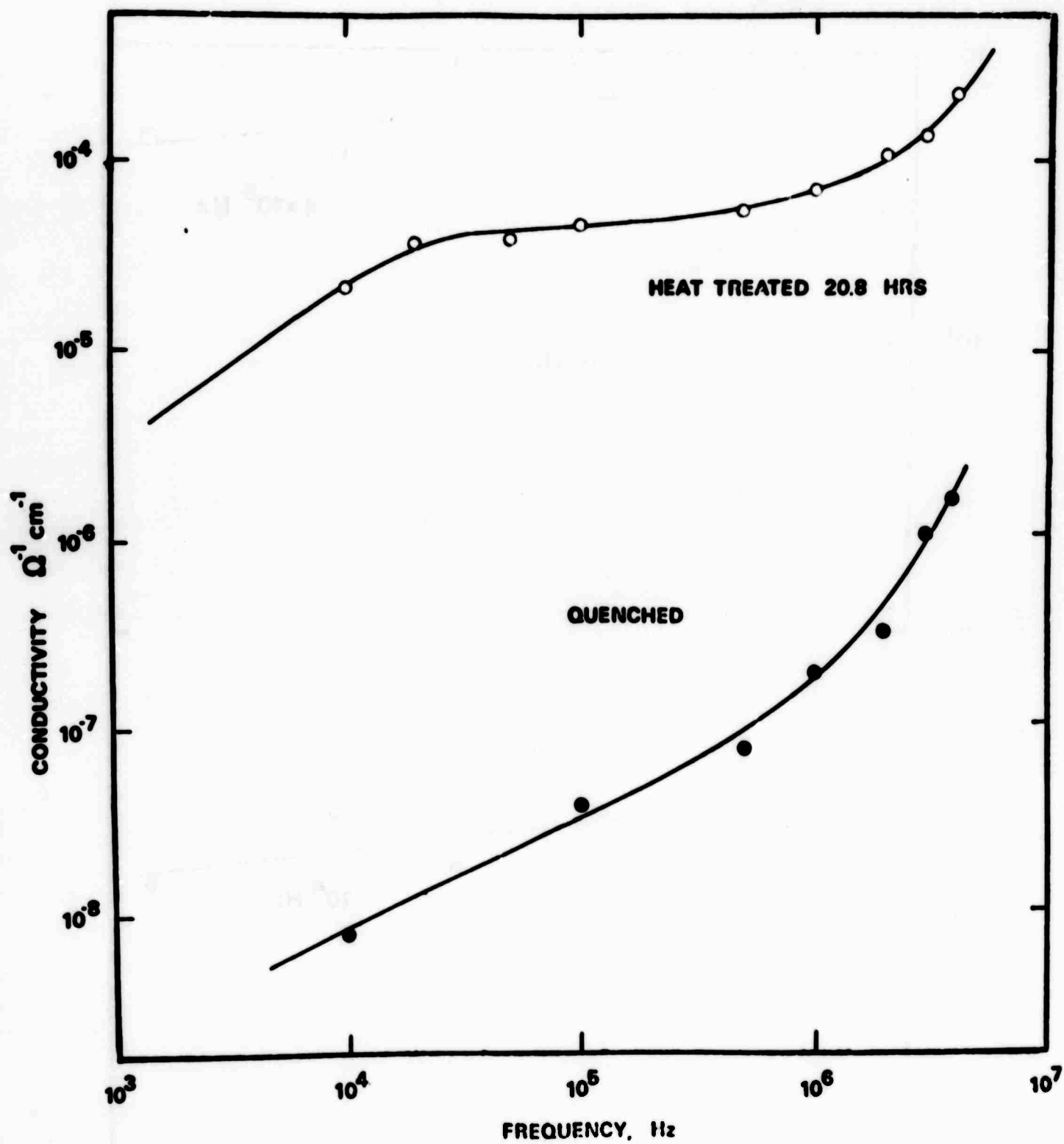


Fig. 5 AC conductivity in quenched and heat treated glasses (70%  $\text{V}_2\text{O}_5$  - 30%  $\text{KPO}_3$ ) at 300°K.

Fig. 6 Temperature dependence of AC conductivity in quenched glass.

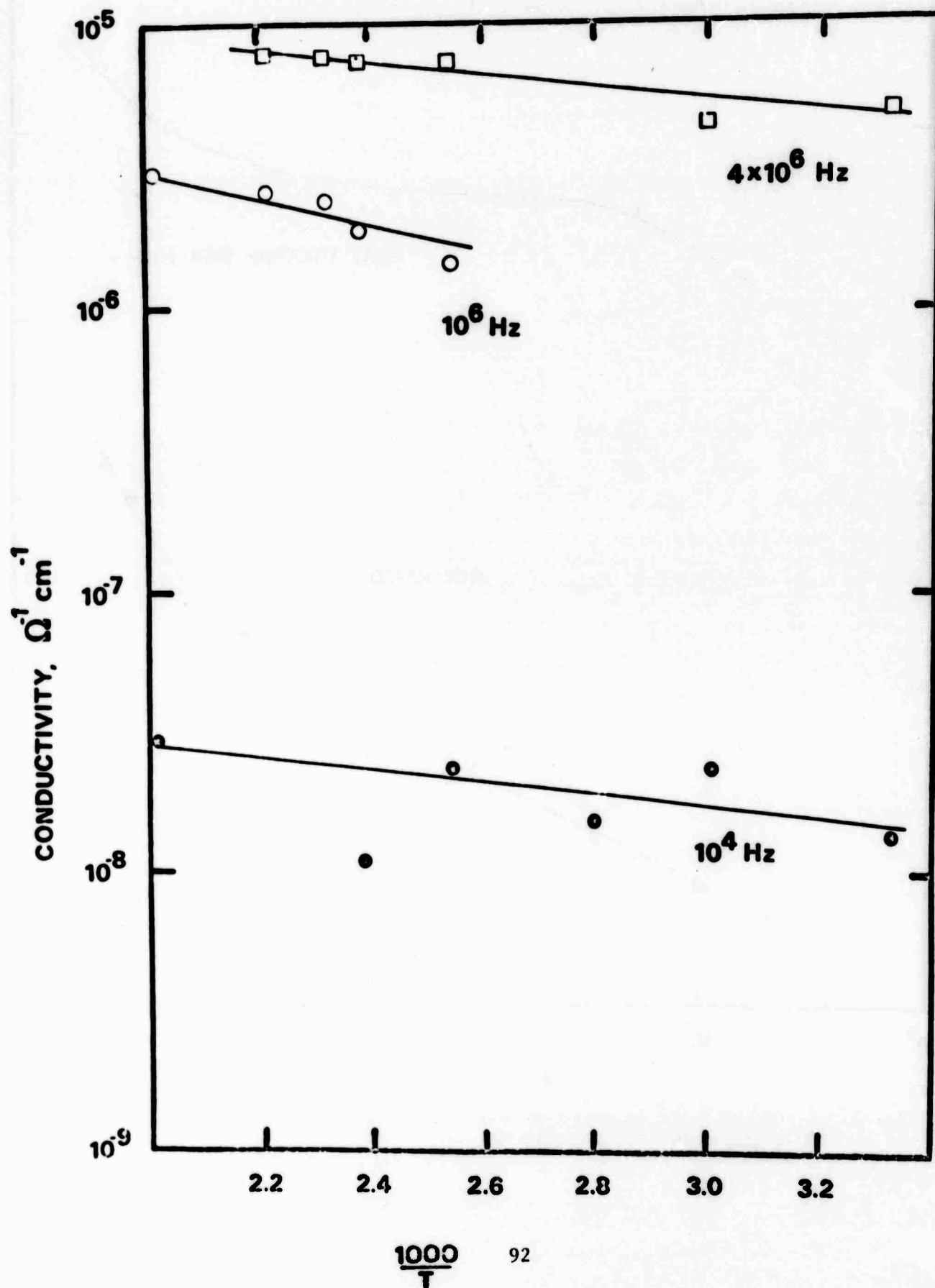
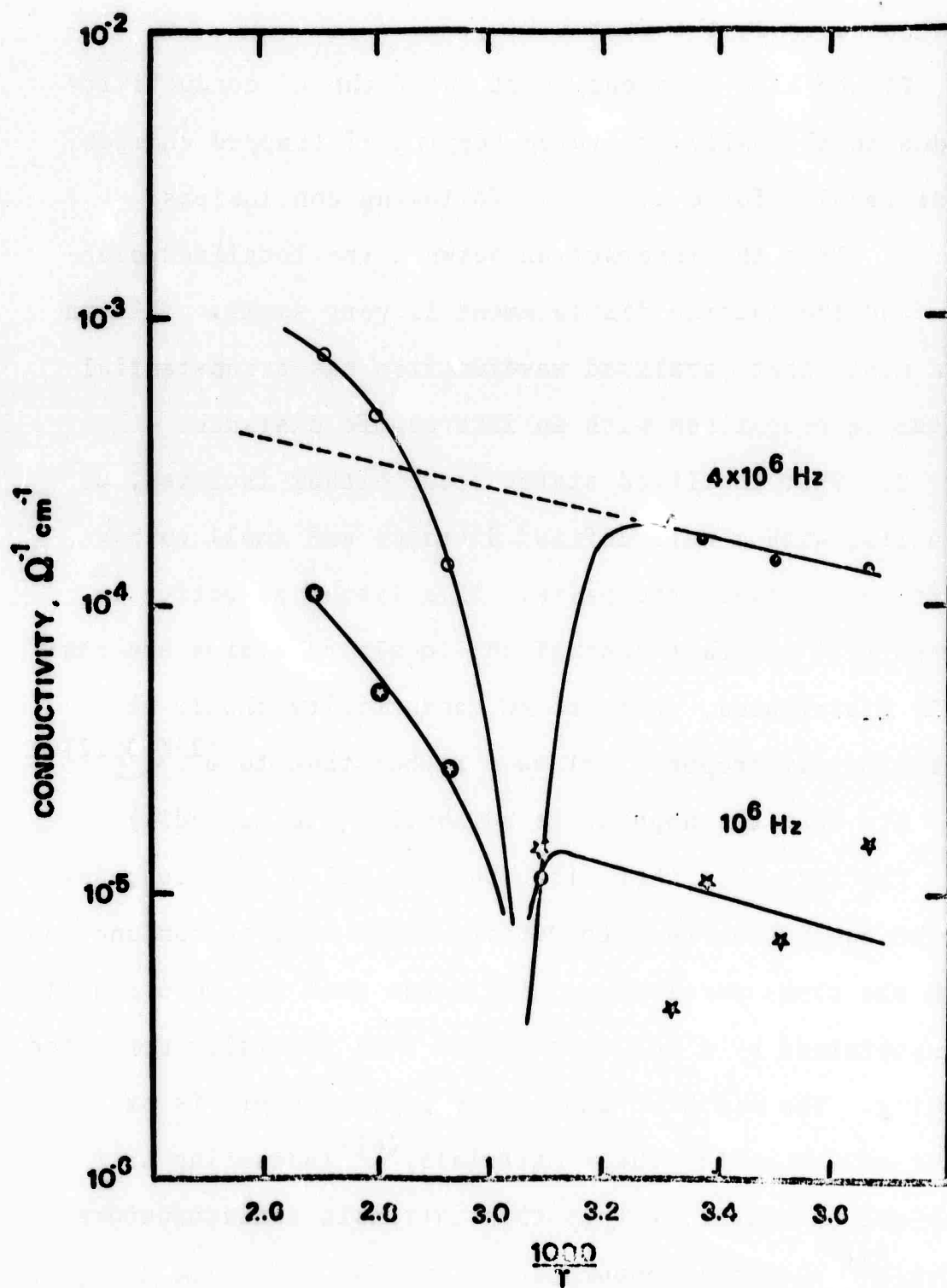


Fig. 7 Temperature dependence of AC conductivity in heat treated glass. Open symbols indicate negative quantities.





dependences. Owen, however, has measured the AC conductivity of similar glasses and has found  $\tau$  to be of the order of  $10^{-10}$  sec. and essentially independent of temperature.<sup>(18)</sup> It therefore appears that all of the temperature dependence is in the factor  $C(\tau)$ .

If the high frequency portion of the AC conductivity is due to thermally activated hopping of trapped charges, these results force us to the following conclusions:

1. That the interaction between the localized electron and the lattice displacement is very small. This in turn means that localized wavefunction has a substantial radius in comparison with an interatomic distance.

2. That localized states occur either isolated, or in pairs, with a well defined distance and small energy difference between the pairs. This latter situation is a result of the fact that if the localized states are randomly distributed, then the AC conductivity should be approximately proportional to  $\omega$  rather than to  $\omega^2$ .<sup>(10,12)</sup>

3. That the hopping is adiabatic (see Appendix).

The fact that there is a substantial activation energy for DC conduction (0.2 to 0.6 eV, Figure 8), in conjunction with the above conclusions, indicates that the DC conduction is determined by a mechanism other than thermally activated hopping. The width of the energy gap, however, is of the order of 2.5 eV for these materials,<sup>(6)</sup> indicating that they are extrinsic, rather than intrinsic semiconductors (with  $V^{4+}$  acting as donors).

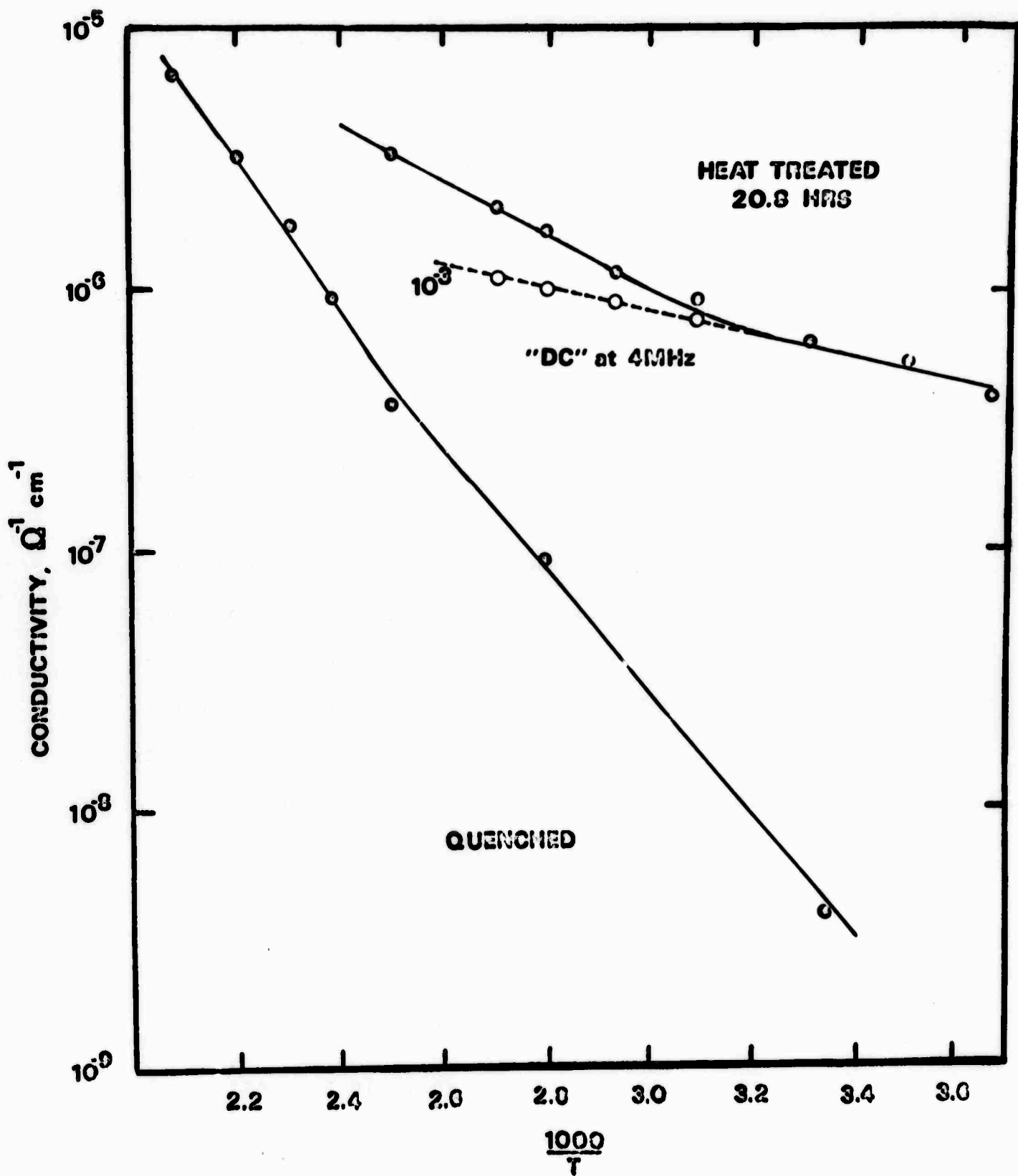


Fig. 8 Temperature dependence of DC conductivity in quenched and heat treated glass. The dashed line is explained in text.

We are therefore led to postulate two models for the conduction mechanisms in the glass:

1. (Figure 9a) That due to the disorder, a large number of localized states are split off from the conduction band, with a large concentration located in the vicinity of the impurity states,  $\sim 0.2$  ev below the conduction band, and with barriers of from 0 to 0.4 ev present, depending on the heat treatment. The high frequency AC conductivity is then due to impurity hopping, with the conditions previously discussed being true. The DC conduction is barrier-regulated by a band mechanism.

2. (Figure 9b) That the impurity states lie just underneath the conduction band, but that there are barriers raised in the conduction band which determine the DC activation energy. The DC conduction is therefore a barrier-regulated band mechanism, while the AC conductivity results from a migration of carriers at the bottom of the band (which are localized states when viewed over the entire glass) under the influence of the AC field. The height of the barriers must decrease with heat treatment.

Turning now to the low frequency AC conductivity, we see that in the quenched glass there is a region where the conductivity is proportional to  $\omega$ , while in the heat treated glass there appears to be a well defined relaxation process with  $\tau \approx 8 \times 10^{-6}$  sec. There are two explanations for the behavior in the quenched glass. (1) The hopping of

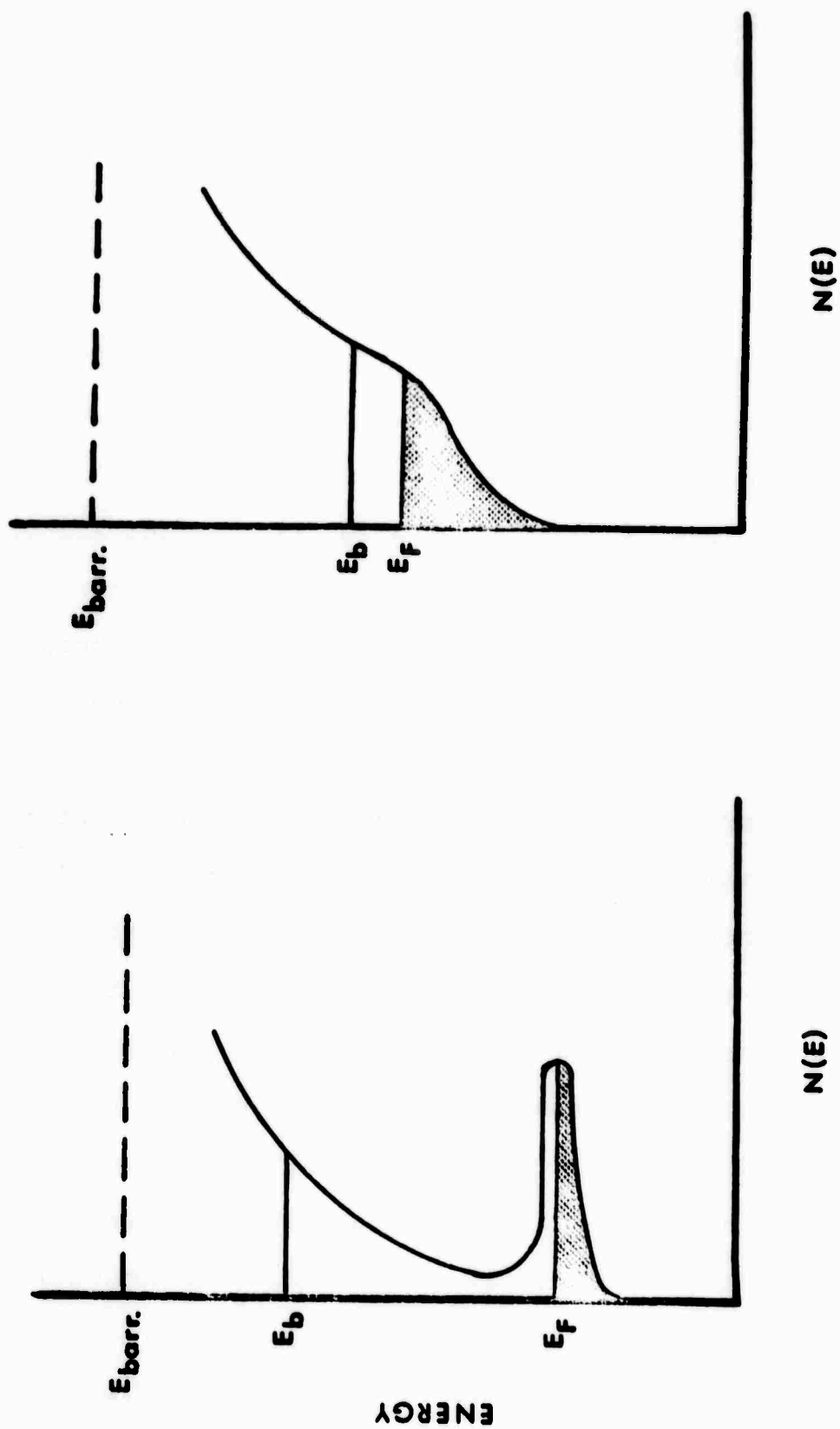


Fig 9 Possible electronic energy structures in 70%  $V_2O_5$  - 30%  $KPO_3$  glasses.  
 $E_F$  is the Fermi level.

localized carriers between randomly distributed centers. This would be in addition to the pair hopping previously discussed; a much smaller number of carriers would be participating in this process than in the pair hopping process. (2) Maxwell-Wagner losses due to a non-spherical second phase. There is some x-ray evidence that the isolated phase in the quenched glass is non-spherical. (5)

In the heat treated glass, however, only the Maxwell-Wagner loss mechanism explains the data. The relaxation time for this loss is found to be a function of temperature, with an activation energy of 0.2 ev (Figure 10). This is also the activation energy for DC conduction in the composite.

Using the low concentration model, and the assumptions that  $\alpha \gg 1$ , and that the dielectric constants of the two phases are temperature independent in the region of interest, the relaxation time should be proportional to  $\sigma_2^{-1}$ . In the low concentration model when the particles are coated with a capacitive barrier phase (Eq. (15)), the relaxation time is proportional to  $\sigma_1^{-1}$ . A physical consideration of this latter model in the limits of high concentration and with the barrier phase having a small real conductivity, indicates that the relaxation time should be proportional to the reciprocal of the composite conductivity, for the barrier forms a series RC circuit, with the resistance being determined essentially by the entire composite.

Turning now to the DC path conductivity in the heat treated glass, it will be noticed that at high temperatures and frequencies, the conductivity decreases with increasing frequencies of  $10^6$  and  $4 \times 10^6$  MHz (Figure 8). The conductivity of the composite at 4 MHz less the additive AC conductivity (which is evident at low temperatures and is assumed to be present also at high temperatures) is plotted in Figure 10. It will be noticed that this forms an extension of the low temperature DC conductivity. This data is consistent with a model in which the isolated phase is coated with a tunneling barrier, for which the transit time through the barrier is  $\sim 10^{-6}$  seconds. The activation energy of the matrix is 0.05 ev, while that of the isolated phase is of the order of 0.2 ev. At 330°K, the conductivity of the isolated phase (particle plus barrier) becomes equal to that of the matrix phase, marking the onset of the decreasing conductivity with frequency. With this interpretation, we would expect the total conductivity to level off at frequencies above 4.5 MHz, and then to again increase with frequency, due to the domination of the carrier hopping contribution to the total conductivity.

Attempts to elucidate the nature of the barriers are of questionable value, due to the limited structural and electrical data, and an incomplete knowledge of the electronic structure of the component phases. Schottky barriers may be justified on the basis of the difference in the

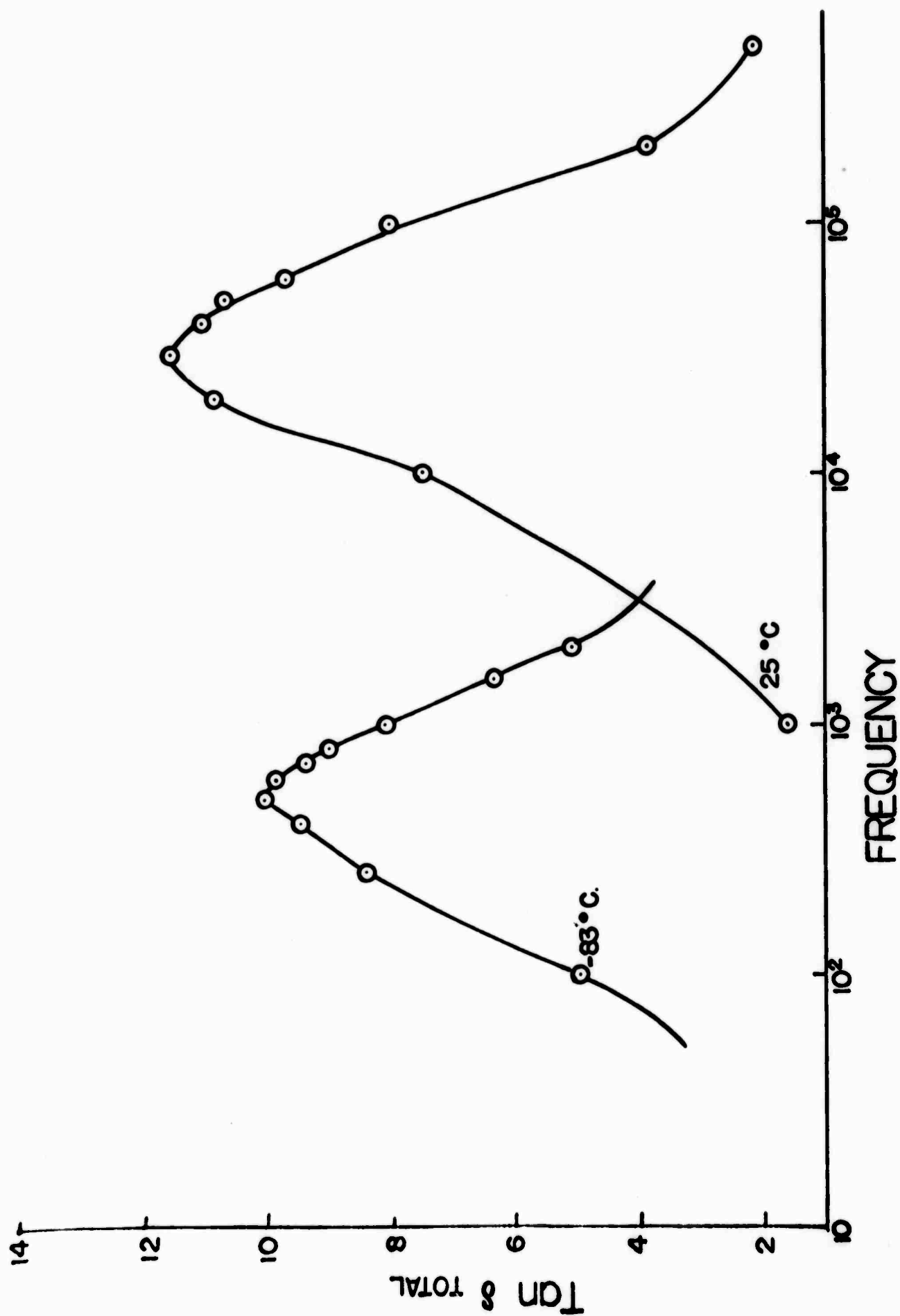


Fig. 10 Loss peaks in heat treated glass.

composition of the matrix and isolated phases. On the other hand, insulating barriers could exist as a result of a vanadium deficiency at the interphase boundary, which results from a minimization of the interfacial energy. Further structural and electrical studies will be required.

The discussion applied to the data of Figures 5, 6, 7, and 8 does not appear to apply to all data on heterogeneous glasses, however. For example, the decrease in AC conductivity with frequency illustrated for the glasses heat treated 0.5 hours and 30.8 hours in Figure 1 is not the same as that just discussed, in that the DC conduction process does not show a break in activation energy. An explanation for this difference may lie in differences between the microstructures of these glasses. A liquid-liquid separation and a liquid-crystal separation may be competing with each other. (6) In that these glasses were cast from different temperatures, their microstructures before heat treatment may be different, in which case the kinetics and microstructural development during heat treatment will be different. Such a possibility is of considerable interest in that the activation energies for DC conduction differ in the two quenched glasses (0.4 eV for that in Figure 1, 0.6 eV for that in Figure 8).



## Appendix

In the derivation of the transition times (Eqs. (10) and (11)), it was assumed that the value of the overlap integral,  $J$ , between the initial and final states:

$$J = \langle m | V | n \rangle$$

is sufficiently small, so that the transition takes place over several periods of the phonon frequency. This assumption leads to a dependence of the transition time for a one phonon process:

$$\tau \propto \frac{1}{J^2}$$

If, however,  $J$  is sufficiently large, the conditions for the approximations made in Ref. 3 are no longer valid. This problem (adiabatic hopping) has been investigated for the multiphonon process by Holstein, <sup>(18)</sup> who finds <sup>that</sup> the pre-exponential factor in Eq. (11) becomes approximately constant, independent of the overlap integral. Physically, this means that the time it takes the carrier to tunnel from one site to another is small in comparison to the time it takes for a phonon to be absorbed or emitted; hence the phonon coupling process becomes the rate determining mechanism. We expect the same analysis to be true for a one phonon process (Eq. (10)).

The existence of adiabatic hopping means that the transition time between sites having a separation greater than some critical value  $r_c$  will be dependent on the separation, while the transition time for hops between sites having a separation less than  $r_c$  will be approximately independent of the separation.

The AC conductivity will therefore consist of two components; one proportional to  $\omega$  due to non-adiabatic hopping, and one proportional to  $\omega^2$  due to adiabatic hopping. If  $r_c$  is sufficiently great, such that there are a large number of site pairs contributing to adiabatic hopping, then the  $\omega^2$  dependence will dominate at high frequency. This is the behavior found in the quenched glass (Figure 5).

### References

1. D. L. Kinser and L. L. Hench, J. Amer. Ceram. Soc., 51 (1968) 445-449.
2. J. D. Mackenzie, in: Modern Aspects of the Vitreous State, Vol. 3 (Butterworths, Washington, 1964) p. 126.
3. H. F. Schaake and L. L. Hench, Jrn. of Non-Crystalline Solids, p. 444 (1970).
4. L. L. Hench, Int'l Jrn. of Non-crystalline Solids, 1 (1970). Proceedings from the SEAS Symposium, New York, May 1969.
5. S. R. Bates and L. L. Hench, to be published.
6. G. W. Anderson, Structural Characterization and Optical Transmission Studies of Vandate Glasses, Ph.D. Thesis, University of Illinois, 1969.
7. L. K. H. van Beek, in Progress in Dielectrics, Vol. 7 (CRC Press, Cleveland, 1967) p. 69.
8. J. S. Dryden and R. J. Meakins, Proc. Phys. Soc. London, B70, 427 (1957).
9. T. Hanai, Bull. Inst. Chem. Res., Kyoto Univ., 39, 341 (1961).
10. E. A. Davis, "Electronic Processes of Amorphous Semiconductors," Physics of Electronic Phenomena.
11. N. F. Mott, Contemporary Physics, 10, 125 (1969).
12. N. F. Mott, Phil. Mag., 17, 1259 (1968).

13. Proceedings of the Symposium on Semiconducting Effects in Amorphous Solids, May, 1969, New York, published in Jrn. Non-crystalline Solids (1970).
14. M. Pollack and T. H. Geballe, Phys. Rev., 122 (1961) 1742.
15. C. B. Duke, Tunneling in Solids (Academic Press, New York, 1969), p. 49.
16. T. Hartman, J. Appl. Phys., 33, 3427 (1962).
17. A. E. Owen, Jrn. Non-crystalline Solids (1970).
18. T. Holstein, Annals Phys., 8, 343 (1959).

C. POWDER SAMPLE PREPARATION ERRORS IN X-RAY SPECTROCHEMICAL ANALYSIS  
(D. E. Clark and L. L. Hench)

Introduction

In recent years the use of x-ray spectrochemical analysis has become very popular in the fields of mining, glass, and ceramics for determining the relative composition of ores, raw materials, and finished products. In each of these cases analyses are made on particulate samples. Errors in x-ray spectrochemical analysis are due to fluctuations in equipment, mis-use of equipment, or problems in sample preparation. This paper is concerned primarily with the error resulting from sample preparation.

Neglecting the ever-present problem of obtaining a representative 10-20 gram sample from a 10 ton stockpile, sample preparations generally stands out as the most difficult and time-consuming step in the entire analytical process. The x-ray spectrochemical method may be applied to a sample in the liquid, solid, glassy or powdered state. Consequently, there are many methods of sample preparation. We are concerned herein with only the problems associated with the general method of pressing dry powders into small pellets and exposing them to radiation.

All matter absorbs x-rays to a greater or less extent depending on (1) the wavelength of the x-rays, and (2) the mass absorption coefficient,  $\mu/\rho$ , of the materials for that particular wavelength. For completely solid materials with no voids the absorption equation relates the transmitted intensity of the x-ray beam,  $I_t$ , to the initial intensity before striking

the sample ( $I_0$ ),

$$I_t = I_0 \exp(-(\mu/\rho) \rho t)$$

where " $\mu$ " is the linear absorption coefficient, " $\rho$ " is the density of the material, " $t$ " is the sample thickness, and " $\mu/\rho$ " is the mass absorption coefficient.<sup>(1)</sup> For the heavier elements  $\mu/\rho$  is such that the incoming x-rays penetrate only a few angstroms. However, in the lighter elements, such as magnesium,  $\mu/\rho$  is small and thus x-rays can penetrate to a considerable depth in the sample. As much as 80% porosity can occur in pressed powder samples at low forming pressures and, consequently, the mass absorption coefficient  $(\mu/\rho)_0$  for the pure compound is changed to  $(\mu/\rho)_1$  for the compound plus  $(\mu/\rho)_2$  for pores between the particles. Of course, the coefficient of absorption for pores is much less than for a solid material. Thus, one would expect the x-rays to penetrate a pressed powder sample to a greater depth than the pure crystalline material with no porosity. The accuracy of x-ray spectrochemical analyses is thus potentially highly susceptible to variations in density and thickness of pressed samples. This potential source of analytical error is examined in this paper.

The objectives of the research are: (1) To determine the characteristic x-ray intensity obtained from pressed powders as a function of forming pressure and sample density. (2) To determine the x-ray intensity of pressed powder samples as a function of sample thickness.

### Experimental Procedure

Four chemical compounds,  $\text{MgCO}_3$ ,  $\text{TiO}_2$ ,  $\text{Cr}_2\text{O}_3$ ,  $\text{ThO}_2$ , were studied. All four compounds were reagent grade and were 200 mesh or finer. Samples were formed by pressing loose powders in a single action cylindrical Carver die with a pressing surface area of one square inch. Samples were prepared with forming pressures from 2,000 psi to 24,000 psi at increments of 2,000 psi. A second series of low density samples was prepared by compacting loose powders directly in the x-ray sample holder. The sample holder was filled with powder and exposed to x-radiation. The powder was pressed at 50 psi by hand and irradiated again. This process was performed in increments of 50 psi up to ~200 psi. A sheet of 1/4 mil mylar was placed over the end of the sample holder to prevent the loose powders from falling into the x-ray unit. The same sheet of mylar was used for the pressed pellets as well.

A Norelco Vacuum X-ray Spectrometer was used for the experiments. The samples were exposed to Tungsten  $\text{L}\alpha$  radiation and the time necessary to count a fixed number of characteristic x-rays was recorded. The fixed count divided by the time necessary to produce the count is reported as the measured intensity. The counting times, sample thicknesses and experimental conditions employed are summarized in Table I.

The intensities of the characteristic  $\text{MgCO}_3$  and  $\text{TiO}_2$  radiation were measured with a modified flow-gas proportional counter. 90% argon-10% methane gas flowed through the counter at the rate of 0.5 cfh. This type of detector is very effective

TABLE I

<u>Compound</u>	<u>Crystal</u>	<u>Gas Flow</u>	<u>Vacuum</u>	<u>Fixed Count</u>	<u>Sample Thickness</u>	<u>MA</u>	<u>KV</u>	<u>2θ</u>
MgCO <sub>3</sub>	ADP	0.5 cfh	100 microns	4000	0.40-2.81 cm*	40	50	106.74
TiO <sub>2</sub>	EDDT	0.5 cfh	---	8000	0.39-2.81	20	50	36.40
Cr <sub>2</sub> O <sub>3</sub>	EDDT	scintillation	---	64000	0.40-2.81	20	50	32.27
ThO <sub>2</sub>	LiF	scintillation	---	64000	0.51-2.81	20	50	27.27

\*2.81 corresponds to the height of the loose powders in the x-ray sample holder.



for elements with low atomic number ( $Z < 20$ ). The characteristic intensities of  $\text{Cr}_2\text{O}_3$  and  $\text{ThO}_2$  were measured with a scintillation detector.

### Experimental Results

The increase in bulk density of the samples versus forming pressure is shown in Figure 1. The density change is represented as the measured fraction of theoretical (or single crystal) density of the compound. Initially, the loose powders contain about 60-90% porosity. Cold pressing at 24,000 psi produces samples with a range of 40-60% porosity. Figure 1 shows that the powders have an initial large increase in density with increasing pressure. The higher density compounds appear to reach their maximum density at lower forming pressures than do compounds containing lighter elements.

Magnesium carbonate has the most interesting pressing characteristics of the materials studied. Its pressure-density curve has the smallest initial slope and reaches its maximum at much higher pressures than the other materials. Pressing above 10,000 psi causes an interesting phenomenon to occur in thick samples of magnesium carbonate. A cone shaped portion of the pellet can actually be separated from the rest of the sample. This is caused by shearing due to internal density gradients, as discussed by Train.<sup>(2)</sup>

The x-ray intensity-density curves for all four compounds are similar as shown in Figure 2. There are three distinct regions that occur in the curves. Region I corresponds to a

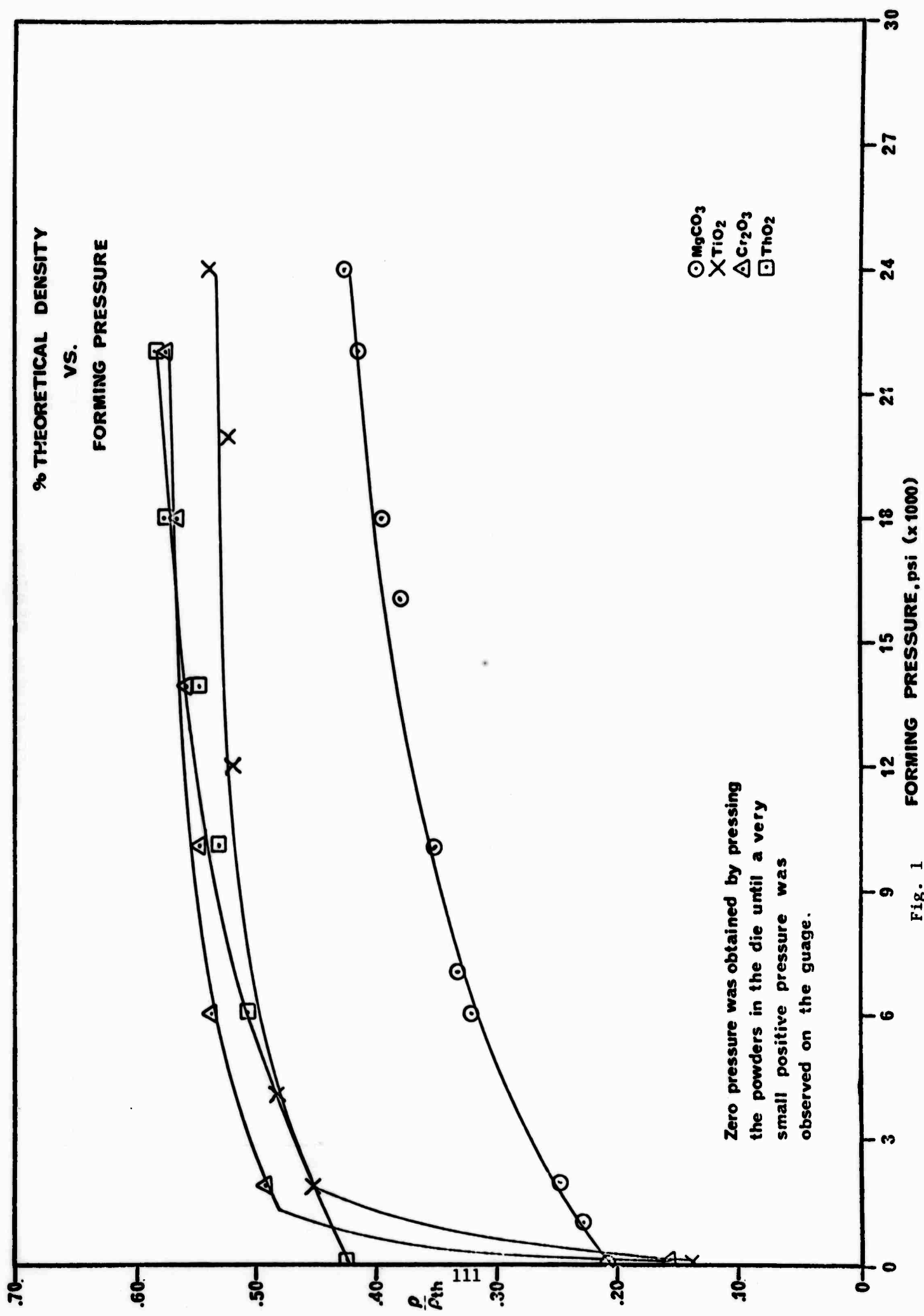


Fig. 1

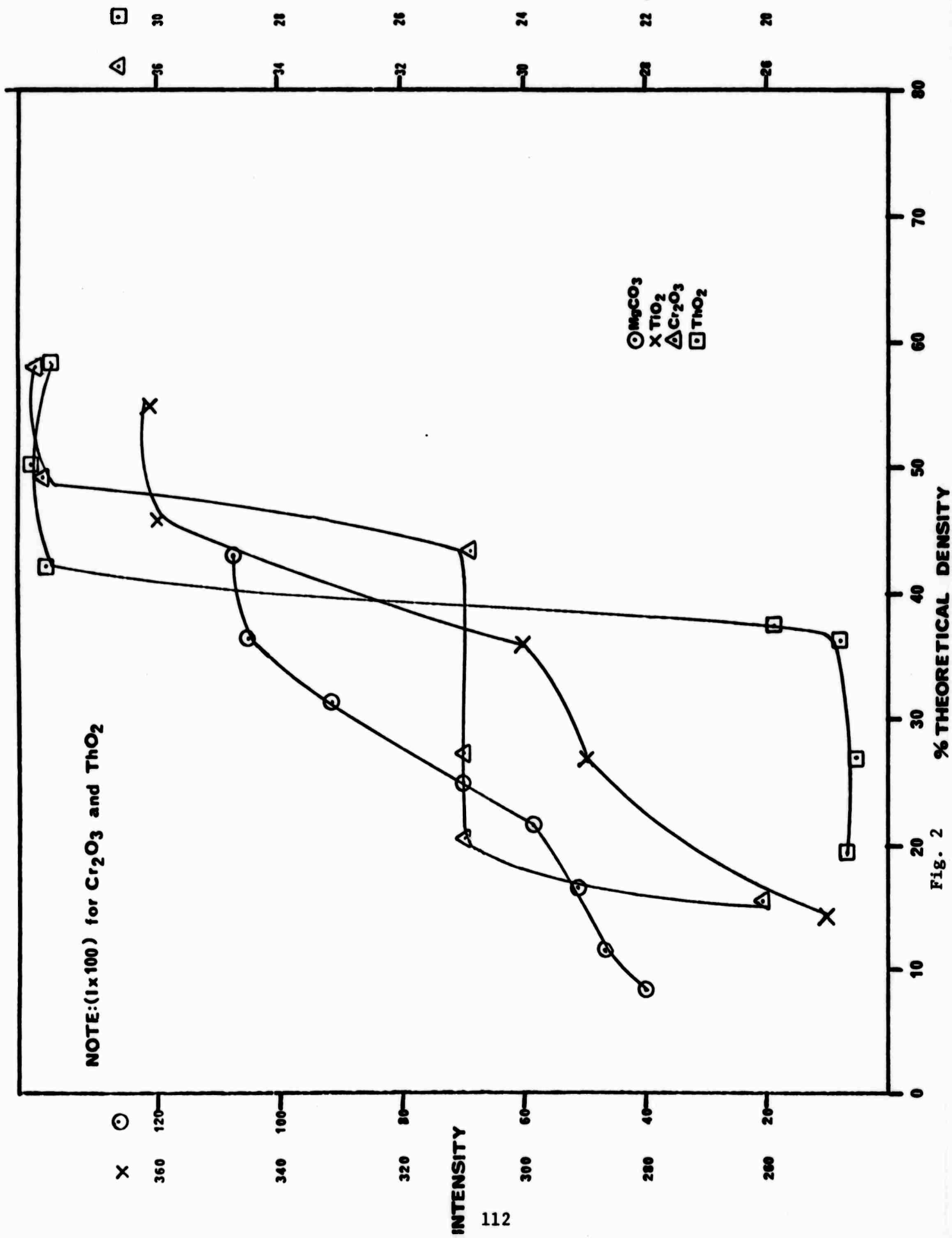


Fig. 2

range of densities in which the change in intensity with density is very small. The second region (II) in the density-intensity curve shows that a small change in density results in a large change in intensity. This effect is highly pronounced in magnesium carbonate. At high densities another regime of nearly independent x-ray intensities appear (Region III). In the case of  $\text{Cr}_2\text{O}_3$  Region I is preceded by another inflection in x-ray intensity, denoted as Region IA.

The range in density over which the three regions occur and the incremental change in x-ray intensity ( $\Delta I$ ) accompanying them is summarized in Table II. An average measured intensity ( $I_a$ ), independent of density fluctuations, is also given in Table II. The ratio  $\Delta I/I_a$  represents a potential analytical error if samples are pressed and analyzed without control of the pressed density. A summary of the density dependent errors for each of the regions of the compounds studied is also given in Table II.

The magnesium carbonate samples showed another very interesting phenomenon. Figure 3 shows that the x-ray intensity from samples pressed at 2,000 psi, with a density range of 0.73 g/cc to 0.75 g/cc, exhibited a significant dependence on the thickness of the pellet. The intensity increases from 65 cps to 73 cps as the thickness is increased from 0.4 cm to 1.51 cm. The same effect was observed for samples pressed at 6,000 psi with a density range of 0.93 g/cc to 0.95 g/cc. The intensity increased from 65 cps to 76 cps as the thickness increased from 0.2 cm to 0.75 cm. Samples irradiated from the

TABLE II

<u>Compound</u>	<u>Region</u>	<u><math>\rho_{th}^*</math></u>	<u><math>\Delta I</math></u>	<u>Average I</u>	<u>% Error</u>
MgCO <sub>3</sub>	I	8-22	12 cps	12 cps	23
	II	22-36	55	80	69
	III	36-43	2	105	2
TiO <sub>2</sub>	I	14-36	50 cps	275	18
	II	36-41	60	330	18
	III	41-54	10	360	3
Cr <sub>2</sub> O <sub>3</sub>	IA	15-20	500 cps	2850	18
	I	20-44	10	3100	3
	II	44-49	400	3450	12
	III	49-58.5	--	3800	0
ThO <sub>2</sub>	I	19-36	10 cps	1850	5
	II	36-42	1100	2500	44
	III	42-58.2	20	3150	6

\*% of theoretical density

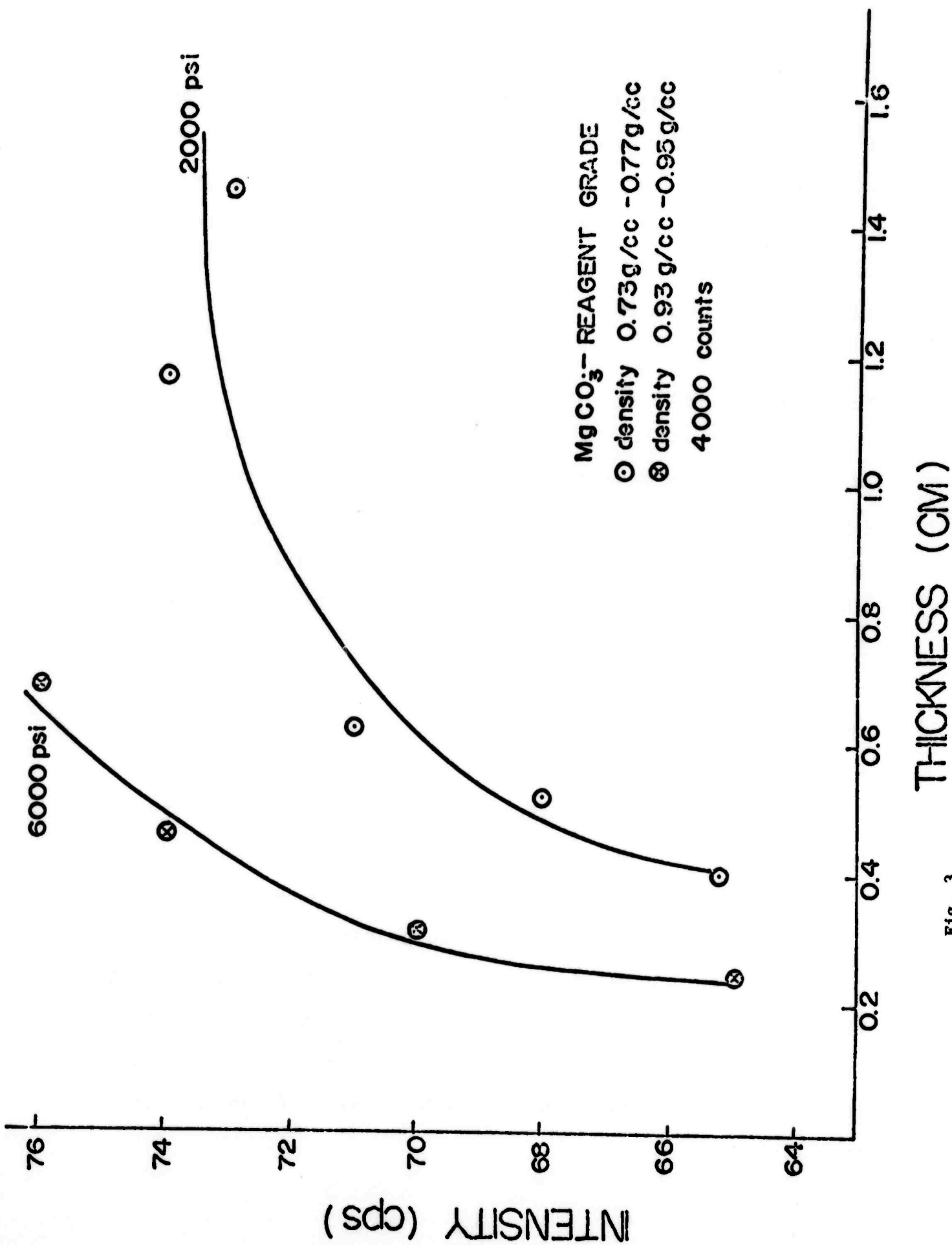


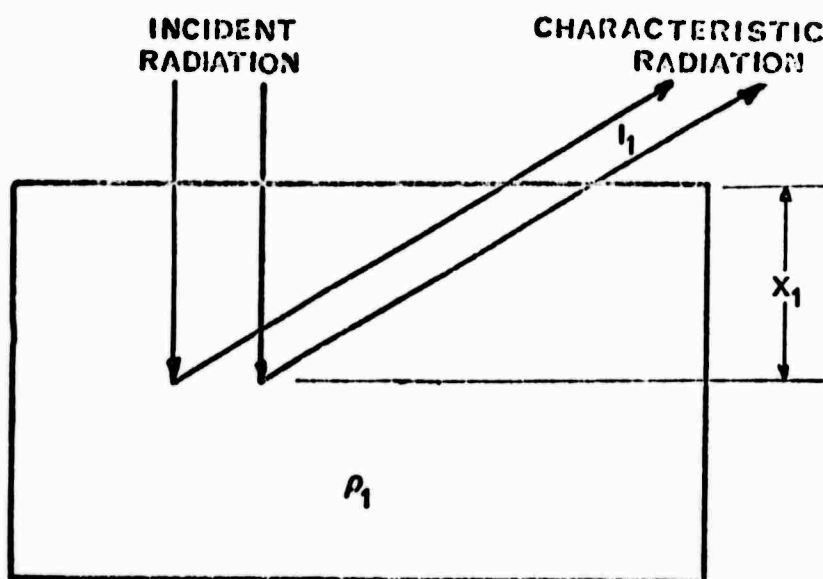
Fig. 3

surface directly exposed to the plunger in the pressing operation give correspondingly higher intensities than those irradiated from the bottom of the sample, away from the plunger.

The other three compounds investigated showed no dependence of intensity on thickness or variation of intensity when irradiated on the top and bottom.

### Discussion of Results

Magnesium carbonate is considered separately from the others due to its unusual thickness dependence. The explanation for its behavior is based on the fact that magnesium is a less efficient x-ray absorber in comparison with heavier elements. Therefore, the x-ray beam penetrates to an appreciable depth in the sample before being totally absorbed. Figure 4a illustrates the point that when the incident radiation penetrates the porous powder sample of density  $\rho_1$  to a depth of  $X_1$ , the measured intensity is  $I_1$ . If the internal density of the sample is uniform, the characteristic intensity can be expected to remain constant at  $I_1$  even if the bulk density of the sample changes. To see this behavior, compare Figure 4a with Figure 4b. Although the incident radiation penetrates to a greater depth in a low density sample ( $X_1$ ), the amount of characteristic radiation that gets to the counter from this depth is the same as that from a smaller depth in a denser sample ( $X_2$ ). Thus, intensity is not a function of sample density if the density is uniform.



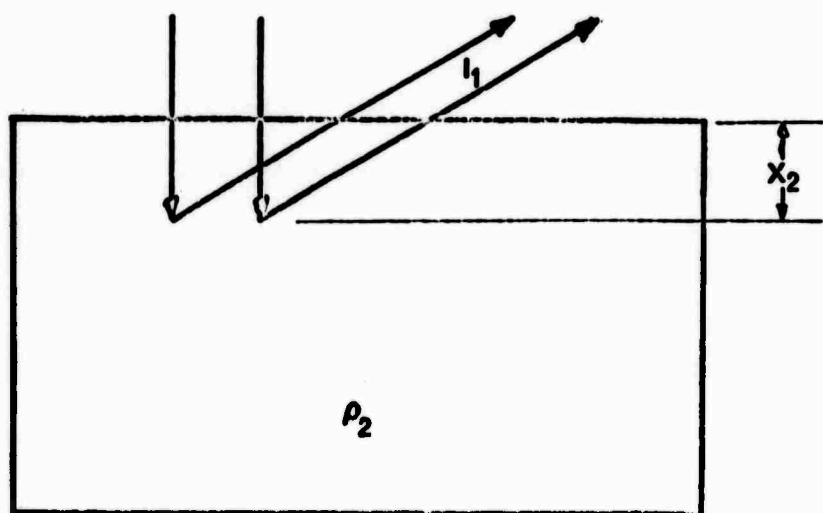
(a)

$$x_1 > x_2$$

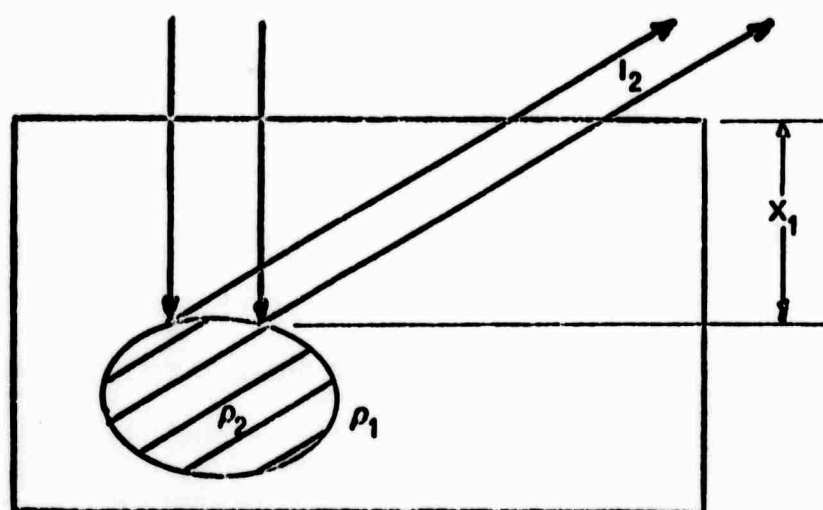
$$I_2 > I_1$$

$$\rho_2 > \rho_1$$

$\rho_1$  and  $\rho_2$  of uniform density.



(b)



(c)

Fig. 4



However, assume that some forming pressure produces the density configuration shown in Figure 4c. If the incident radiation penetrates to the surface of the high density region, a greater amount of characteristic radiation will be produced from this area than the area above it. The more characteristic radiation excited from a given depth within the sample the greater the probability that a given fraction will reach the detector. The measured intensity will be increased to  $I_2$  at the pressure that creates the inhomogeneous regions of density. Thus, intensity can be a function of forming pressure if density gradients exist within the sample.

David Train et al.<sup>(2)</sup> has shown that when powders of magnesium carbonate are pressed density gradients are introduced into the sample. The density gradient distribution depends on the pressing pressure as well as the thickness of the sample.

The initial region of the density-intensity curves in which  $dI/d\rho$  is small can be explained by the fact that although the bulk density is increasing, the local density which is exposed to incident radiation, is remaining fairly constant. Therefore, the measured intensity does not change.

The second region in the density-intensity curve corresponds to a large  $dI/d\rho$ . Train's results show that within this range of densities there is a large change in local density with only a small change in bulk density. Therefore, the intensity changes by a large factor with just a small change in bulk density. In other words, the small change in bulk density is sufficient to bring a high density region close enough to the top of the sample to be exposed to the incident radiation.

The third region of the density-intensity curve is a plateau. Train's results show that within this region there is not much change in local density with bulk density. Thus,  $dI/d\rho = 0$  (Figure 2).

The x-ray results show that there is also a dependence of intensity on sample thickness for magnesium carbonate powders (Figure 3). Train's data are evidence that samples of different thicknesses pressed to the same density have different density gradients. An adaptation of their results is shown in Figure 5. The figure illustrates that the higher the forming pressure the greater the changes in local density with a change in thickness. It was seen that a sample pressed at 2,000 psi and 1.50 cm thick gives a lower intensity than a sample pressed at 6,000 psi and 1.50 cm thick. A sample pressed at 6,000 psi gives a greater change in intensity if the sample thickness is increased to 1.75 cm than does a sample pressed at 2,000 psi with a corresponding increase in thickness. Consequently, the observed thickness and pressure dependence of  $dI/d\rho$  is consistent with Train's density gradient results.

The regions of the intensity-density curves for the other three compounds can be explained in a similar manner. The curve for titanium dioxide resembles that of magnesium carbonate because titanium is a light element, also. The curves for chromium oxide and thorium oxide show a larger  $dI/d\rho$  in the second region than do the lighter compounds, because the local density in the irradiated volume changes more rapidly for the heavier compounds. The fact that there is no intensity

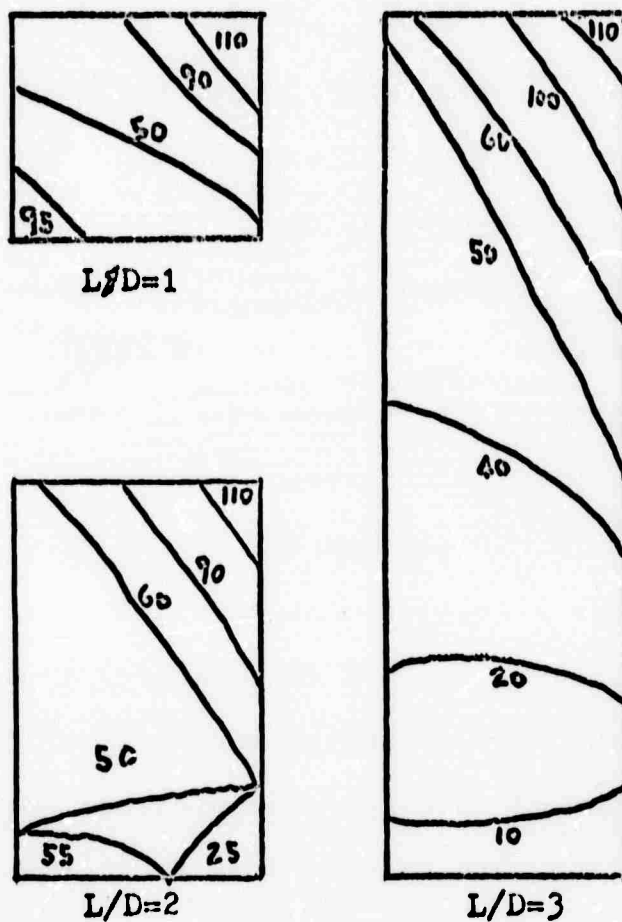


Fig. 5 Density distribution in  $\text{MgCO}_3$  sample pressed at 10,000 psi.

dependence on thickness for titanium dioxide, chromium oxide and thorium oxide is due to the larger mass absorption coefficients of these compounds and that changes in local density gradients as a function of thickness are not as large as for magnesium carbonate. Very large length to diameter ratios must be used before thickness variations become important for compounds containing heavier elements.

### Conclusions

The results of this paper indicate that in order for an accurate x-ray spectrochemical analysis of pressed powder specimens to be determined, the following rules should be observed:

- 1) The density of the sample should be carefully controlled for all materials if the pressed density lies in the region where  $dI/d\rho$  is large. The best results are obtained when samples are pressed in the density range where  $dI/d\rho \sim 0$ . This is usually Region III.
- 2) The thickness of the sample is very important for compounds containing the lighter elements. All samples should be the same thickness for reproducible results to be obtained.
- 3) The sample thickness is not an important factor for compounds containing the heavier elements ( $Z > 20$ ).

### References

1. L. S. Birks, X-ray Spectrochemical Analysis, Interscience Publishers, Inc. New York.
2. D. Train, "Transmission of Forces Through a Powder Mass During the Process of Pelleting," Trans. Instn. Chem. Engrs., Vol. 35, pp. 258-266, 1957.

#### IV. Measurement Techniques (R. W. Gould, L. L. Hensch, and J. J. Hren)

##### A. STRUCTURE OF SURFACE DEFECTS (D. L. Stoltz and J. J. Hren)

###### Introduction

In the past decade the properties of solid surfaces in electronic, mechanical and chemical phenomena have been gradually recognized as being more and more important. The influence of different types of defects and their distribution in the bulk structure of materials has been studied in depth and utilized to explain various observed bulk properties. The advent of ultra-high vacuum capabilities and sophisticated observational methods, such as transmission electron microscopy, field-ion and electron-emission microscopy and low energy electron diffraction, now creates the possibility to extend defect structural analysis to surfaces and to correlate this analysis with the physical properties of solid surfaces.

Ideally, surfaces of crystalline materials represent the abrupt termination of the periodic array of the crystalline structure. Because of the inherent complexity of real surfaces, however, several viewpoints should be considered to gain a complete picture. For example, the atomic arrangement, electronic configuration, and nature of surface defects need to be correlated with various surface-dependent physical properties. Such properties are directly dependent upon the nature of the surface. Such properties include: electrical surface conductance, electronic work function, surface tension, and interaction of the surface with gas, liquid and solid phases. Pertinent Phenomena for solid-gas interfaces include physical adsorp-

tion, chemisorption, and oxidation or film formation. Examples of solid-liquid interfacial phenomena are electrical double layers, electrode equilibrium and kinetics, and corrosion. Solid-solid interfaces are associated with grain boundaries, p-n junctions, rectifying contacts, and dissimilar solids in physical contact.

To analyze surface defects one must utilize techniques involving both "clean" and "real" surfaces. Studies of "clean" surfaces, which ideally represent an atomically flat surface void of any contaminating atoms, provide a necessary means for developing fundamental concepts and the required theoretical models to explain various observed intrinsic surface structures. Experimental information for "real" surfaces, on the other hand, will provide the basis for understanding the kinetics and energetics involved in different observed phenomena and physical properties.

The importance of bulk defects is already known for semiconductor devices. Point defects, such as impurity atoms, strongly influence the electrical properties of the devices, particularly the minority carrier lifetime. In addition, dislocations have been shown to increase the diffusion rate of both acceptor and donor atoms as compared to the perfect material. Queisser et al.,<sup>(1)</sup> for example, have attributed this rate increase to the formation of dopant atmospheres at dislocations, enhanced diffusion by vacancy mechanisms, and lowered activation energies. In

turn, this enhanced mass transport disrupts the sharp impurity concentration gradients within the devices by the build-up of impurity atoms into dislocation atmospheres and, sometimes, in the formation of precipitates. These structural changes then create short circuits between the emitter and collector regions and cause reduced device lifetime. A similar structural change, involving precipitates of heavy metals in p-n junctions, results in raising the reverse currents (called softening) to such a degree that drastic failures occur. Several workers<sup>(2)</sup> have mentioned that these precipitates nucleate at dislocations and second-order twin boundaries and report that diodes with high dislocation contents and second-order boundaries were soft, while diodes with lower line defect densities showed desirable reverse current-voltage characteristics.<sup>(3)</sup> It seems apparent that defect-free materials would be desirable for semiconductor devices. However, in 1960 empirical tests of transistors and diodes made from dislocation-free silicon indicated no superiority compared with devices made from materials with moderate dislocation densities.<sup>(4)</sup> It was interesting that subsequent investigations revealed that the reason for this (at first blush) surprising lack of superiority of the perfect material was simply that the material was not free from defects following the manufacturing processes.<sup>(5)</sup>

Briefly, one can state various possible and recognized means of introducing defects in solid state electronic



devices. These include:

1. variation in dopant concentrations in single crystals which produce spiral-like patterns of impurity atoms. Such spirals of impurity atoms, according to Goetzberger,<sup>(6)</sup> result in diodes exhibiting a striated surface with low breakdown voltages.
2. introduction of dislocations during slicing of single crystals and mishandling prior to heat treatment.
3. nucleation and growth of precipitates of impurity atoms during heat treatment.
4. introduction of interstitial point defects at the surface of the single crystal by diffusion of impurity atoms.
5. coalescence of point defects and rearrangement of dislocation arrays during application of high electric fields.

#### Methods of Observation

From the preceding one recognizes that the bulk and surface defects in materials play a major role in determining the materials performance in various applications. It seems appropriate, therefore, to briefly describe various means of observing surface and bulk defects.

Several optical methods exist for revealing the presence of dislocations on the surface and interior of the crystal. Etching techniques expose dislocations at the surface by forming pits at their points of emergence with the surface. Initiation of these pits appears to be related to impurity atmospheres and local lattice strain associated with dislocations intersecting the surface.<sup>(7)</sup> This technique is particularly valuable for determining low dislocation densities and observing general dislocation arrangements. Another method of optical observation of dislocations is the decoration technique. Wherein one intentionally causes the separation of a second phase to occur preferentially on the dislocations. This technique permits surface and volume arrays to be observed optically. Figure 1 represents a dislocation network of mixed type in KCl, decorated with particles of Ag. Dash<sup>(8)</sup> has also observed copper decorated dislocations in silicon by using infra-red radiation. However, the decoration technique is clearly restrictive, since the thermal diffusion treatments required to decorate the dislocations can modify the dislocation arrangement and in any event leave it permanently altered. The general phenomenon of photoelasticity can be also used to reveal dislocations, since the lattice strain around a dislocation causes an isotropic crystal to become birefringent. Kear and Pratt,<sup>(9)</sup> for example, used a polarizing microscope to study quenching strains in rock salt, so that the colored

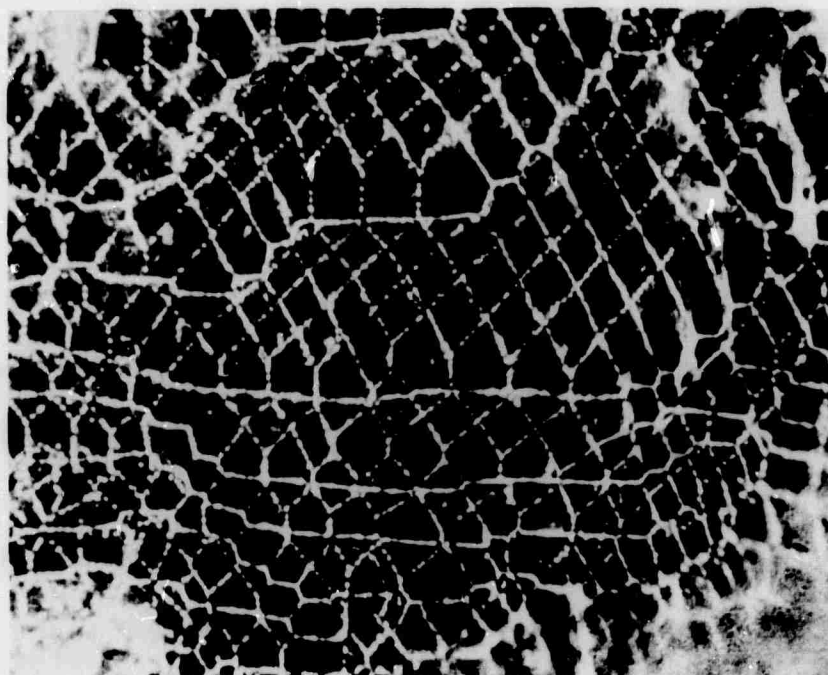


Fig. 1. Network of mixed dislocations in KCl, decorated with silver particles. (Amelinckx, S., *Acta Met.*, 6, 34 (1958).)

birefringent bands were sharply visible and could be related to the different signs of the dislocations. Indenbohm<sup>(10)</sup> utilized all three of the above optical techniques on the same sample and obtained a perfect correlation.

Due to the opaqueness and high dislocation content of many materials, however, other observational techniques have been developed that utilize various higher energy incident beams. One such method is the transmission electron microscopy. Hirsch<sup>(11)</sup> and Bollman,<sup>(12)</sup> independently, first obtained high magnification images of line defects in thin foil sections of aluminum and stainless steel respectively. These dislocations are made visible in the electron microscope by means of diffraction contrast arising from the strain field associated with the dislocations. Thus, the trace of the dislocation line itself is observed. This well known technique has proven itself very successful in observing and studying dislocations, antiphase boundaries, point defect aggregates, dislocation loops, stacking faults, dislocation interactions and arrays, second phase particles, and Guinier-Preston zones. Overall, this method has probably contributed more to our understanding of bulk crystalline defects than any other, but we will not comment further on it here because of the already extensive literature extant.

A monochromatic x-ray beam will also pass through a crystal and yield contrast effects very similar to transmission electron microscopy. This observational method is particularly suited to materials with low defect

density and has been used increasingly in recent years. Two such methods are the Berg-Barrett<sup>(13,14)</sup> and Lang<sup>(15,16)</sup> techniques. Of these the Lang method appears most promising for producing topographs from crystals with optically flat "real" surfaces. These projection topographs represent dark field images and the diffracting conditions are readily controlled and defined. One application of this technique is the determination of Burgers vectors from paired projection topographs.<sup>(17)</sup> Figure 2 is an example and shows an enlarged section of a (224) topograph of a silicon wafer after boron diffusion. Notice the dark dislocations (thin bands) and precipitates (black spots). Stereographic pairs of such topographs (using  $(hkl)$  and  $(\bar{h}\bar{k}\bar{l})$  reflections) create a three dimensional representation of any dislocation structure.

All of the observational techniques just described have very limited utility in determining surface defect structures. The remaining discussion will therefore be primarily concerned with the use of the field-ion microscope which is probably most applicable for such studies. The method was initially developed by Müller<sup>(18,19)</sup> as a modified version of the electron-emission microscope.<sup>(20)</sup> A schematic diagram of the instrument is shown in Figure 3. The specimen is generally a small diameter wire which has been electrochemically polished to a very sharp point ( $\sim 1000 \text{ \AA}$ ), and field evaporated to produce a nearly atomically



**Fig. 2.** 224 topograph of silicon after boron diffusion.  
(Schwuttke, G. H., AFCRL-66-192, p. 6-6 (1966).)

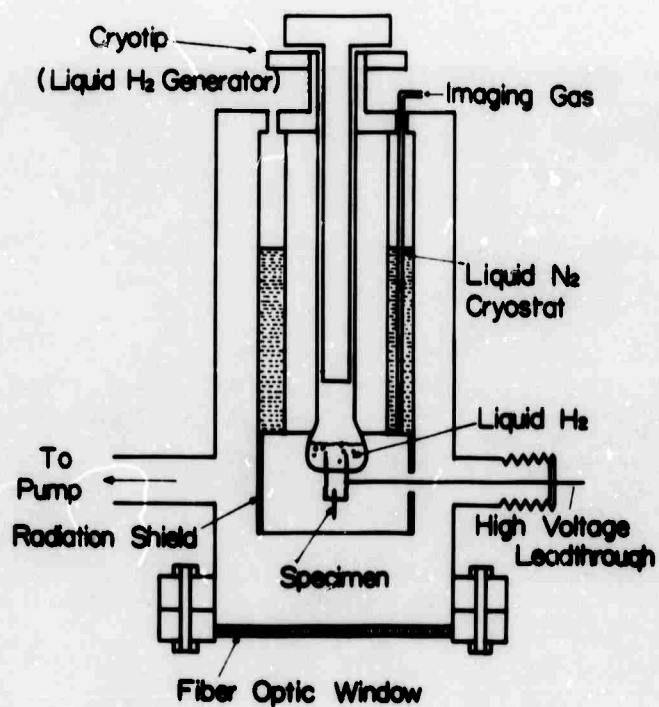


Fig. 3. Schematic diagram of field-ion microscope.

smooth, hemispherical surface. An imaging gas, usually helium, is introduced into the chamber and its atoms are ionized at the vicinity of the discrete atomic surface. These positive ions are repelled by an accelerating electrical field of approximately 450 MV/cm to the phosphor coated screen at ground potential.

The image formed by the field-ion microscope represents an enlarged projection of the detailed field distribution of the surface and depends sensitively upon local field strengths. The atomic structure of the surface greatly influences this field distribution, i.e., the protruding atoms create high local fields which in turn produce bright image points as shown in Figure 4. Note the numerous small circular facets present and that the atoms at the edges of these facets appear brightest because their protrusion leads to a high localized field strength. The symmetry of this image allows the various crystal faces to be identified crystallographically. Figure 5 illustrates that the path traveled by the ions is approximately normal to the local tip surface. The geometrical magnification is normally about  $10^6$ , as determined by the ratio of the distance from tip to screen to the radius of the tip.

It should be added that field-ion microscopy not only allows individual atomic observation of a surface, but by use of field evaporation, individual atomic layers can be removed to provide an atom by atom reconstruction of a



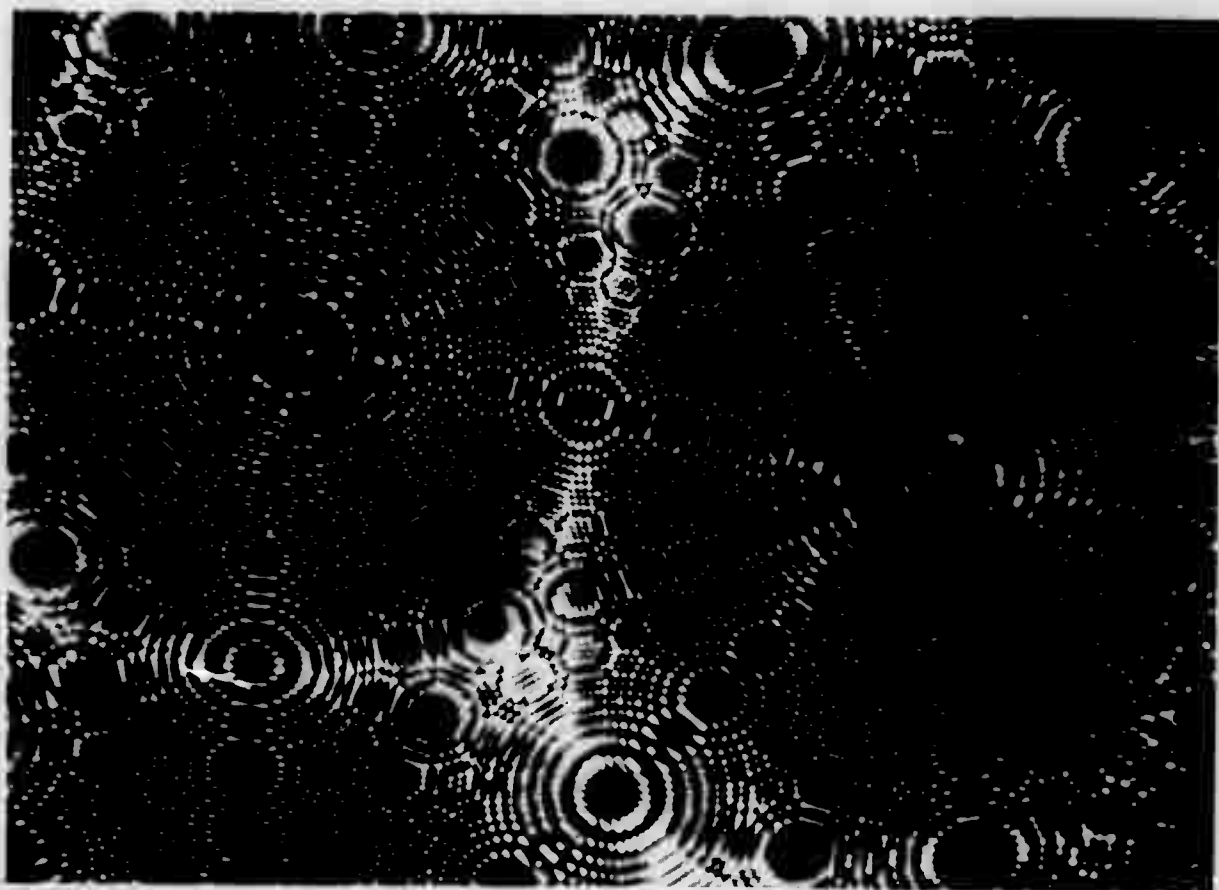


Fig. 4. Field-ion micrograph of platinum.

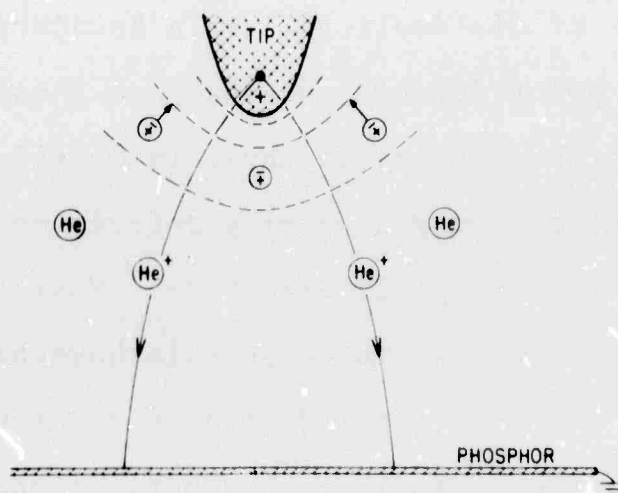


Fig. 5. Schematic illustration of path of ionized gas from specimen tip to phosphorus screen.

volume. Also, by using field evaporation in ultra-high vacuums (better than  $10^{-10}$  Torr), "clean" surfaces can be formed and retained for extended periods.

#### Interpretation of Surface Defects by Field-Ion Microscopy

Despite the various experimental difficulties in observing defects in the small hemispherical surfaces of the field-ion specimens, a number of researchers (of Ref. (21)) have obtained images of dislocations, grain boundaries, stacking faults and point defects and analyzed these in depth. We will describe several of these in detail.

One of the most commonly appearing defects detected in field-ion images is the spiral structure. Most often in discussions of crystal growth, these spirals have been described as resulting from the intersection of a screw dislocation with the surface. In fact, however, if one scrutinizes the basic literature on the geometry of dislocations, it becomes clear that any dislocation can give rise to an unending step or spiral ramp when it intersects a surface. For example, Cottrell<sup>(22)</sup> pointed out:

"Suppose that we have a family of parallel planes and project through them a dislocation line with a suitable Burgers vector which also projects through them. Then the structure is changed by the dislocation from a family of parallel planes into a single spiral surface or "helocoid." This property is true of edge, screw and mixed dislocations, but can be seen most easily in the case of screw dislocations which project vertically through the family of planes."

Papers by George<sup>(23)</sup> and Ranganathan et al.,<sup>(24)</sup> that explained spiral-like structures at grain boundaries and streaks in field-ion images respectively, were close in recognizing the correct interpretation. Pashley<sup>(25)</sup> presented a quantitative partial interpretation of dislocation images that included a mathematical description of the pitch of the helix structure about any dislocation line for which  $\hat{n} \cdot \vec{b} \neq 0$ , where  $\hat{n}$  is a unit vector normal to the (hkl) planes and  $\vec{b}$  is the Burgers vector. He stated: "It is important to realize that the effect of dislocations on the field-ion micrograph depends only on the component of the Burgers vector perpendicular to the (hkl) planes concerned. Thus, a dislocation showing a spiral structure is not necessarily a pure screw dislocation..." Ranganathan<sup>(26)</sup> independently developed these ideas while attempting to explain grain boundary structures in terms of dislocation networks. His work is more detailed than Pashley's, but is quantitatively the same. Ranganathan's terminology deduced the nature of a spiral from the dot product  $\vec{g}_{hkl} \cdot \vec{b}$  in analogy to electron microscope interpretations, where the reciprocal lattice vector is equivalent to

$$\vec{g}_{hkl} = h \vec{a}^* + k \vec{b}^* + l \vec{c}^* \quad (1)$$

By definition  $\vec{g}_{hkl}$  is perpendicular to (hkl) and has magnitude  $1/d_{hkl}$ , irrespective of crystal structure. The Burgers vector,  $\vec{b}$ , is a real lattice vector and proceeds from one

lattice point to another, if it is a total dislocation. It need not be (and normally is not) coincident with one of the basis vectors of the lattice, but it may always be written in terms of a constant  $K$  and the real basis vectors  $\vec{a}$ ,  $\vec{b}$ ,  $\vec{c}$  as:

$$\vec{b} = K(u \vec{a} + v \vec{b} + w \vec{c}) \quad (2)$$

The dot product is then the following:

$$\begin{aligned} \vec{g}_{hkl} \cdot \vec{b} &= (h \vec{a}^* + k \vec{b}^* + l \vec{c}^*) \cdot (u \vec{a} + v \vec{b} + w \vec{c})K \\ &= K(h u + k v + l w) \end{aligned} \quad (3)$$

where the quantity in brackets is clearly either zero or an integer. The constant  $K$ , therefore, determines whether the dot product is an integer or not. If  $\vec{b}$  is a total dislocation,  $K$  is either zero or an integer since  $\vec{b}$  goes from one lattice point to another. On the other hand, if  $\vec{b}$  is a partial dislocation (superlattice dislocations may be included in this definition),  $K$  may be such as to give a fraction for the dot product. The  $\vec{g}_{hkl} \cdot \vec{b}$  criterion can be illustrated by considering the real lattice vectors of a cubic lattice. The reciprocal lattice vector  $\vec{g}_{hkl}$  may be expressed as:

$$\vec{g}_{hkl} = \frac{\hat{n}_{hkl}}{d_{hkl}} \quad (4)$$

where  $\hat{n}_{hkl}$  is unit normal vector to  $(hkl)$  and  $d_{hkl}$  is interplanar spacing. Using the following identities

$$\hat{n}_{hkl} = \frac{[hkl]}{(h^2 + k^2 + l^2)^{1/2}} \quad (5)$$

and

$$d_{hkl} = \frac{a_0}{(h^2 + k^2 + l^2)^{1/2}} \quad (6)$$

where  $a_0$  is the unit cell dimension, equation (4) becomes

$$\vec{g}_{hkl} = [hkl]/a_0 \quad (7)$$

Consider a Burgers vector in the face centered cubic structure,  $\vec{b} = a_0/2 \langle 110 \rangle$ , then by substituting into equation (4), one obtains

$$\vec{g}_{hkl} \cdot \vec{b} = \frac{1}{2} [h + k] \quad (8)$$

or the equivalent expression depending on the exact Burgers vector value. Since the possible (hkl) planes in face centered cubic structures have all odd or all even indices, the last equation is always zero or an integer. The quantity  $\vec{g}_{hkl} \cdot \vec{b}$  may be, thus, thought of as being the projection of the Burgers vector,  $\vec{b}$ , on the unit vector  $\hat{n}$  in units of  $d_{hkl}$ .

An alternate way to state this, due to Smith et al.,<sup>(27)</sup> is as follows: "Characterize a surface facet of a field-ion specimen by its normal  $\hat{n}_{hkl}$ . Then the Burgers vector of a dislocation is given by the closure failure in the Burgers circuit.<sup>(28)</sup> But this is independent of the circuit selected, as long as it is always taken in good crystal." Consider the schematic description of this statement in Figure 6. One notes that when the Burgers vector lies in

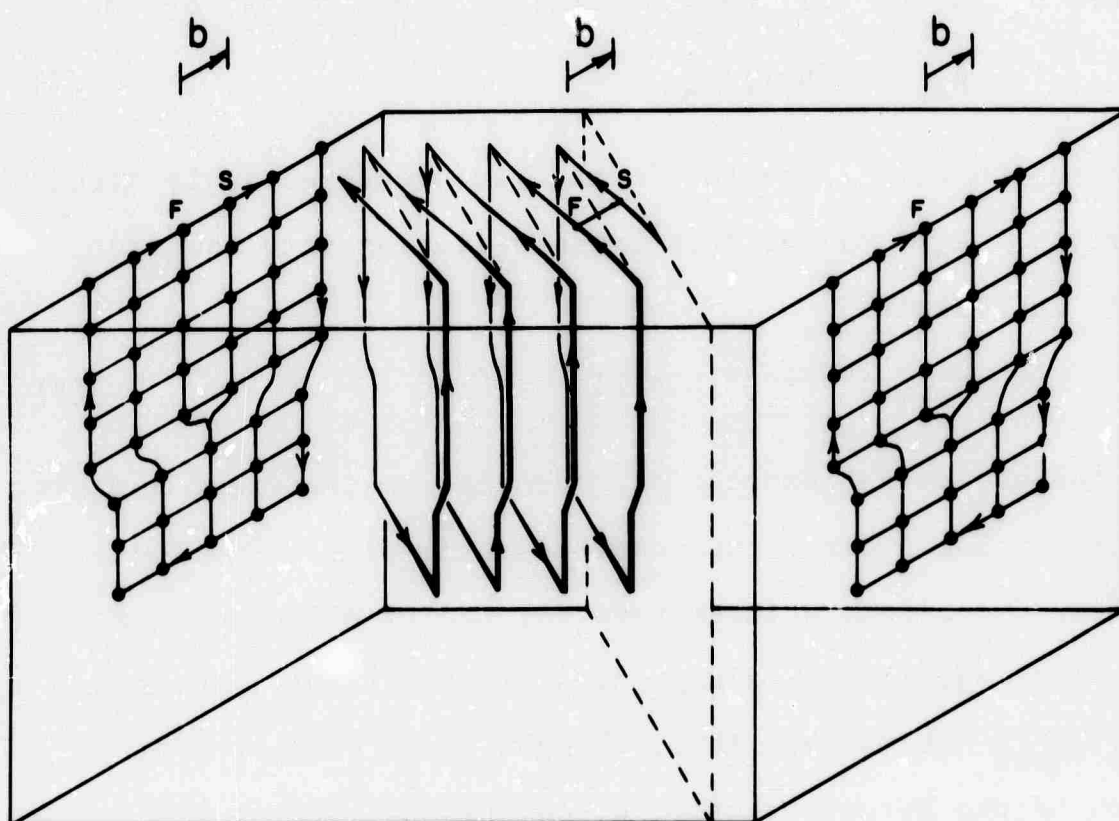


Fig. 6. Pure edge dislocation's intersection with rational surfaces, illustrating creation of spiral surface.

the plane of the surface, it is defined by a Burgers circuit lying in that surface also. If the Burgers circuit is taken for this identical edge dislocation on an arbitrary plane surface, it will be converted into a spiral surface to retain its original direction and magnitude. Utilizing the  $\hat{n}_{hkl} \cdot \vec{b}$  expression to define the pitch of the dislocations spiral, where  $\vec{b}$  is equal to the lattice vector and the  $\hat{n}_{hkl}$  represents a rational plane, this dot product must be an integral number of interplanar spacings.

The conclusion to be emphasized is that, except for the relatively rare case where the Burgers vector of a dislocation intersecting the surface lies in the plane of the surface, all dislocations will produce an unending surface ramp which extends over large regions of the surface. Thus, if the surface is truly atomically flat, the step would proceed from the emergence point of the dislocation line to the edge of the piece, as shown in Figure 6. If the surface has a long range curvature, such as the hemispherical field emitter surface, the step adopts the character of a spiral when viewed from above. Figure 7 illustrates that the sense of the spiral can be established by the sense of the Burgers vector with respect to the (hkl) planes of interest, i.e., when the Burgers vector points inward the spiral has one sense and when it points outward the spiral has the opposite sense.

Since the character of the dislocation is not required to predict the nature of the expected spiral structure,



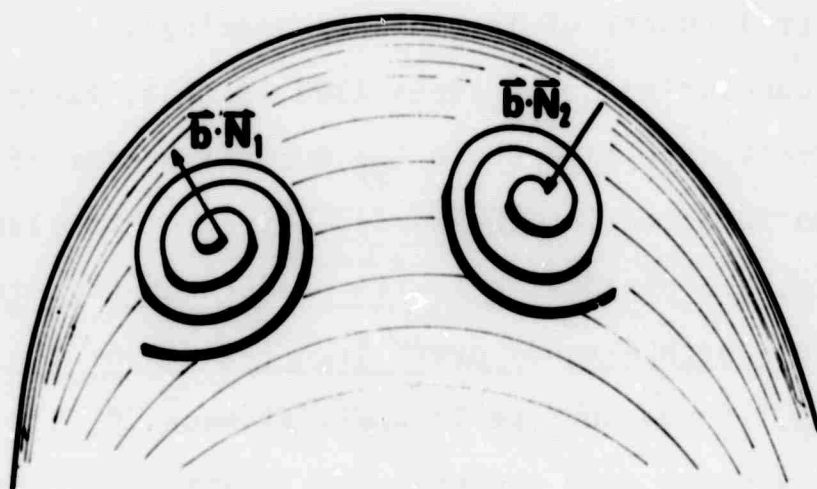


**Fig. 7.** Schematic drawing indicating relationship between sense of spiral formed on surface of hemisphere when intersected by a dislocation with the direction of the normal component of the Burgers vector.

computer models can be devised, based only upon the Burgers vector and the plane intersected by the dislocation to test the predictions of the  $\vec{g}_{hkl} \cdot \vec{b}$  criterion. Utilizing arbitrary dislocations and available mathematical descriptions of the atomic displacements around the dislocation, the geometry of the unending ramp may be accurately simulated in a digital computer. Sanwald and co-authors<sup>(29)</sup> first selected a pure screw dislocation, defined by a Burgers vector,  $\vec{b} = \frac{a_0}{2} [110]$ , intersecting a family of the  $\{420\}$  type planes. The (204) pole is reproduced in Figure 8 and illustrates the single spiral from the  $\vec{g}_{hkl} \cdot \vec{b}$  criterion. Figure 9 corresponds to an experimental field-ion image of a single spiral and verifies the geometrical foundations of the spiral hypothesis.

A more complicated spiral structure was developed by assuming two closely spaced dislocations with  $a_0/2 \langle 110 \rangle$  Burgers vectors intersecting the image near the (113) planes of a FCC lattice. By selecting for this computer simulation the Burgers vectors  $\vec{b}_1 = a_0/2 [011]$  and  $\vec{b}_2 = a_0/2 [0\bar{1}1]$  and assuming them to be separated by 10 Å in the specimen, the resulting image shown in Figure 10 is obtained. The experimental image of iridium near the (113) plane, found in Figure 11, shows good qualitative agreement with the computer simulated image.

When the dislocation intersection does not emerge from the center of the pole (Figure 8), one obtains images

## (204) POLE



Fig. 8. Computer simulated image of pure screw dislocation emerging at center of the (204) pole to produce single leaved spiral.



**Fig. 9.** Experimental field-ion micrograph of an Ir specimen containing a single spiral.

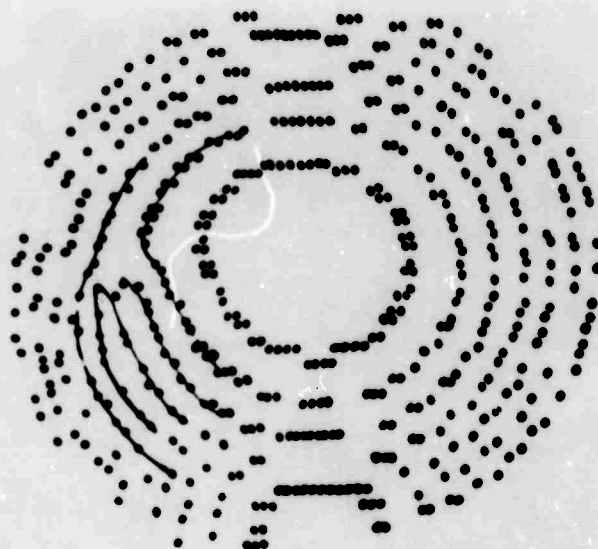


Fig. 10. Computer simulated image of triple spiral caused by pair of noninteracting dislocations.

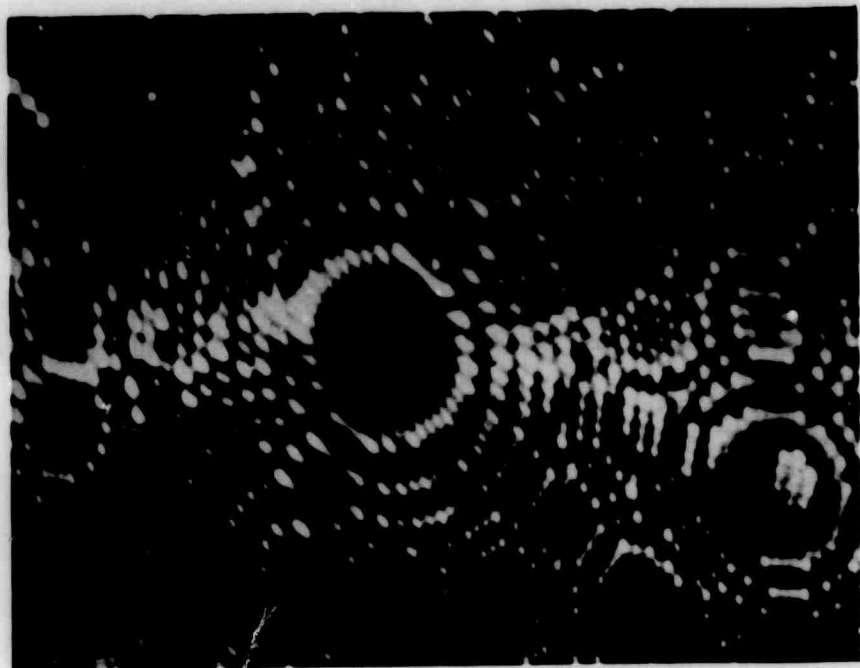
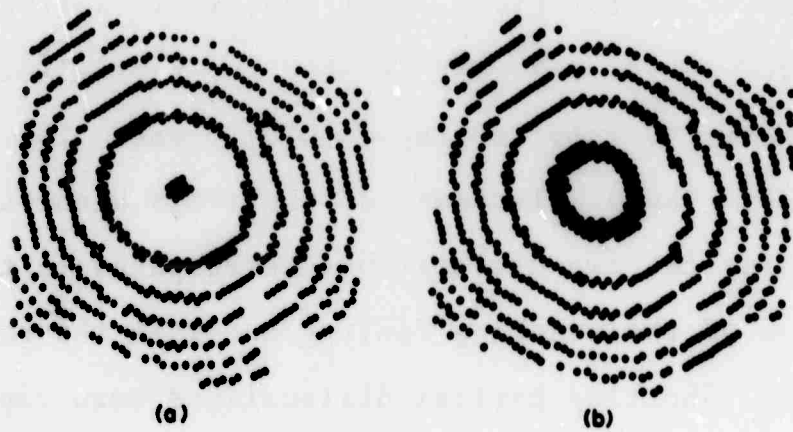


Fig. 11. Triple spiral on (113) plane of an Ir specimen.

similar to Figure 12. Figure 12a represents a pure screw dislocation causing a single spiral on the (204) plane. Note that the only difference between Figures 8 and 12a is the point of emergence of the pure screw dislocation. When analyzed in terms of the expected single spiral structure, the result is obviously correct, yet if such a structure was observed experimentally it could be easily misinterpreted as showing an extra half-plane and be mistaken for an edge dislocation.

Figure 12b, on the other hand, illustrates the simulated image of a pure edge dislocation in the same location of the crystal facet as the pure screw dislocation in Figure 12a. There is little difference in the appearance of the two images. The same single spiral structure is predicted in both cases and only the diameters of the rings appear to be different (in the computed images). This latter effect is due simply to the sensitivity of the computer model to the exact tip radius,<sup>(30)</sup> which was slightly different in the neighborhood of the pole in each case. Figures 12a and 12b point up the need for careful interpretation of experimental field-ion images to accurately characterize the spiral structures.

So far attention has been directed primarily to the interpretation of surface steps caused by total dislocations. Straightforward application of the  $\vec{g}_{hkl} \cdot \vec{b}$  criterion to partial dislocations of the type  $a_0/6 \langle 112 \rangle$  and stacking



**Fig. 12. Pure screw and edge dislocations causing single spiral on (204) plane edges.  
(\* = point of emergence of dislocation)**



faults will be illustrated in the FCC structure. Although each partial dislocation will not yield a step with an integral number of d-spacings, a pair of partial dislocations together yields a whole dislocation with a Burgers vector from one lattice point to another. (This argument also applies for super dislocations in ordered alloys.) Consequently, the long-range effect must give a step with an integral number of d-spacings, as illustrated previously for total dislocations. The stacking fault, between the pair of partial dislocations, will contribute a fractional step. Figure 13 shows a pair of Shockley partial dislocations,  $a_0/6 \langle 112 \rangle$ , intersecting a (220) plane. The total  $\vec{b}$  is  $\frac{a}{2} [101]$ . The displacement of the rings along a great circle joining the two dislocations corresponds to the intersection of the stacking fault plane with the surface. Since the two Shockley partial dislocations were separated by a small distance, this disturbance appears along a straight line joining the two emergence points of the dislocations. Away from each of the dislocations one notices a single spiral which is expected from the total dislocation from which the pair has dissociated. Experimental confirmation of this analysis comes from a recent study by Newman et al., (31,32) which revealed a Frank loop and its associated stacking fault. The stacking fault can be seen as a streak connecting the two spirals of opposite sense in Figure 14. This configuration was simulated as a Frank

### Stacking Fault on (220) Pole

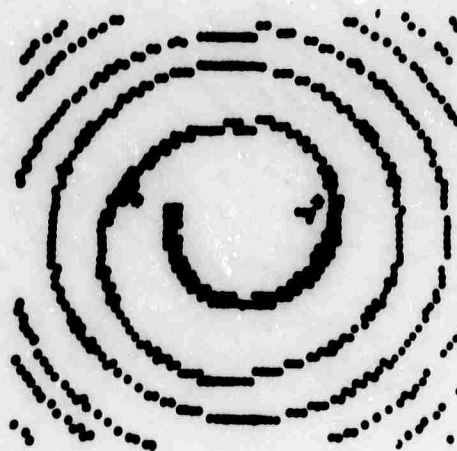


Fig. 13. Pair of Shockley partial dislocations and associated stacking fault intersecting (220) plane; total  $\vec{b} = a/2 [101]$ . (\* = point of emergence of dislocation)

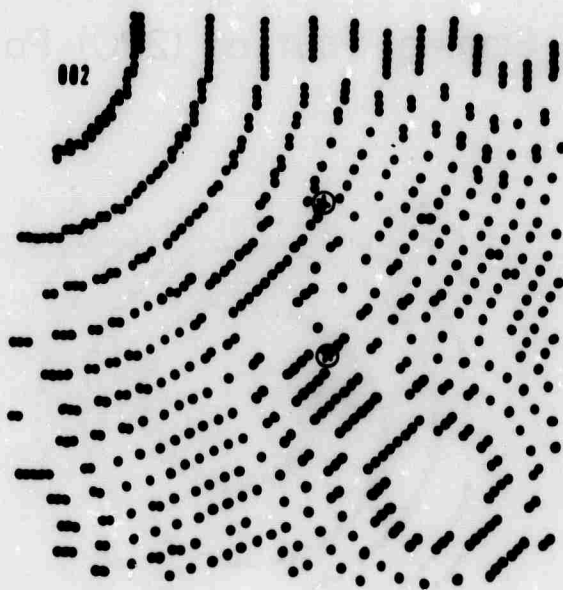


Fig. 14. Computer simulation of Frank loop with associated stacking fault.

loop on the computer and the result is shown in Figure 15. The agreement is clearly very good.

Since all dislocations which have a component of their Burgers vectors normal to the surface will produce steps if they intersect it, it is instructive to calculate the amount of new surface created thereby. This will also serve to illustrate the potential importance of surface defects on physical and chemical properties. Using an extension of the  $\vec{g} \cdot \vec{b}$  criterion, it is possible from pure geometry to write the expression:

$$A_s = [(\vec{g}_{hkl} \cdot \vec{b}_i) d_{hkl}] \rho_{b_i} |L|, \quad (9)$$

where  $A_s \equiv$  surface area created by the dislocation

$\vec{g}_{hkl} \equiv$  reciprocal lattice vector of (hkl)

$\vec{b}_i \equiv$  Burgers vector of  $i^{\text{th}}$  dislocation

$d_{hkl} \equiv$  interplanar distance (hkl)

$\rho_{b_i} \equiv$  density of dislocations with Burgers vector  $b_i$

$|L| \equiv$  parameter which corresponds to average step length from point of emergence of any dislocation to edge of planar area.

An order of magnitude for  $A_s$  may be obtained from Equation (9) by assuming the following values:

$$\rho_{b_i} = 10^8 \text{ cm/cm}^3$$

$$\vec{g}_{hkl} = [111]$$

$$\vec{b}_i = a/2 [110]$$



**Fig. 15.** Extreme blow-up of region containing a Frank loop with associated stacking fault. Note the streak connecting the two spirals of opposite sense.

$$d_{hkl} = 2 \times 10^{-8} \text{ cm}$$

$$|\vec{L}| = 1/2 \text{ cm}$$

The resulting value of  $A_s$ , created by dislocations, is  $1 \text{ cm}^2$ , the same as the nominal initial surface area of the sample!

This amount of new surface area must markedly affect the properties of the material's surface. For instance, in metallic samples these surface steps could develop electric double layers, whereas in ionic materials localized dipole regions could be formed. For covalently bonded materials, such as silicon and germanium, these steps could create a significant increase in the number of dangling bonds. It follows that surface step structures from dislocation intersections must markedly affect the electronic, chemical and mechanical properties of real surfaces in general.

Point defects also may be observed and analyzed by field-ion microscopy. Use of controlled field evaporation permits identification of single lattice sites on the specimen's surface.<sup>(33)</sup> Since field evaporation removes atoms almost exclusively from edge sites, the appearance of a void in the interior of a fully resolved atomic surface corresponds to a vacancy. Therefore, the concentration and distribution of vacancies can be determined from the field-ion micrographs. Point defects may affect many other properties of the surface as well. For example, vacancies and aggregates of vacancies on the

surfaces of ultra-high vacuum-cleaved rock salts contribute significantly to the nucleation and growth of single crystal thin films. Rhodin et al.<sup>(34)</sup> have reported recently that surface vacancies created by electron irradiation provide nucleation sites favoring the formation of oriented nuclei for an epitaxial layer of gold, silver, or copper on KCl. Another recent study of epitaxial deposition of platinum on iridium was made by Graham et al.<sup>(35)</sup> using the field-ion microscope. Their results indicate that the incident platinum atoms preferred to be trapped selectively in the most energetically stable positions on the surfaces, i.e., those positions representing vacancies, not depressions, in the iridium surface.

In similar ways, defects, other than those described, can be quantitatively studied via field-ion microscopy and the image interpretation aided by computer simulated models. These include, for example, grain boundaries and anti-phase boundaries in ordered alloys. Some studies have been made, but many more remain to be carried out.

#### Summary and Conclusions

Although the observational techniques and identification procedures of various surface defects have been discussed, the actual role surface defects play in affecting electronic and chemical properties still needs to be

evaluated in detail. A more complete understanding of the complex nature of surface defects requires an integrated investigation involving not only the characterization of the surface and its defects but also the correlated determination of particularly important physical properties as well. The experimental techniques would certainly include: field emission, low-energy electron diffraction, Auger spectroscopy, photo-electric emission and optical properties. Such studies, for instance, would involve determinations of surface conductivity and electronic work functions for similar specimens with varying defect content and type. By controlling the environment and surface structure measurements could be made on "clean" and "real" surfaces of the same bulk material. Another possibility would include evaluation of a material's chemical reactivity as a function of its surface area and structure, as in catalysis, oxidation, or adsorption. Similarly, further studies involving the nucleation and growth of thin films (or epitaxial layers) on various substrates must be conducted. Various means of computer aided calculation of both the geometric and electronic properties of surfaces exist and should be employed with all of the experiments suggested. Suitable tools are now at hand and, with perhaps slight modifications, we should employ them actively to fulfill a long vacant information gap.



## REFERENCES

1. Queisser, H. J., Hubner, K., and Shockley, W.,  
Phys. Rev., 123, 1245 (1960).
2. Goetzberger, A. and Shockley, W., J. Appl. Phys., 31,  
1891 (1960).
3. Queisser, H. J., J. Electrochem. Soc., 110, 52 (1963).
4. Taylor, W. E., Dash, W. C., Miller, L. E. and Mueller,  
C. W., Properties of Elemental and Compound Semicon-  
ductors, edited by H. C. Gatos, Interscience  
Publishers, New York and London, p. 377 (1960).
5. Schwuttke, G. H., Proceedings of the International  
Symposium on Test Methods and Measurements, Budapest,  
Hungary, April (1967).
6. Goetzberger, A., MacDonald, B., Haito, R. and  
Scarlett, R. M., J. Appl. Phys., 34, 1591 (1963).
7. Gilman, J. J. and Johnston, W. G., J. Appl. Phys.,  
31, 687 (1960).
8. Dash, W. C., J. Appl. Phys., 27, 1193 (1956).
9. Kear, B. H. and Pratt, P. L., Acta Metall., 6, 457  
(1958).
10. Indenbohm, V. L., Dokl. Akad. Nauk U.S.S.R., 141,  
1360 (1961), Fiz. Tverdogo Tela., 4, 231 (1962).
11. Hirsch. P. B., Horne, R. W. and Whelan, M. J.,  
Phil. Mag., 1, 677 (1956).
12. Bollmann, W., Phys. Rev., 103, 1588 (1956).

13. Barrett, C. S., Trans. AIME, 161, 15 (1945).
14. Newkirk, J. B., Trans. AIME, 215, 483 (1959).
15. Lang, A. R., Acta Cryst., 12, 249 (1959).
16. Lang, A. R., J. Appl. Phys., 30, 1748 (1959).
17. Kohra, K. and Yoshimatsu, M., J. Phys. Soc. Japan, 17, 1041 (1962).
18. Müller, E. W., J. Appl. Phys., 27, 474 (1956).
19. Müller, E. W., Z. Phys., 131, 136 (1951).
20. Müller, E. W., Z. Phys., 106, 541 (1937).
21. Hren, J. J. and Ranganathan, S., "Field-Ion Microscopy," Plenum Press, New York, New York (1968).
22. Cottrell, A. H., "Theoretical Structural Metallurgy," London, 2nd Edition, p. 231 (1955).
23. George, T. H., Zeit. für Phys., 176, 556 (1963).
24. Ranganathan, S., Bowkett, K. M., Hren, J. J. and Ralph, B., Phil. Mag., 12, 841 (1965).
25. Pashley, D. W., Rep. Prog. Phys., 28, 291 (1965).
26. Ranganathan, S., "Field-Ion Microscopy," edited by J. J. Hren and S. Ranganathan, Plenum Press, New York, New York, p. 120 (1968).
27. Smith, D. A., Fortes, M. A., Kelley, A. and Ralph, B., Phil. Mag., 17, 1065 (1968).
28. Frank, F. C., Phil. Mag., 42, 809 (1951).
29. Sanwald, R. C., Ranganathan, S. and Hren, J. J., Appl. Phys. Letters, 9, 393 (1966).
30. Moore, A. J. W., Phys. Chem. Solids, 23, 907 (1962).

31. Newman, R. W., Scripta Met., 2, 69 (1968).
32. Hren, J. J., Newman, R. W., Sanwald, R. C. and Son, U. T., Fourth Semiannual Report, NASA, Research Grant NGR 10-005-039, Sept. 1, 1967 - Feb. 29, 1968, University of Florida, Gainesville, Florida.
33. Müller, E. W., Adv. in Electronics and Electron Physics, 13, 83 (1960), (New York; Academic Press).
34. Rhodin, T. N., Palmberg, P. W. and Todd, C. J., J. Appl. Phys., 39, 4650 (1968).
35. Graham, W. R., Hutchinson, F., Nadakavukaren, J. J., Reed, D. A. and Schwenterly, S. W., J. Appl. Phys., 40, 3931 (1969).

B. THE EVOLUTION OF PARTICLE SIZE DISTRIBUTION FROM DATA ON THE LOW TEMPERATURE AGING OF ALUMINUM-ZINC ALLOYS (R. W. Gould)

Abstract

In this paper, a method is used by which the particle size distribution can be determined as a function of aging time from small-angle x-ray data on the low temperature aging ( $-45^{\circ}\text{C}$ ) of three aluminum-zinc alloys. A series of particle size distribution curves and particle diameter growth paths results from this analysis, and the evolution of the particle size distribution can be followed.

Introduction

During the past fifteen years, small-angle x-ray scattering and transmission electron microscopy have been used to study the growth of Guinier-Preston zones in metallic solid solutions. The aluminum-zinc system has been of particular interest as it contains spherical, zinc-rich Guinier-Preston zones which give rise to high mass contrast in the transmission electron microscope and which produce easily observable small-angle scattering effects. When small-angle scattering was first applied to this problem, one of three size parameters was generally used to characterize the growth

of the zones, Guinier radius, Porod or surface area "radius," and a radius determined from the position of the small-angle scattering intensity maximum. These single parameters were difficult to correlate with the transmission electron microscopy measurements which became available in the mid-1950s as shown clearly by Baur and Gerold.<sup>1</sup> Harkness, Gould and Hren,<sup>2</sup> in a recent publication have shown that the Guinier radius alone does not give a good measure of the mean zone radius. But when the Guinier radius and the Porod radius are both available, the combination of these two measurements enables the particle size distribution to be determined if the particles are spherical and a size distribution function can be assumed.

For the present study, the system aluminum-zinc was chosen and data was taken from a publication by Bonfiglioli and Guinier<sup>3</sup> in which the aluminum-zinc alloys were aged at  $-45^{\circ}\text{C}$  in order to study the very early stages of zone growth. Three alloys were examined by Bonfiglioli and Guinier, hereafter referred to as B and G,<sup>3</sup> i.e., 10, 20 and 30 wt. % zinc in solid solution in aluminum.

#### Analysis of Data

B and G studied the structure of the Guinier-Preston zones in the first stages of their formation, thus requiring the low temperature of aging. During the course of their investigation, they measured, as a function of aging time, several parameters characteristic of G.P. zone formation which are listed in Table I. Table I shows the time rate of change of the Guinier radius ( $R_G$ )<sup>†</sup> and the Porod radius ( $R_p$ ) as well as the integrated intensity  $Q(0)$ .

TABLE I

Zonal State Parameters of Three Al-Zn Alloys Aged at  $-45^{\circ}\text{C}$ .<sup>3</sup>

Alloy	Aging Time Minutes	$\beta$ Volume Fraction of Zones	$Q(0) = 2\pi \int_0^{\infty} sj(s)ds$ $\times 10^2$	$R_G$ ( $\text{\AA}$ )	$R_P$ ( $\text{\AA}$ )
Al-10 w/o Zn	10'	0.0318	2.07	6.34	5.40
	30		2.53	7.34	5.44
	90		3.19	9.48	6.33
	270		3.35	10.7	7.28
	810		3.58	11.5	7.30
	2430		3.69	11.5	7.26
Al-20 w/o Zn	0	0.0889	3.10	5.0	3.10
	10		6.50	13.6	7.58
	30		6.90	14.9	12.2
	90		8.35	15.0	11.8
	270		8.35	15.3	12.1
	810		8.72	15.4	13.9
	2430		8.57	16.4	15.2
Al-30 w/o Zn	10	0.135	10.65	14.6	9.62
	30		11.88	15.2	11.7
	90		11.75	16.1	14.1
	270		12.15	16.5	13.9
	810		12.10	16.3	13.9
	2430		11.90	16.1	14.2

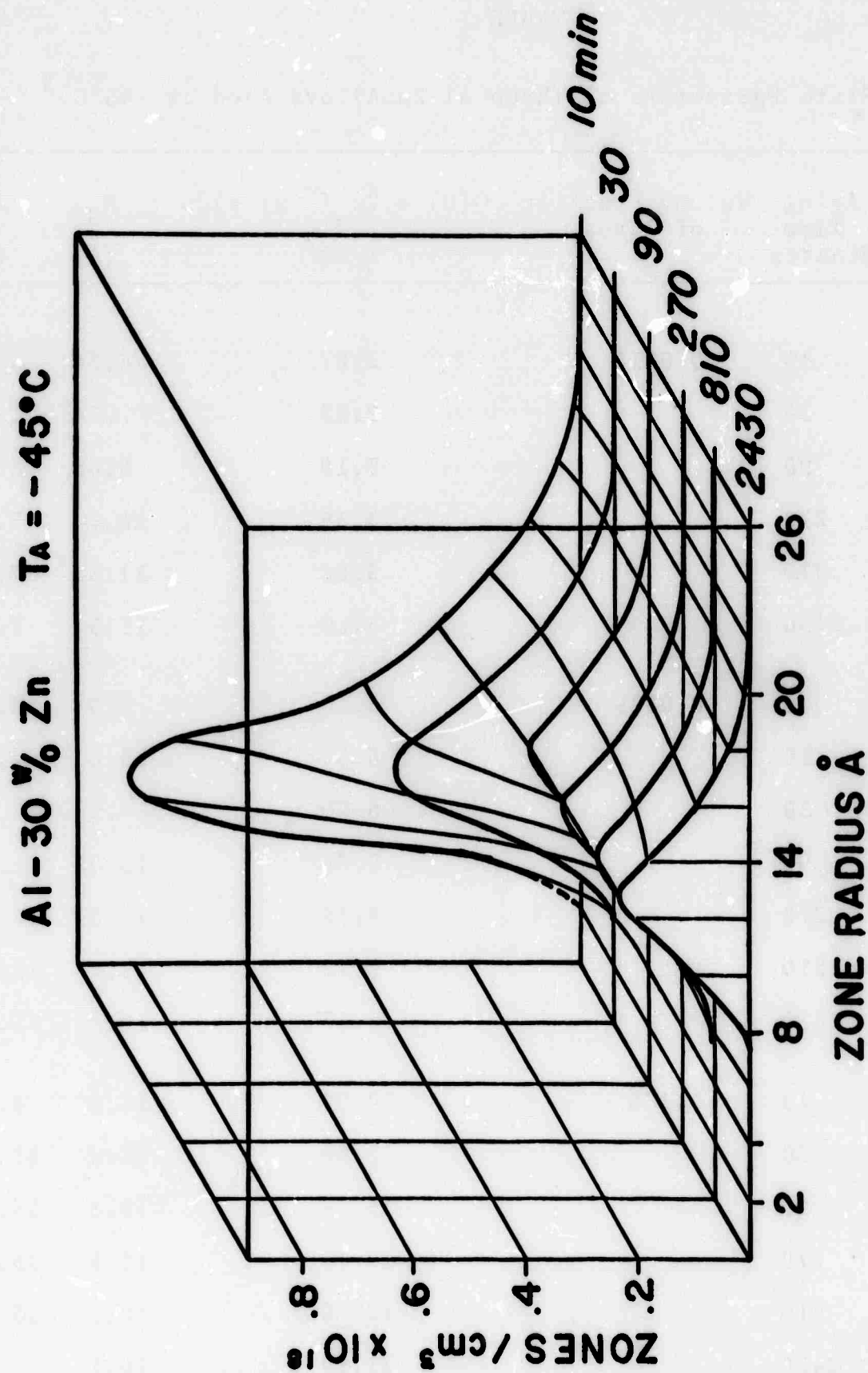


Fig. 1 Particle size distribution curves for Al-10% Zn after various aging times at  $-45^\circ\text{C}$ .

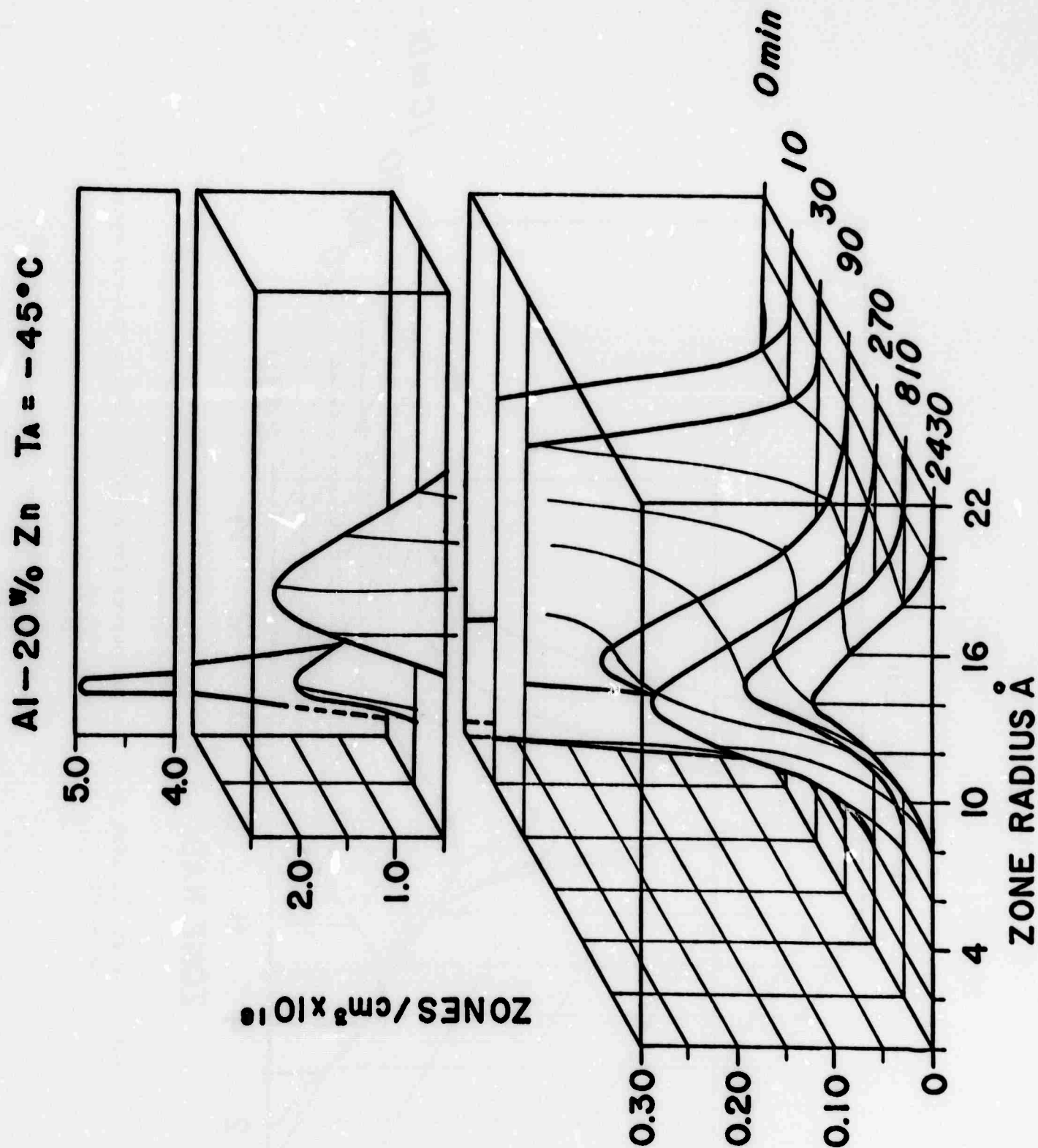


Fig. 2 Particle size distribution curves for Al-20% Zn after various aging times at  $-45^\circ\text{C}$ .



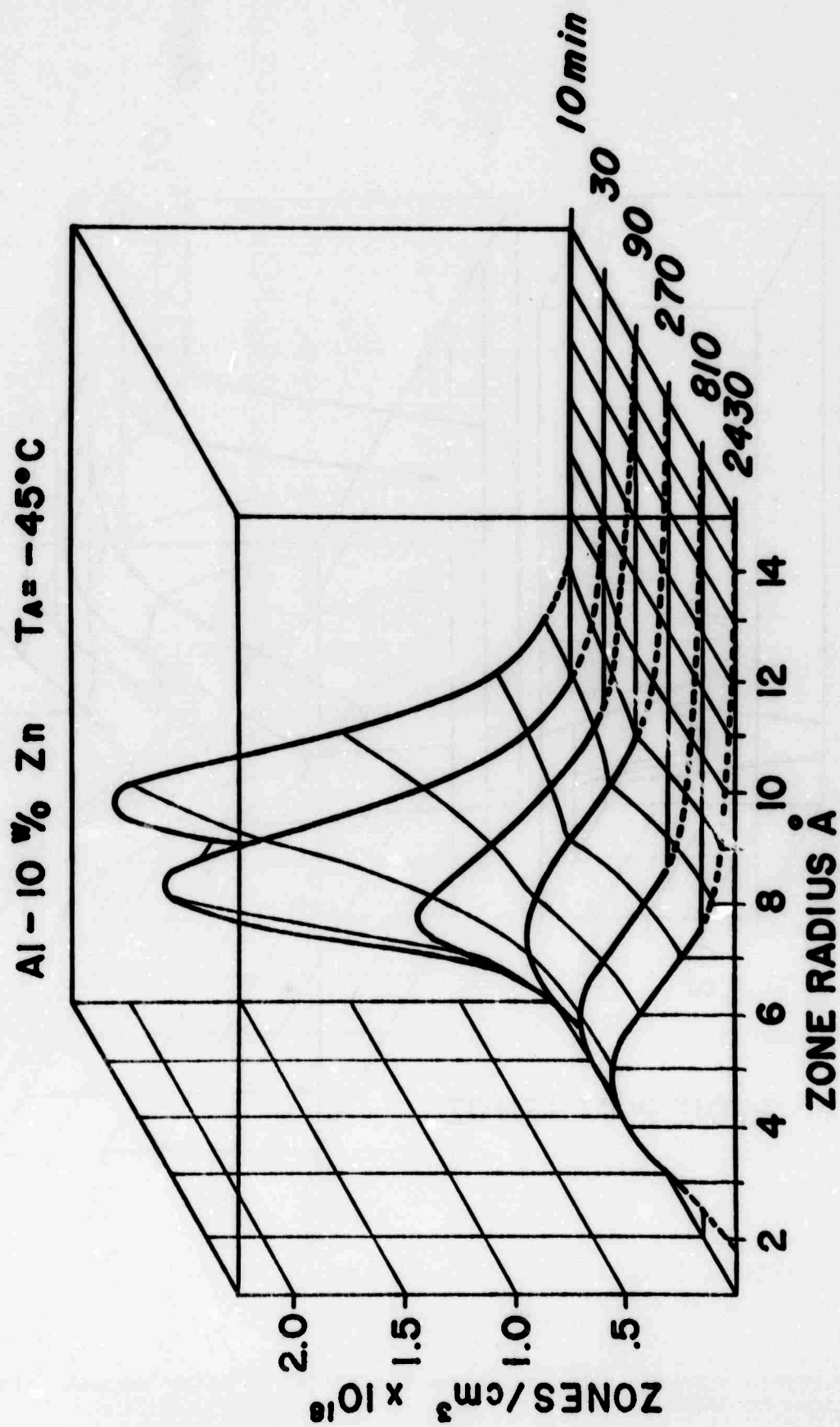


Fig. 3 Particle size distribution curves for Al-30% Zn after various aging times at  $-45^\circ\text{C}$ .

In order to measure the Porod radius it is considered good experimental<sup>3</sup> procedure to show that a plot of  $s^3 J(s)$  versus  $s^3$  results in a straight line of slope zero over a rather large angular range which includes the Porod region of the small-angle scattering curve. Such a straight line plot insures that the Porod law is valid, i.e., that there is a sharp interface between the zone and the surrounding matrix. B and G in their Figure 2 show that this situation does exist for all of the alloys with the single exception of the aluminum 30 wt. % zinc immediately after the quench. Porod radii taken from the Al-30% Zn in this condition, therefore, have not been included in the present analysis.

The volume fraction of segregated zones and the composition of the zones during the course of aging can be monitored by measuring the change in integrated small-angle scattering intensity. This measurement was also performed by B and G and they show that the total integrated intensity  $Q(0)$  does indeed change for all of the alloys up to 100 minutes or so after quenching. They explain, however, that this increase in  $Q(0)$  represents an increase in the percent of zinc in the zones and not an increase in the volume fraction of the zones. If their explanation is accepted, then the calculated volume fraction ( $\beta$ ) (see Table I) can be used from the

---

† Gerold (Physica Status Solidi 1, 37 1961) discusses and derives the, Guinier radius, the Porod radius and the integrated intensity. The Guinier particle radius is obtained from the slope of a plot of  $\log I$  versus  $s^2$  whereas the Porod radius is obtained from the outer or tail portion of the SAXS curve. The Porod radius is a surface area sensitive measurement.

early stages of decomposition to obtain the number of zones per unit volume in each size class "i" once the particle size distribution curve has been measured. The analysis of particle size distribution follows that given by Harkness and Gould in a recent publication.<sup>5</sup>

Utilizing the Guinier and Porod radii in Table I, particle size distributions were calculated at each aging time for each alloy. The results of such calculations are found in Figures 1-3. Visual observations of these figures indicates changes in the position of the size distribution maximum, which does not coincide with either the Guinier or Porod radius. In Figures 4-6, the total number of particles per unit volume, the mean zone radius and the change in the breadth (FWHM) of the particle size distribution are plotted as a function of aging time. In Figures 7 and 8, the growth paths of a particular size particle can be followed as a function of aging time. These curves will be analyzed in the discussion section which follows.

#### Determination of $N_v(R)$

The log normal size distribution<sup>2</sup> as given below:

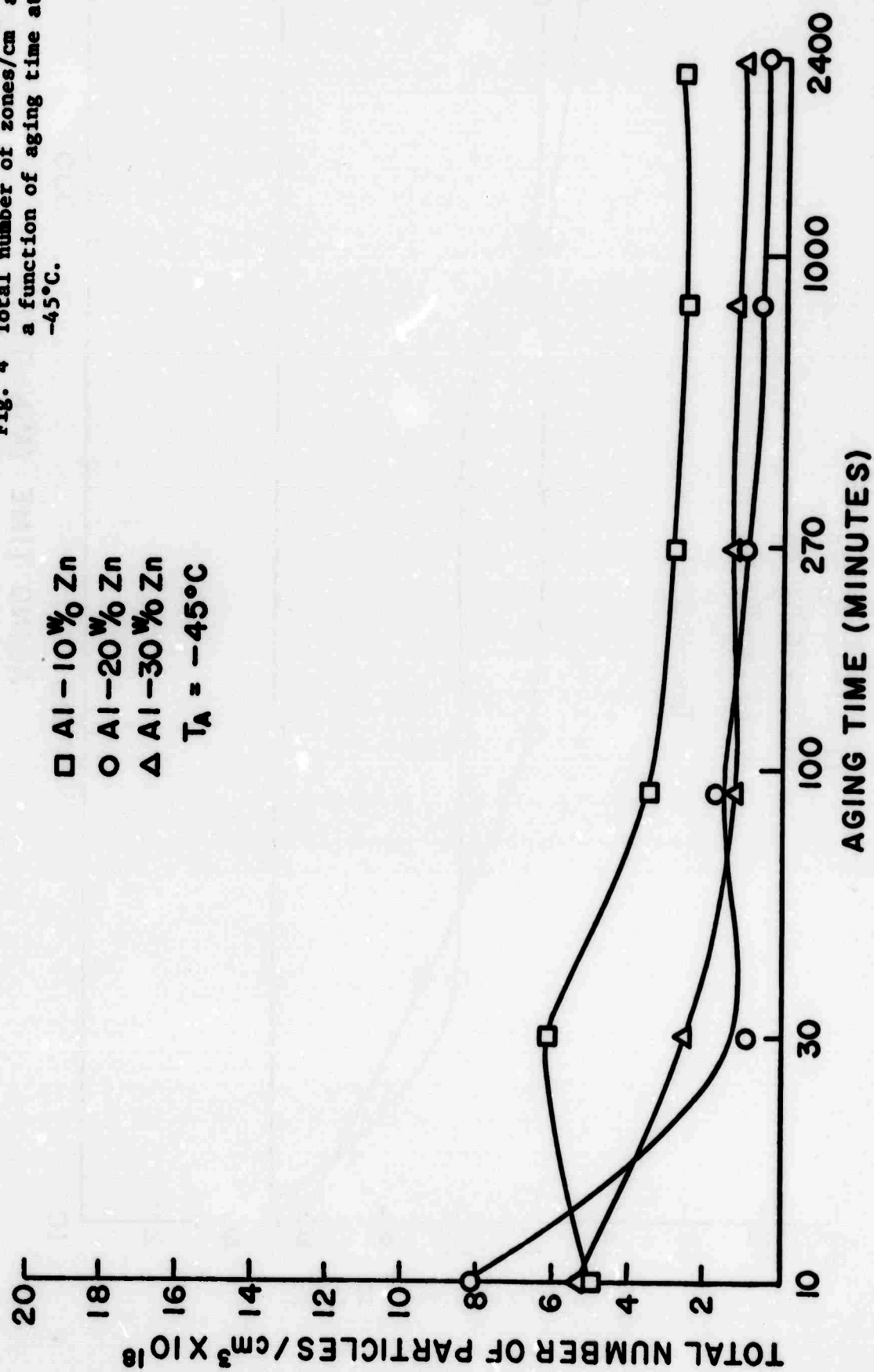
$$F(R) = \frac{1}{\sqrt{(2\pi)} R \ln \sigma} \exp - \frac{1}{2} \left[ \frac{\ln \mu - \ln R}{\ln \sigma} \right]^2$$

is completely characterized when  $\mu^\dagger$  and  $\sigma$  are known. It has been

---

<sup>†</sup>  $\ln \mu$  is the geometric mean and  $\ln^2 \sigma$  is the geometric variance of the log normal distribution

Fig. 4 Total number of zones/cm<sup>3</sup> as a function of aging time at -45°C.



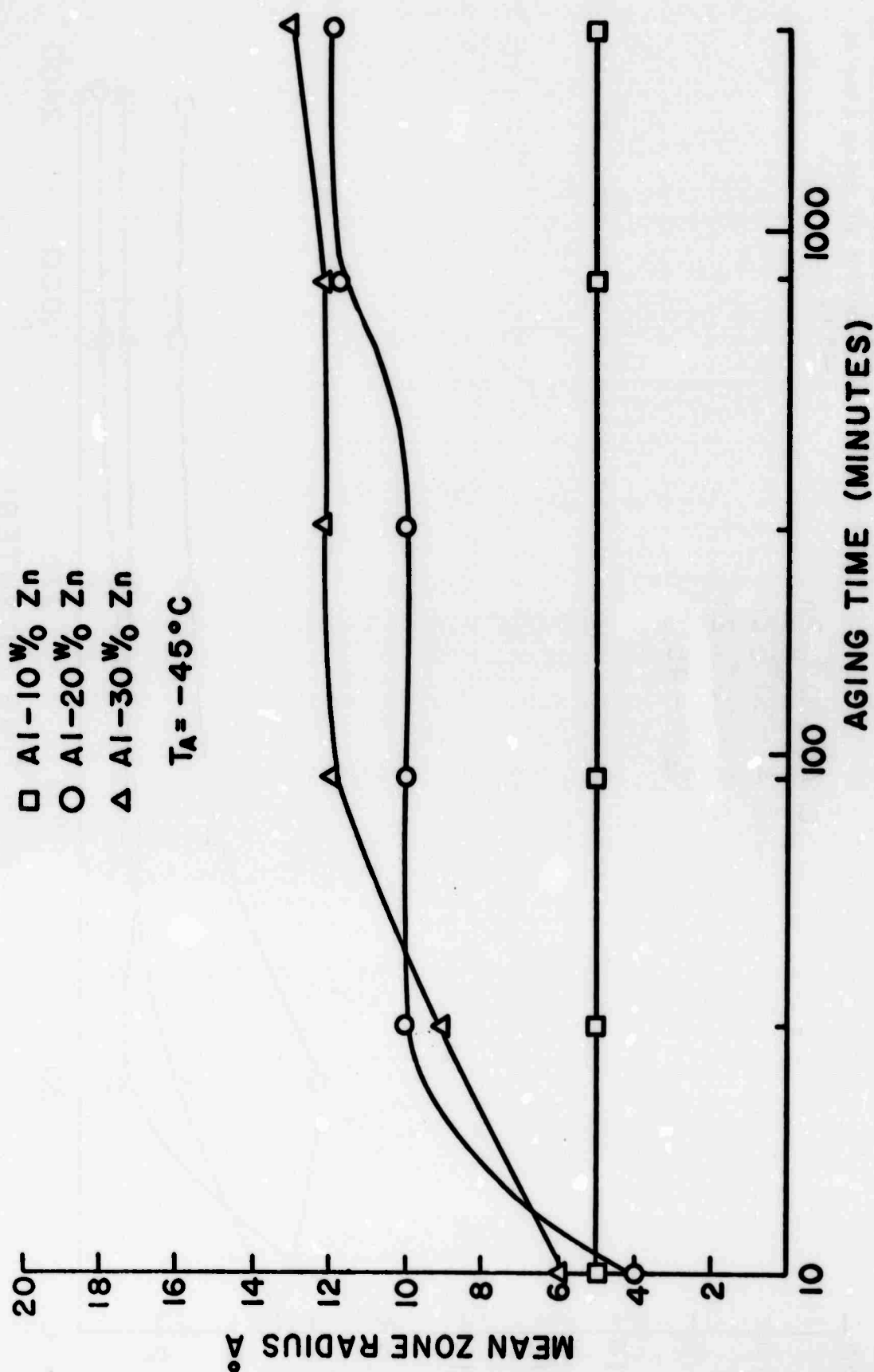
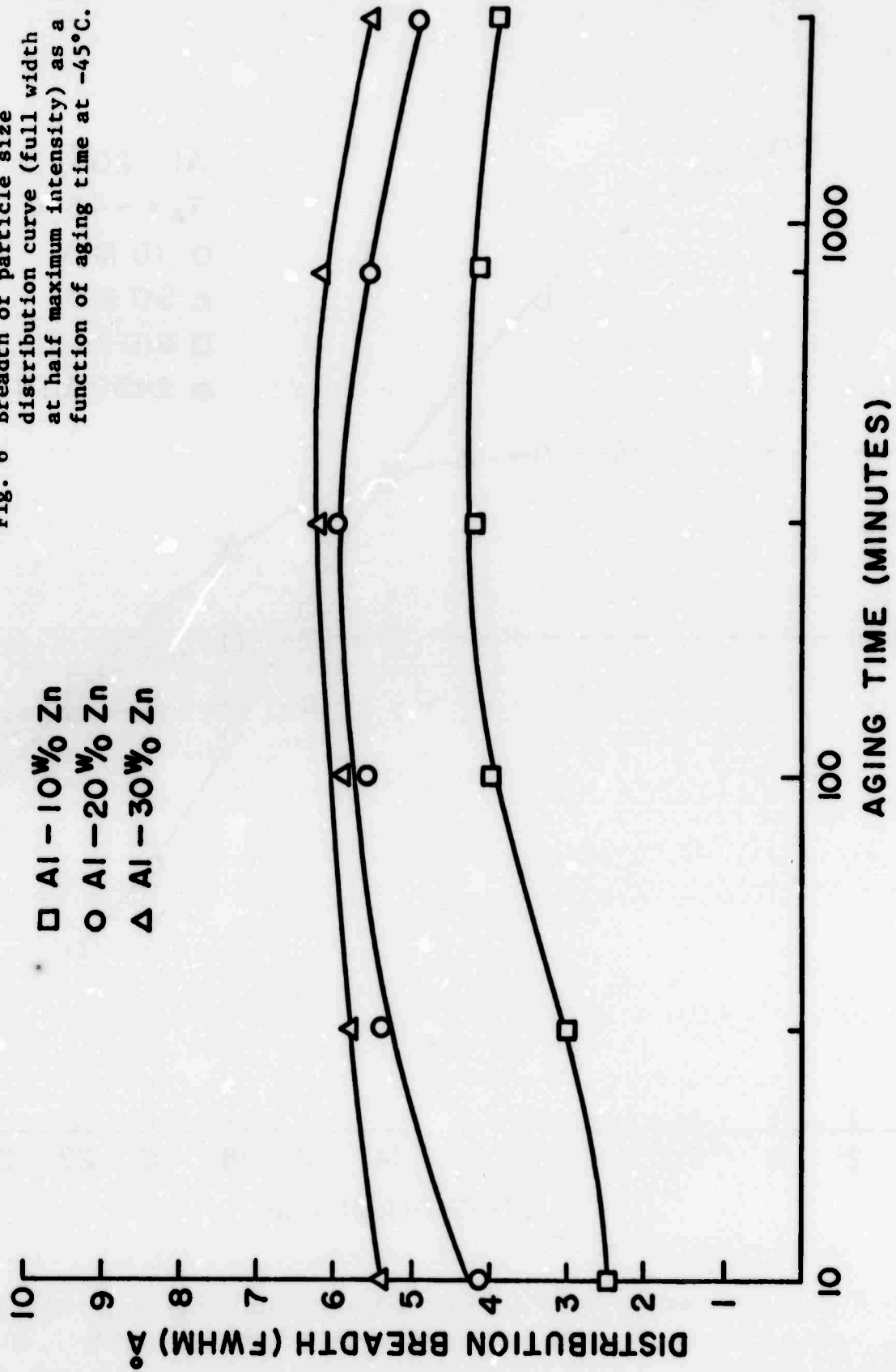


Fig. 5 Mean zone radius as a function of aging time at  $-45^\circ\text{C}$ .

Fig. 6 Breadth of particle size distribution curve (full width at half maximum intensity) as a function of aging time at  $-45^{\circ}\text{C}$ .



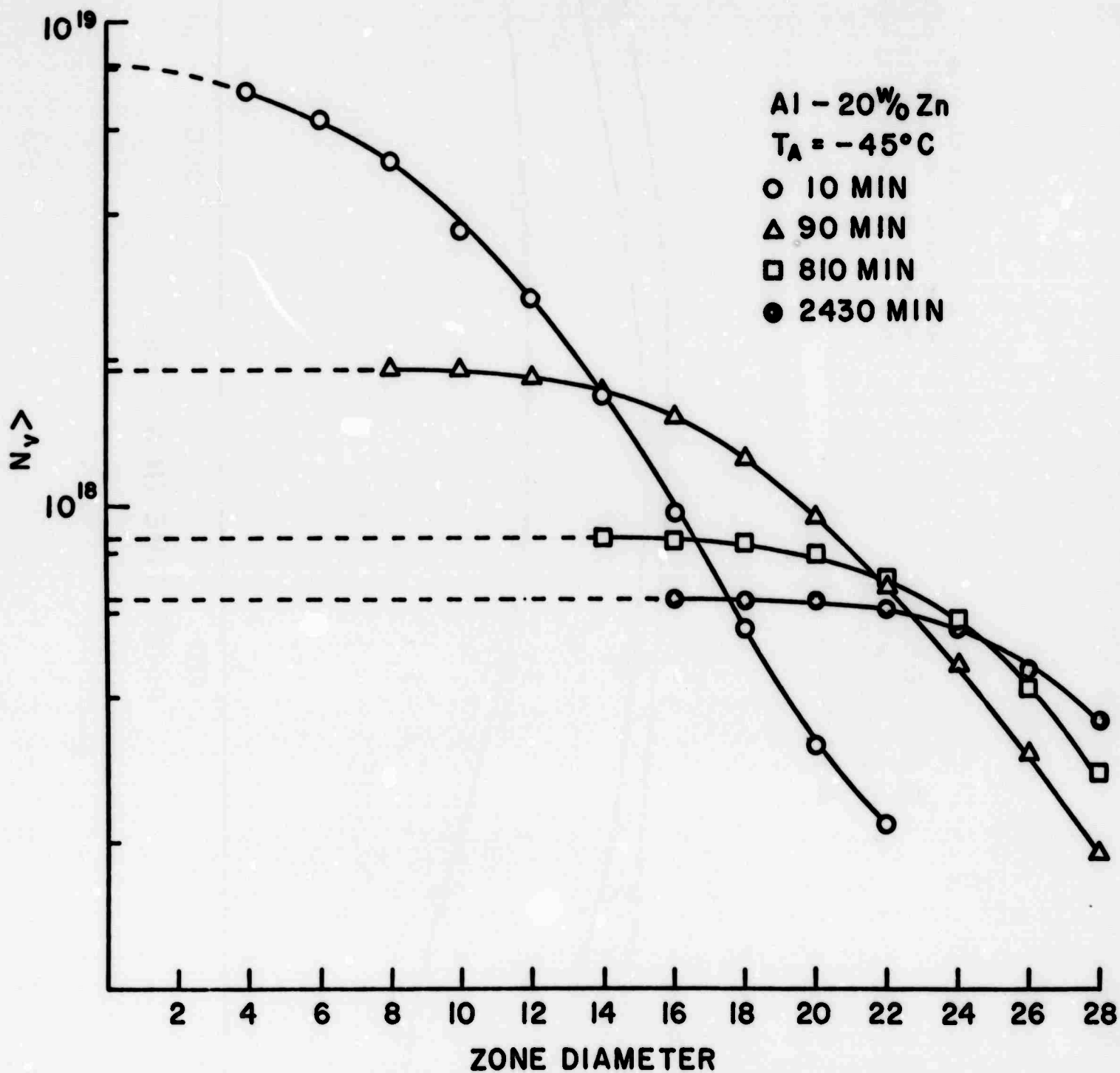
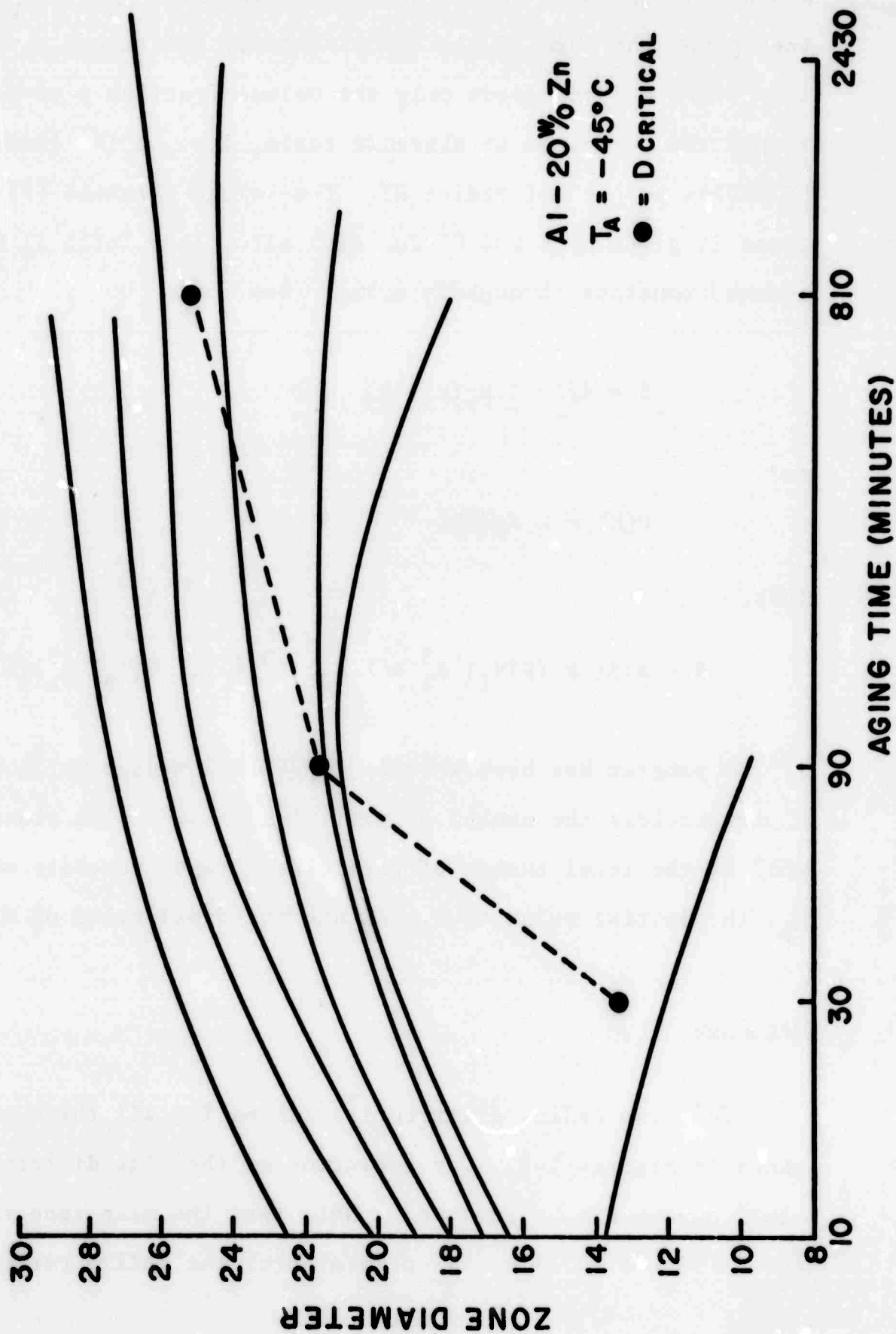


Fig. 7 The number of particles per unit volume greater than size  $i$  ( $N_v^>$ ) versus size  $i$  as a function of aging time for Al-20 x/o Zn aged at  $-45^\circ\text{C}$ .

Fig. 8 Particle growth curves  
for G.P. zones in Al-20 w/o  
Zn alloy aged at  $-45^{\circ}\text{C}$ .





shown<sup>2</sup> that  $\mu$  and  $\sigma$  may be written in terms of  $R_G$  and  $R_p$ .  $F(R)$  then gives the form of the experimentally determined size distribution curve and one needs only the volume fraction  $\beta$  of particles to put the curves on an absolute scale, i.e.,  $N_V(R)$  [number of particles per  $\text{cm}^3$  of radius  $R$ ]. The volume fraction ( $\beta$ ) of G.P. zones is given by  $B$  and  $G^3$  for each alloy (see Table I) and is assumed constant throughout aging. Now

$$\beta = 4/3\pi \sum_i N_V(R_i) R_i^3$$

and

$$F(R) = k N_V(R).$$

Thus,

$$\beta = 4/3\pi k \{F(R_1) R_1^3 + F(R_2) R_2^3 + \dots F(R_n) R_n^3\}.$$

A program has been written<sup>6</sup> in PL 1 language which calculates  $k$  and provides the number of particles in each size class  $R_i$  as well as the total number of particles. Input consists of  $\beta$ ,  $R_G$ ,  $R_p$ , the initial value of  $R_i$ ,  $\Delta R$  and the final value of  $R_i$ .

#### Discussion

The zone radius distribution curves for all three alloys are shown in Figures 1-3. The evolution of the size distribution at  $-45^\circ\text{C}$  can easily be followed. Note that the mean zone radius of the Al-10 w/o Zn alloy is constant over the entire period while the

curves for Al-20 w/o Zn and Al-30 w/o Zn alloy clearly indicate particle coarsening (Figure 5) and the total number of particles is decreasing as aging occurs (Figure 4). Thus the decrease in the total number of particles with aging time indicates that smaller zones are dissolving in favor of the growth of larger zones.

Note that the Al-10 w/o Zn alloy is undergoing a redistribution process, although this fact is not reflected in the change of mean zone radius with aging time as shown in Figure 5. The small maximum of the Al-10 w/o Zn curve in Figure 4 at approximately 30 minutes aging time would appear to indicate that this alloy may not have fully decomposed during the quench. The change in the breadth of the zone size distribution curve for each alloy as measured at half maximum intensity appears to pass through a weak maximum (Figure 6) indicating that the quenched state and the well aged state are more monodisperse than intermediate states of growth. The zero aging times were not included in this figure as the validity of the Porod radius may be questioned for this initial state. However, the Al-20 w/o Zn alloy appears to have a sharp zone-matrix interface even immediately after the quench. The FWHM breadth of this curve can be measured from Figure 2 to be approximately  $1.5 \text{ \AA}$ , indicating a very monodisperse initial zone state.

If the zone radius distribution curves are available, one is able to calculate the growth paths of various sized zones. This method has been illustrated by Harkness and Gould<sup>5</sup> for Al-Ag and Al-Zn alloys and the reader is referred to that paper for details.  $N_v > \dagger$  curves can be obtained from the particle size distribution

---

$\dagger N_v >$  curves plot the number of zones larger than a particular zone size versus that size.

data if the volume fraction of particles is known. A typical  $N_v$  curve for the Al-20 w/o An alloy is reproduced in Figure 7. The resulting growth path curves are shown in Figure 8. As anticipated, the critical zone diameter,  $D_{critical}$ , tends to increase with increasing aging time.

### Summary

A method for obtaining particle size distribution curves from SAXS data has been applied to G.P. zones in the Al-Zn system aged at  $-45^{\circ}\text{C}$ . A series of G.P. zone diameter distribution curves have been derived using Guinier and Porod radii measured by Bonfiglioli and Guinier.<sup>3</sup> These curves were then analyzed and the low temperature G.P. zone growth behavior can be described as a typical particle coarsening process with competitive growth. It appears that the zonal state immediately after the quench is characterized by a more monodisperse zone size distribution than at later aging times.

## REFERENCES

1. R. Baur and V. Gerold, Acta Met., 12 (1964) 1448.
2. S. D. Harkness, R. W. Gould, and J. J. Hren, Phil. Mag., 19 (1969) 113.
3. A. Bonfiglioli and A. Guinier, Acta Met., 14 (1966) 1213.
4. R. W. Gould, English Translation of Reference 3.
5. S. D. Harkness and R. W. Gould, Advances in X-Ray Analysis, Vol. 12, p. 97.
6. R. W. Gould and P. Mehl, Particle Distribution Analysis Computer Program, Department of Metallurgy, University of Florida.

## V. Magnetic Materials (J. K. Watson)

### A. ANALOG APPROXIMATIONS OF TRANSIENT FLUX DIFFUSION (J. K. Watson and C. T. Leis<sup>\*</sup>)

#### Introduction

The trapped flux interaction between magnetic films and nearby electrical conductors is a well-known phenomenon experimentally<sup>1-5</sup>, and has been used as the basic mechanism of NDRO memories<sup>3,5</sup>. However, a theoretical understanding of this process has been difficult. Previous analyses<sup>4,5</sup> are formidable enough computationally and conceptually to limit their usefulness. The new approach<sup>6</sup> presented here has a surprisingly simple form and leads to results that agree well with more complicated methods<sup>5</sup>. Our approximations and assumptions are indicated in detail, since this analog method is thought to be applicable to other magnetic diffusion problems.

The underlying mechanism stems from Maxwell's equations which require that changes of flux density  $\bar{B}$  within a non-magnetic conductor must satisfy the diffusion equation

$$\nabla^2 \bar{B} = \mu_0 \sigma \partial \bar{B} / \partial t \quad (1)$$

where  $\mu_0$  is the permeability of space and  $\sigma$  is the conductivity of the material. In the geometry of interest here,  $B$  is a complicated spatial function which is not easily represented in closed form, even in the static case where it defines the stray field from the film.

<sup>\*</sup>C. T. Leis is now with the Hewlett-Packard Co., Cupertino, California.

When a film is switched, or remagnetized to another orientation, the stray field must also be reoriented. The transient interaction exists while the old field collapses and the new field builds up. The major objective of this paper is to provide a basis for estimating the magnitude and time duration of the transient, taking into account the geometry of the film, insulators, and conductors.

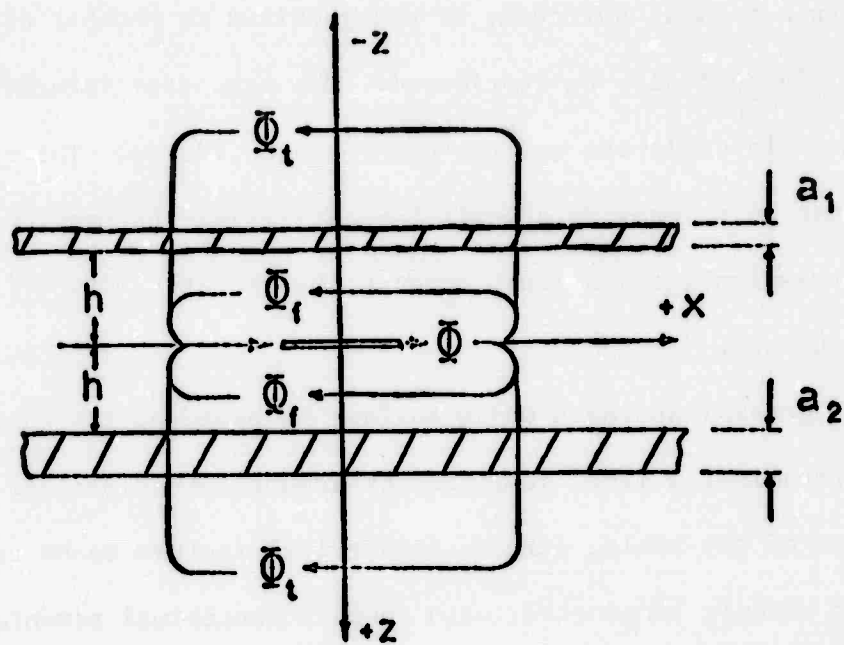
The general approach which follows is based on the analogy to (1) of an RC transmission line, justified by assumptions described below. Subsequent use of the analog permits geometrical factors to be represented as electric circuit components, with certain conceptual advantages that will be evident.

#### System Model

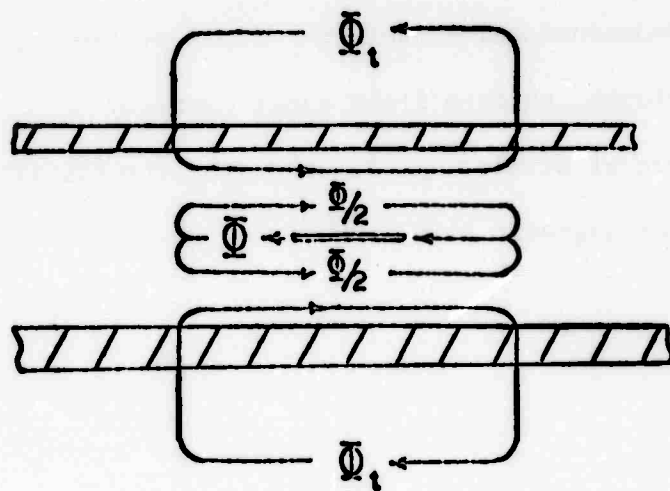
In this section we consider those assumptions which lead to the representation of the 3-dimensional nonuniform field problem by a conceptually simpler one-dimensional, uniform field approximation.

For convenience of developing the concepts, the geometry of Fig. 1(a) is assumed in which the magnetic film is halfway between two conducting plates of a stripline.

The total stray flux,  $\phi$ , emanating from the film has a free component,  $\phi_f$ , and a trapped component,  $\phi_t$ , where the latter penetrates the conductors in the static situation. Immediately after an instantaneous reversal of film magnetization, Fig. 1(b),  $\phi_t$  still retains its original orientation within the conductors. However the total flux  $\phi$  is temporarily squeezed between the striplines in the new orientation, along with the return from the trapped flux,



(a)



(b)

Fig. 1. Geometrical notation, and flux patterns around thin film. (a) Before switching. (b) After switching.

because of the relatively slow diffusion.

We consider the flux density in the vicinity of the z-axis, just above and below the film which is in the x-y plane. Here the flux is parallel to the plane of the film and conductors. The flux density along the z-axis has only an x-component, which is, however, a function of z and time. Hence the problem of interest is reduced to one spatial dimension. For a circular film of radius r, thickness  $\delta$ , and saturation magnetization M, the static flux density along the z-axis is given by

$$B(z) = \frac{\delta r^2 M}{4(r^2 + z^2)^{3/2}} \quad (2)$$

Interestingly, it is not necessary to find a diffusion process which approaches (2) as a final value. Instead, we shall use a surprisingly simple, rectangular approximation to (2), based on the key concept that the total stray flux and the trapped fraction of flux are the pertinent quantities of the diffusion process. Using the geometry of Fig. 1, with insulators near the film for  $|z| < h$  and conductors for  $|z| > h$ , the free flux is defined in terms of its average value  $B_a$  as

$$\phi_f = 2h B_a = \int_{-h}^h B(z) dz = 2h Q(r^2 + h^2)^{-1/2}$$

where  $Q = \delta M/4$ . Choosing the rectangular approximation of Fig. 2, of value  $B_a$  inside the conductor and out, gives rise to the concept of "effective penetration depth" d.

Thus the trapped flux is

$$\phi_t = 2 \int_h^\infty B(z) dz = 2d B_a$$

where  $d = \sqrt{r^2 + h^2} - h$ . In the transmission line analogy to be developed subsequently, d will be a useful measure for defining the effective termi-



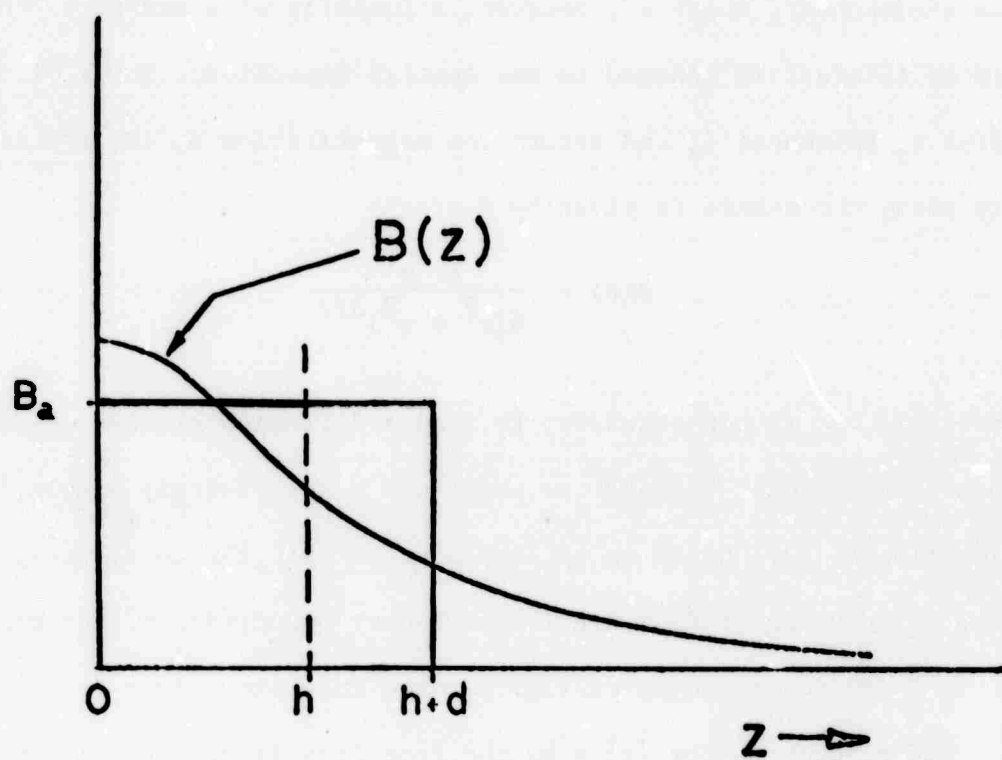


Fig. 2.  $B(z)$  and its rectangular approximation.

nation impedance for the lines. The important role of the conductor separation  $2h$  can be discerned from the equation for parameter  $d$ .

The original problem has now been reduced to a much simplified form. The assumed flux patterns are illustrated in Fig. 3.

Before switching, the flux density along the  $z$ -axis is zero except for a constant value of  $-B_a$  from  $-(h + d) < z < (h + d)$ .

Just after a fast rotation of  $\bar{M}$  the entire flux from the film plus the closing path of the trapped flux is squeezed between the plates. The new value of flux density in the region is then

$$B_s = \frac{1}{h}(\frac{\phi}{2} + \phi_t) = B_a(h + 2d)/h. \quad (3)$$

As time progresses, flux from the space between the plates diffuses into and through the conductors until equilibrium is reached in the opposite direction. At all times the total flux

$$\phi = \int_{-\infty}^{\infty} B(z) dz = 2B_a(h + d) \quad (4)$$

must stay constant.

The model for the physical system is now complete. Of particular interest are the two components of flux between the plates during the diffusion process. They represent the mechanism of the interaction torque between film and strip-line.

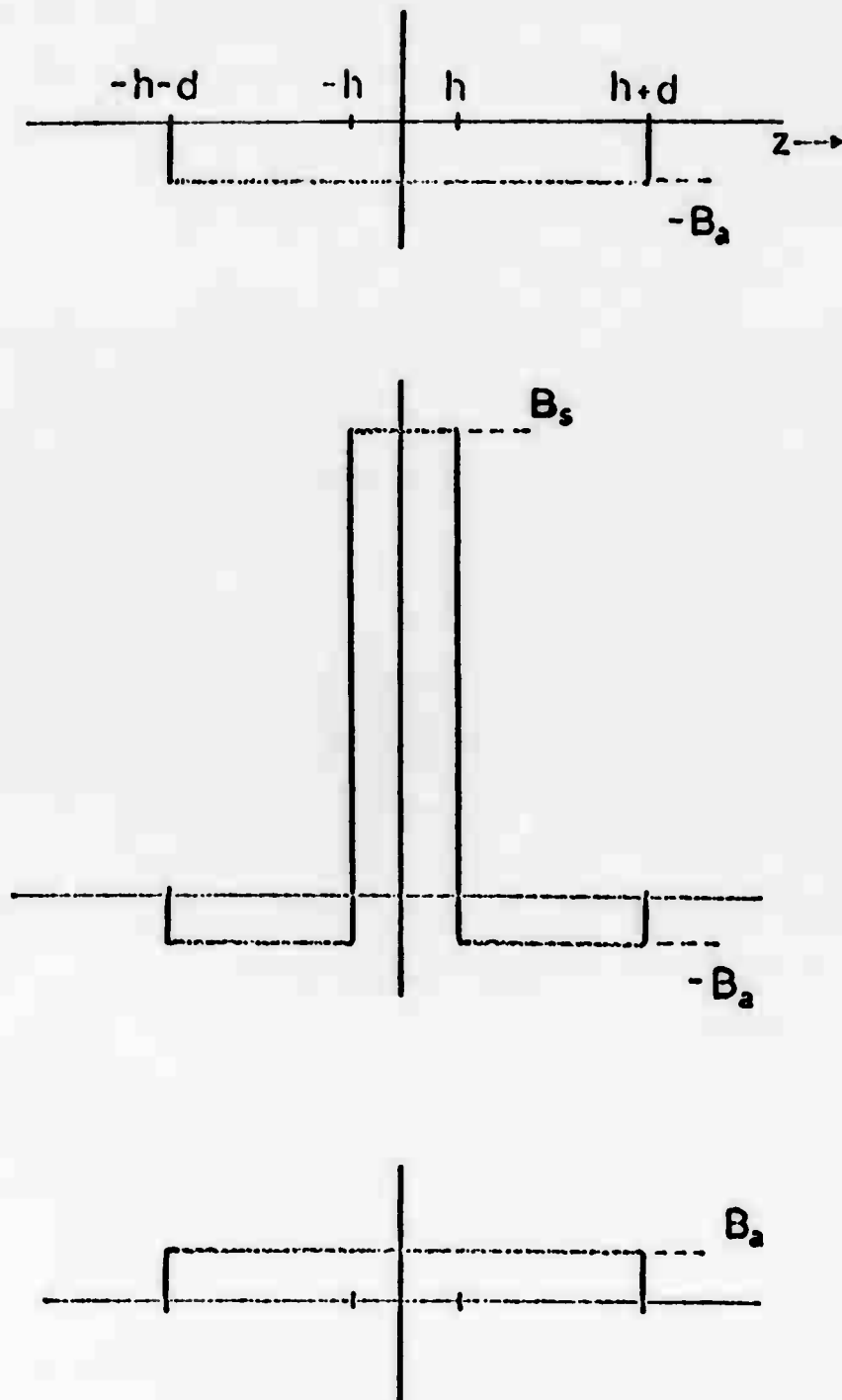


Fig. 3. The assumed  $z$ -axis flux density distributions. (a) Before switching. (b) Immediately after "fast" switching. (c) After diffusion.

### Electric Analog

The assumptions cited above permit the diffusion equation to be reduced to one dimension along the z-axis, thereby providing access to solutions which are available<sup>7</sup>. For our purposes it is instructive to consider the analogous RC transmission line equation

$$D \frac{\partial^2 B}{\partial z^2} = \frac{\partial B}{\partial t} \quad \text{analogous to} \quad \frac{\partial^2 V}{\partial z^2} = RC \frac{\partial V}{\partial t}$$

where diffusivity  $D = 1/\mu_0 \sigma$ . In this comparison flux is analogous to electric charge as the diffusing quantity. Outlined in the appendix and illustrated in Fig. 4, the linear dimensions along the z-axis are analogous to circuit elements for y-dimensions normalized to unity.

In this figure, the central capacitor  $C_0$  corresponds to the space between the plates so its value is the z-dimension  $2h$ . As shown, each stripline plate is represented by RC transmission line of length  $a_1$  and each is terminated by a capacitor  $C_1 = d - a_1$  which represents the amount of free space beyond the conductor available for flux distribution. If the conductor thickness is greater than  $d$ , the transmission line will be an open-circuited line of length  $d$ .

We will be concerned with finding  $V(t)$ , the voltage across  $C_0$ , which is equivalent to finding the flux density between the conductors as a function of time. As suggested by Fig. 3, the initial conditions after an instantaneous film reversal would place a positive voltage  $B_0$  on  $C_0$ , and a voltage  $-B_0$  on all the other capacitors. At time  $t = 0$  the system will be released and current will flow until equilibrium is reached.

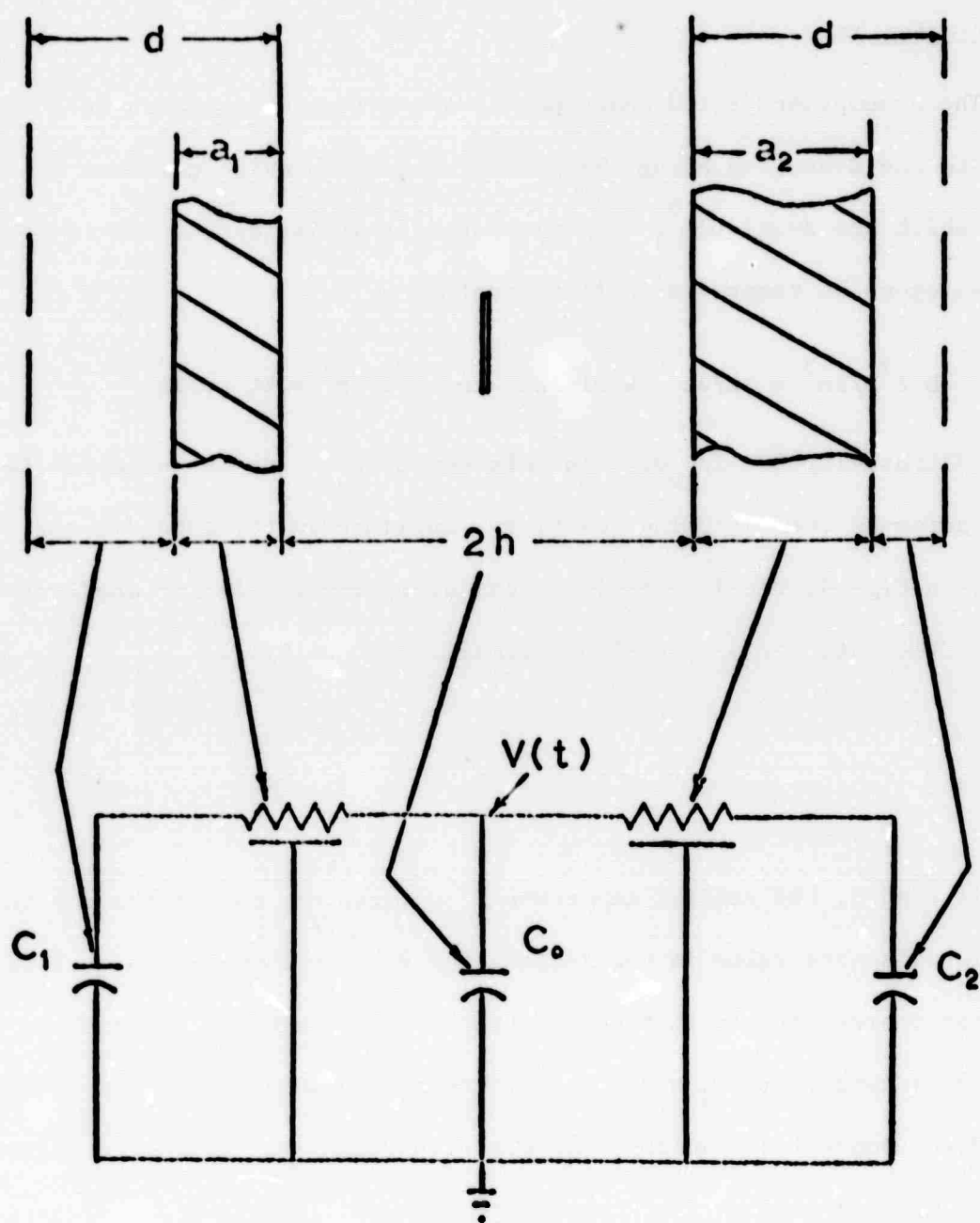


Fig. 4. The electrical analog.  $C_0 = 2h$ ,  $C_1 = d - a_1$ , and  $C_2 = d - a_2$ .

Conventional circuit analysis techniques, including lumped approximations to distributed lines, can now be brought to bear on the problem. Results from two special cases are considered, to illustrate the principle of finding the input impedance which is connected to  $C_0$ . The feasibility will be evident of extending the technique to other geometry.

Case 1,  $a \ll d$

When the conductors are very thin, the capacitance of the RC line can be neglected with little loss of accuracy with the result shown in Fig. 5. Each resistor has the value  $a/D$ , from the appendix, and the capacitor has the value  $d - a \approx d$ . Thus the input impedance is

$$Z(s) = a/D + 1/ds$$

Case 2,  $d \leq a$

When the conductors are very thick, the electric circuit consists of an open circuited RC line of length  $d$  connected on each side of  $C_0$ . The input impedance for such a line is

$$Z(s) = \frac{1}{\sqrt{Ds}} \coth \left( d \frac{\sqrt{s}}{\sqrt{D}} \right)$$

as noted in the appendix.

It is sometimes useful to consider a lumped approximation to the RC line, for a circuit model in the same form as Fig. 5. Using the two lowest-order terms of the series expansion<sup>8</sup> about zero of  $\coth$ , which is equivalent to a low-frequency model<sup>6</sup> for  $Z$ , the result is

$$Z(s) \approx \frac{d}{3D} + \frac{1}{ds}$$

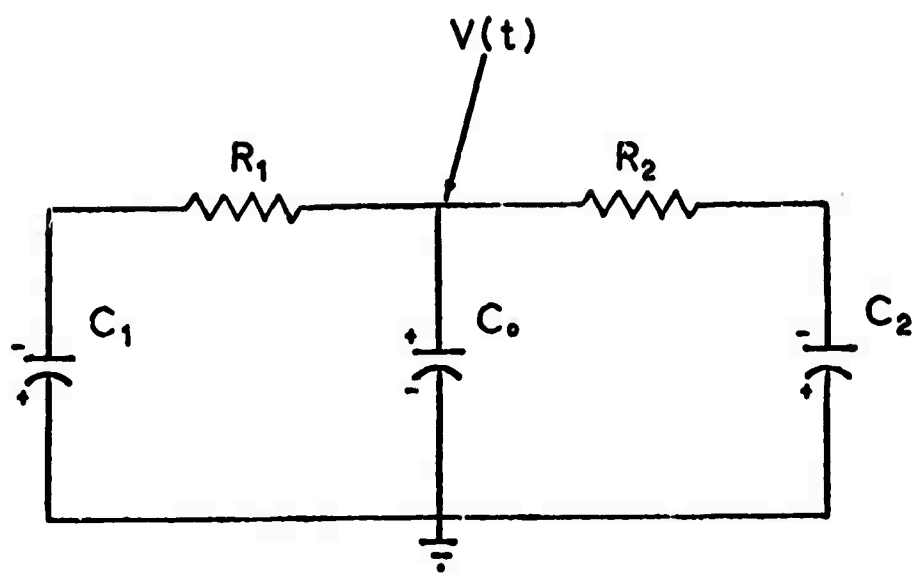


**Fig. 5.** Complete analog circuit incorporating approximations for very thick or very thin strip-line plates.

### System Solutions

We now indicate transient solutions to the analogous circuits which were developed in the previous section, using the approximation of Fig. 5. We consider three cases: both stripline conductors are very thin, both conductors are very thick, and one is thick and the other is thin. In each case the fact that  $C_1$  and  $C_2$  have identical initial conditions stems from the assumption that the film is located midway between the conductors. Using conventional circuit analysis techniques, the transform of the voltage is

$$V(s) = \frac{B_s + B_a}{s} \left[ \frac{Z_t}{\frac{1}{C_0 s} + Z_t} \right] - \frac{B_a}{s}$$

where  $Z_t$  is the parallel combination of  $Z_1$  and  $Z_2$ . If both conductors have the same thickness, the final result is

$$B(t) = B_a + [B_s - B_a] e^{-t/\tau}$$

after replacing the electrical symbols by their physical counterparts. In that equation  $B_s$  is given by (3) as before. The value of time-constant  $\tau$  ranges from  $\tau = ah'/D$  for very thin conductors to approximately  $\tau = dh'/3D$  for very thick conductors, where  $\mu_0 \sigma = 1/D$  as before,  $h' = dh/d + h = h/1 + \lambda$ , where  $\lambda$  is the ratio of free to trapped flux.

A particularly interesting geometry consists of one thin conductor above the film and a thick conducting ground plane below. The circuit of Fig. 5 is then solved for  $V(t)$  when  $R_1 \ll R_2$ . Two important time constants result

$$\tau_1 = R_1 K_1 \text{ with } K_1 \text{ given by } C_0 \text{ in series with } C_1,$$

$$\text{and } \tau_2 = R_2 K_2 \text{ given by } C_2 \text{ in series with } C_0 + C_1.$$

The physical interpretation is that the flux diffuses rapidly through the thin plate until a temporary equilibrium is reached. Then the slow diffusion into the ground plane takes place. To find the intermediate value of flux



density  $B_i$  it is assumed that the diffusion into the thick conductor is negligible during the fast mode. Using a sketch of the above statement, and the principle that total flux (4) must remain constant, it follows that

$$B_i = B_a \frac{(3 + 2\lambda)}{(1 + 2\lambda)} .$$

The complete estimate of the time response of flux density between the conductors is

$$B(t) = B_a + [B_s - B_i] e^{-t/\tau_1} + [B_i - B_a] e^{-t/\tau_2} \quad (5)$$

where the two terms on the right are due to the influence of eddy currents.

The form of the eddy current component is the same as an empirical result<sup>9</sup>.

In physical units the two dominant time constants are  $\tau_1 = \frac{2ah}{D(1 + 2\lambda)}$  and  $\tau_2 = \frac{d^2(1 + 2\lambda)}{6D(1 + \lambda)}$  where  $a$  is the thickness of the top conductor. Fig. 6 shows a sketch of (5), which we now examine in greater detail.

### Comparison of Results

In an attempt to establish a measure of the validity of (5) and its associated time constants, a comparison was made with some results of Jutzi<sup>5</sup>. Using a complicated numerical procedure, he obtained solutions for the magnetic field intensity  $H = B/\mu_0$  between the conductors as a function of time after an instantaneous change in the magnetization vector from a value of zero to  $1 \text{ W/m}^2$ . His procedure differs from the above analysis in having no trapped

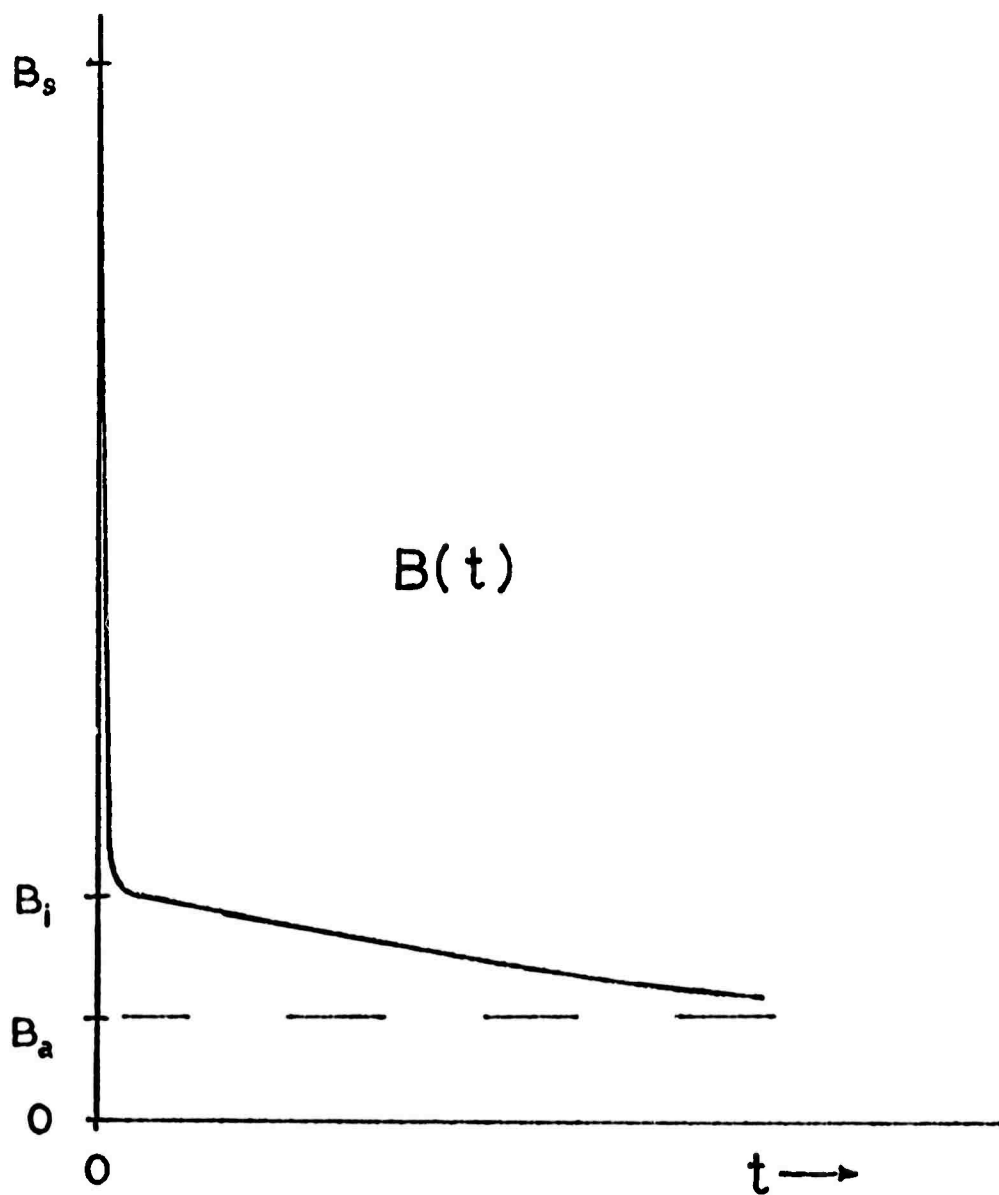


Fig. 6 Estimation of the time response of flux density between the conductors (one thin plate, the other thick).

flux in the initial condition, thus the initial ( $B_s$ ) and the intermediate ( $B_1$ ) values of flux density need to be adjusted. The time constants remain unaffected since they depend solely on the geometry. The physical dimensions in the comparison are:  $\delta = .07 \mu$ ,  $r = 200 \mu$ ,  $h = 2.5 \mu$ , and  $a = 2.5 \mu$ . The ratio of  $h/r$  implies  $\lambda = 0$  and  $d = 200 \mu$ . The resulting time constants are  $\tau_1 = 0.915 \text{ ns}$  and  $\tau_2 = 487 \text{ ns}$ . After omitting the trapped flux, the field intensities are computed to be  $H_a = B_a/\mu_0 = 70 \text{ A/m}$ ;  $H_1 = 140 \text{ A/m}$ ;  $H_s = 5600 \text{ A/m}$ .

The fast portion and the slow portion of the transient are compared separately with Jutzi's calculated results in Figs. 7 and 8, respectively, and the agreement is good. It is concluded that (5) is an adequate representation of the physical situation.

### Conclusion

This paper has sought to establish an approximation method for flux diffusion, then to apply it to the computation of parameters which are of considerable practical interest. These objectives motivated our attempt to carefully define the assumptions and approximations of the system model. The approach is attractive because of the simplicity of the results, the ease with which the geometry is considered, and certain conceptual advantages which are gained from the analog representation of the problem. The circuit analog is

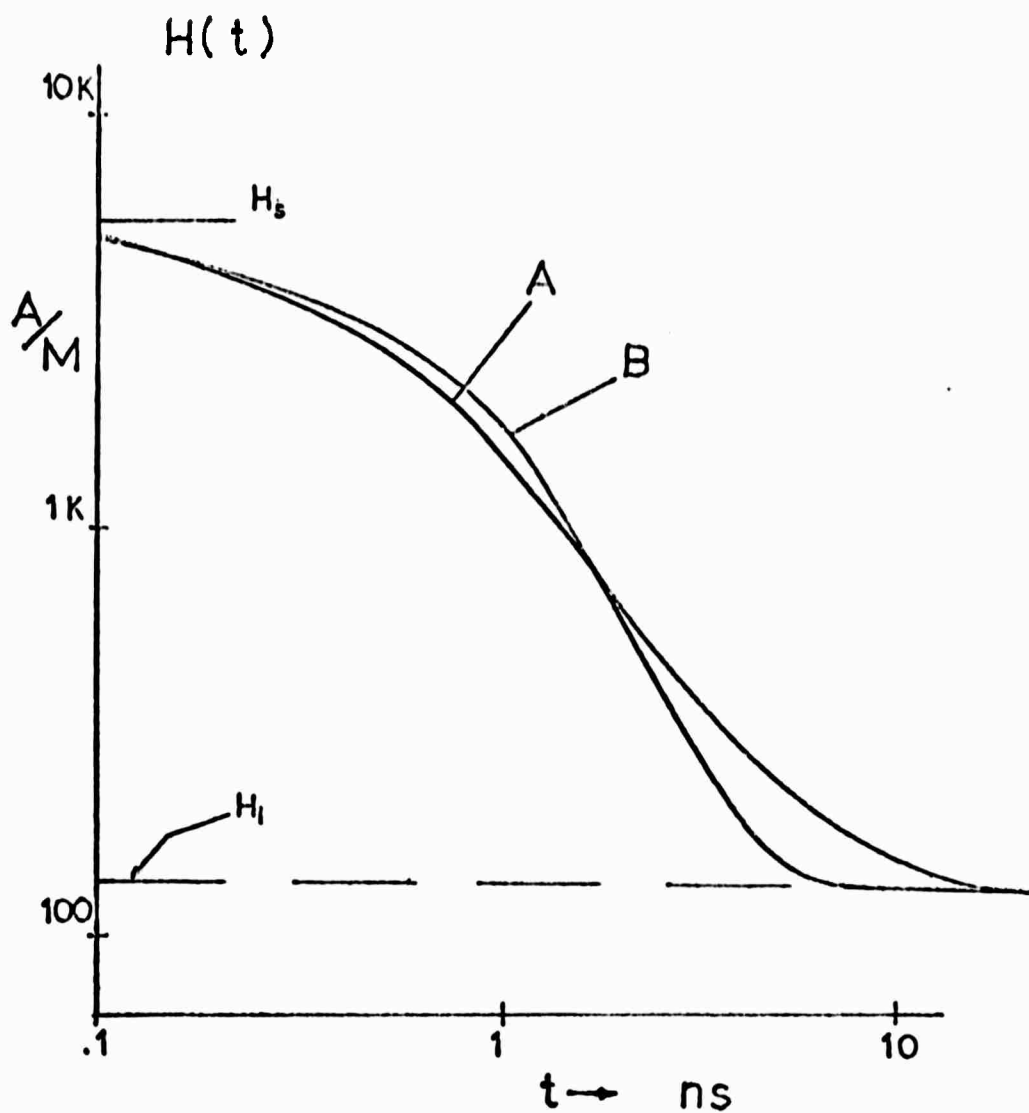


Fig. 7 Fast decay mode comparison. Jutzi's computation, A, and the estimation, B, with time constant  $\tau_1 = .915 \text{ ns}$ .

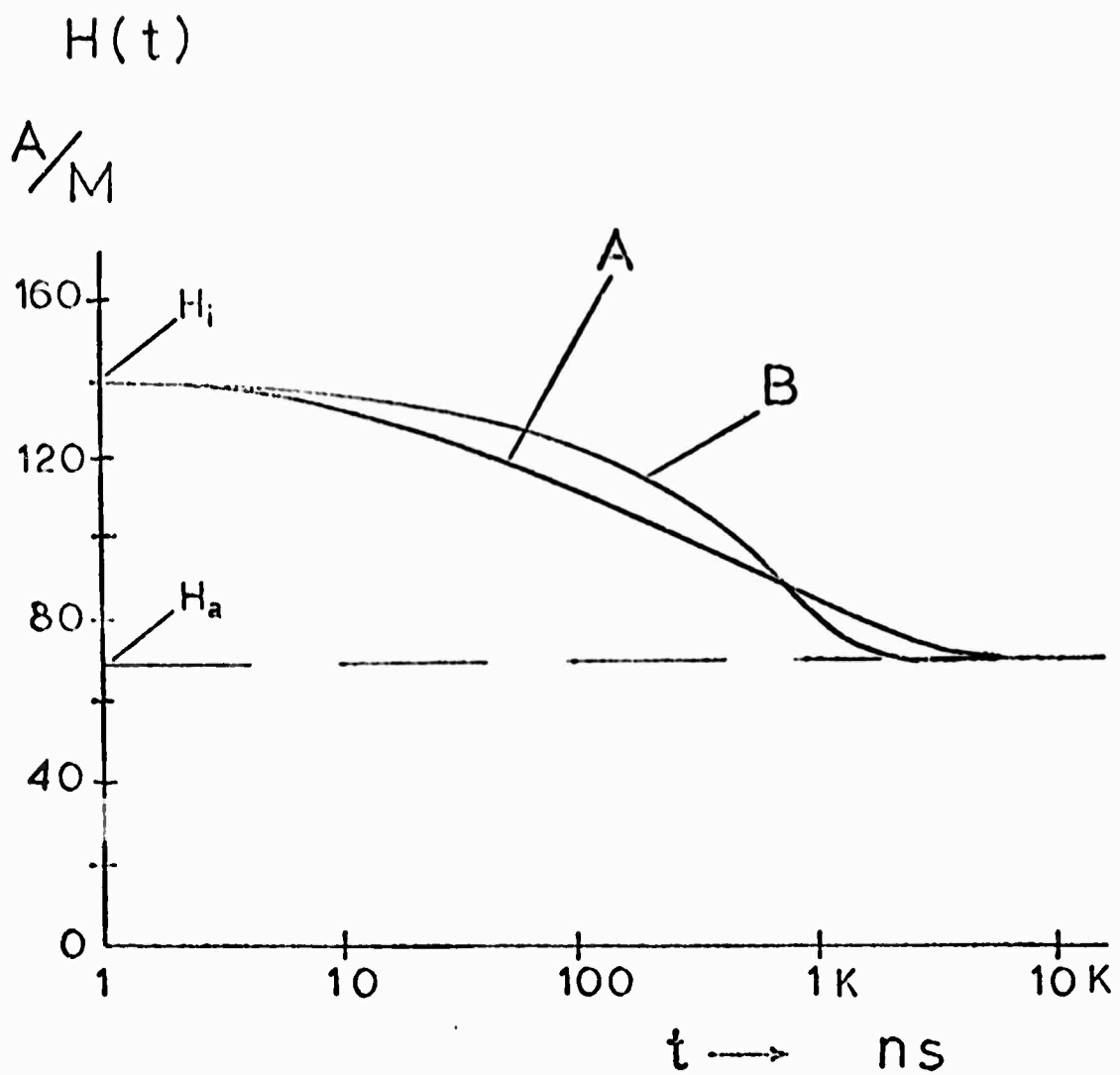


Fig. 8. Slow decay mode comparison. Jutzi's curve, A, and estimation, B, with time constant  $\tau_2 = .487 \mu\text{s}$ .

particularly helpful to the electrical engineer.

The model developed here provides a basis for the observation<sup>10</sup> that eddy-current torques have not been a significant factor in film flux-reversal studies where the stripline separation is large.

The question of accuracy has not yet been fully answered due to the difficulty of measurements, but these results compare well with computations of others<sup>5</sup>.

## APPENDIX

### ELECTRICAL ANALOGY FOR DIFFUSION

The equation for an RC transmission line is well-known to be  $\frac{\partial^2 V}{\partial z^2} = RC \frac{\partial V}{\partial t}$  which has an evident analogy to  $D \frac{\partial^2 B}{\partial z^2} = \frac{\partial B}{\partial t}$  on the basis of the similar equations. The purpose here is to further interpret the parameters of resistance and capacitance per unit length in terms of line geometry.

First, it is argued on the basis of the following tabulation that capacitance is a spatially related parameter which is independent of conductivity, and which serves to contain a diffusing substance. Analogous quantities are vertical.

$$(\text{capacitance}) \times (\text{voltage}) = (\text{charge})$$

$$(\text{area}) \times (\text{flux density}) = (\text{quantity of flux})$$

On that basis we take capacitance per length as analogous to area per length, where the total area is  $yz$ , normal to the  $x$ -direction of flux. Taking length  $y$  as unity leads to unit dimension for  $C$ , hence  $R = 1/D$ . Applying these definitions<sup>to transmission line theory,</sup>  $\gamma = \sqrt{RCs}$  and  $Z_0 = \sqrt{R/Cs}$ , and to the equation for input impedance of an open-circuit line of length  $d$ ,  $Z_{in} = Z_0 \coth \gamma d$ , leads to the equation of case 2.

#### REFERENCES

1. J. S. Eggenberger, J. Appl. Phys., 31, No. 5, May 1960, p. 2875.
2. T. A. Smay, IEEE Trans. Comm. and Elec., 81, Nov. 1964, pp. 808-812.
3. G. Kohn et al, IBM J. of R and D, 11, No. 2, Mar. 1967, pp. 162-168.
4. A. Rudiger, Elect. Rechenanlagen, heft 3, 7 Jahrgang 1965, seite 122-30.
5. W. Jutzi, 1965 Proc. Intermag., p. 8.2.1.
6. C. T. Leis, "Field Diffusion Effects in Nearby Conductors During Fast Switching of Magnetic Films," MSE Thesis, Univ. of Fla., 1969.
7. J. Crank, The Mathematics of Diffusion, London: Oxford Univ. Press, 1956.
8. M. Abramowitz, I. Stegun (eds.) Handbook of Mathematical Functions, Washington: Nat'l. Bureau of Standards, 1964.
9. V. T. Shahan and C. Townsend, 1964 Proc. Intermag., p. 16.2.1.
10. F. B. Humphrey (private communication, circa 1969).

## VI. Discussion

The research of this fifth semiannual period has yielded results of technical significance and it has laid the foundations for future study and growth.

The study of the photomagnetolectric effect in silicon doped with gold and phosphorus has yielded a basic characterization of such material and has suggested several potential applications. Among these is the possibility of a laser beam demodulator utilizing silicon overcompensated with gold, with applications to the field of communications. Research exploring this possibility is now proceeding.

From the study of the density of quantum states in a semiconductor has come a basic understanding of the dependence on impurity concentration of this density. The impurity concentration dependence can manifest itself importantly in the behavior of the highest-performance transistors of the present day, and thus the study has yielded information relevant to the many fields of application that utilize transistors: communications, telemetry, detection, navigation, control, bio-medicine, etc.

The electric field that a ceramic can withstand may determine its applicability in various uses in the electronic technology: as an insulator, as a protective surface in various devices, as an isolator in integrated circuits, and as a material for encapsulation. The study reported here suggests the relative importance of the many variables pertinent to the design of ceramic materials for use in these applications.

From the investigation of the relationship borne between heterogeneities present in semiconducting glass and the consequent electrical properties has come an understanding that will contribute ultimately to the evaluation of the potential merit of semiconducting glass as a device material for



various military applications, particularly for those involving system operation in high-radiation environments.

The trapped-flux interaction between magnetic films and nearby electrical conductors is a well-known phenomenon experimentally and has constituted the basic mechanism of NDRO memories. Its study therefore relates directly to the design of digital computers and thus to many fields of relevance to the D.O.D. Because of its simplicity relative to methods of analysis previously proposed, the new approach reported here to the analysis of this phenomenon promises a substantial advantage to the designer of magnetic memories.

The plan of the research remains unchanged. Emphasis will continue to focus on the relationship between the structural properties of materials, on the one hand, and the resultant electrical, quantum, chemical, and thermal properties, on the other. Device applications made possible by the understanding gained from this materials research will receive increasing attention.

## DOCUMENT CONTROL DATA - R&amp;D

(Security classification of title, body of abstract and indexing annotation must be entered when the overall report is classified)

1. ORIGINATING ACTIVITY (Corporate author) University of Florida Engineering and Industrial Experiment Station Gainesville, Florida 32601		2a. REPORT SECURITY CLASSIFICATION <b>Unclassified</b>	
3. REPORT TITLE <b>A CENTER OF COMPETENCE IN SOLID STATE MATERIALS AND DEVICES</b>		2b. GROUP	
4. DESCRIPTIVE NOTES (Type of report and inclusive dates) <b>Scientific Interim</b>			
5. AUTHOR(S) (First name, middle initial, last name) Fred A. Lindholm                      Robert W. Gould                      Sheng S. Li Arthur J. Brodersen                  Larry L. Hench                      James K. Watson Eugene R. Chenette                  John J. Hren			
6. REPORT DATE <b>10 March 1970</b>		7a. TOTAL NO. OF PAGES <b>206</b>	
		7b. NO. OF REFS <b>151</b>	
6a. CONTRACT OR GRANT NO. <b>F 19628-68-C-0058 ARPA Order No.</b>		9a. ORIGINATOR'S REPORT NUMBER(S) <b>Scientific Report No. 5</b>	
b. PROJECT, TASK, WORK UNIT NOS. <b>8687 n/a n/a</b>			
c. DOO ELEMENT <b>61101D</b>		9b. OTHER REPORT NO(S) (Any other numbers that may be assigned this report)	
d. DOO SUBELEMENT <b>n/a</b>		<b>AFCRL-70-0284</b>	
10. DISTRIBUTION STATEMENT <b>1 - This document has been approved for public release and sale; its distribution is unlimited.</b>			
11. SUPPLEMENTARY NOTES <b>This research was supported by Advanced Research Projects Agency.</b>		12. SPONSORING MILITARY ACTIVITY <b>Air Force Cambridge Research Laboratories (CRW) Laurence G. Hanscom Field Bedford, Massachusetts 01730</b>	
13. ABSTRACT <b>This report describes technical findings in four main subject areas: semiconductors and semiconductor devices, insulating and semiconducting glasses, measurement techniques, and magnetic materials. For silicon doped with gold and phosphorus, a study of the photo-magnetoelectric effect yields a basic theoretical relationship between the excess hole and excess electron concentrations and an experimental determination of the effective lifetime for temperatures between 21 and 84°K. A pragmatic approach is proposed and empirically tested concerning the dependence that the density of quantum states in a semiconductor shows on the impurity concentration. For a variety of ceramic materials, the electric-field breakdown shown is related to the various environmental and material variables. Based on available data concerning material structure, a study is made to characterize the relationship borne in semiconducting glasses between heterogeneity in structure and resultant electrical properties. Errors in x-ray spectrochemical analysis of powdered materials due to pressing variations are quantitatively examined. The several means for analysis of the defect structure of solid surfaces are discussed together with the relation that this defect structure bears to the surface electronic and chemical properties. Small-angle x-ray data on the low-temperature aging of aluminum-zinc alloys is shown to provide a method for determining the particle size distribution as a function of aging time. A new approach is proposed and evaluated for characterizing the trapped-flux interaction between magnetic films and nearby electrical conductors.</b>			

Unclassified

Security Classification

14.	KEY WORDS	LINK A		LINK B		LINK C	
		ROLE	WT	ROLE	WT	ROLE	WT
	semiconductors ceramics magnetic materials semiconducting glasses surface defects						

Unclassified

Security Classification